UNIVERSITY OF POTSDAM

FACULTY OF MATHEMATICS AND SCIENCE
INSTITUTE OF PHYSICS AND ASTRONOMY

ULTRAFAST DYNAMICS IN CONDENSED MATTER

Magnetostriction and timeresolved X-ray diffraction on $TbFe_2$

MASTER THESIS

Author: STEFFEN PEER ZEUSCHNER
szeuschn@uni-potsdam.de

1st Reviewer: Prof. Dr. MATIAS BARGHEER
University of Potsdam

2nd Reviewer: Dr. KARINE DUMESNIL
Institut Jean Lamour

Submission date: December 5th, 2017

Abstract

I provide an overview of magnetostriction theory and utilise X-ray diffraction to observe forced magnetostriction in $TbFe_2$ as well as time resolved X-ray diffraction (UXRD) to examine the structural dynamics of $TbFe_2$ after laser excitation. I compare results from three complementary experimental setups; a conventional micro-focus X-Ray tube of the UDKM group (MFXT), the XPP-KMC3-Beamline at BESSY II and at a plasma X-Ray source of the UDKM group (PXS). Exposing $TbFe_2$ to an external field (MFXT and BESSY II) results in a distortion which depends on the relative orientation of the external field and initial magnetization. An increasing strain is observed during the rotation of the external field, vanishing when magnetization and field becomes antiparallel. The strain results from the tilt and eventually realignment of the sample magnetization due to the external field which I model by calculating and minimizing the competing anisotropy energy E_A and Zeeman energy E_H in terms of the magnetization direction and the external field. Exciting $TbFe_2$ with a sub picosecond laser pulse (BESSY II and PXS) results mainly in thermal expansion as the excited electrons thermally equilibrate with the lattice leading to heat diffusion on the nanosecond time scale. On s picosecond time scale however, a bipolar strain wave emerges at the surface and propagates through $TbFe_2$. The evaluation of UXRD measurements via the UDKM1DSIM-toolbox suggests an ultrafast non-equilibrium heat diffusion in $TbFe_2$, increasingly effective with higher pump fluences, which is essential to model the slope of the observed strain wave.

Kurzdarstellung

Ich gebe einen Einblick in die Theorie von Magnetostriktion, nutze Röntgenbeugung um erzwungene Magnetostriktion an $TbFe_2$ zu beobachten und zeitaufgelöste Röntgenbeugung (UXRD) um die ultraschnelle Gitterdynamik in $TbFe_2$ nach einer Laseranregung zu vermessen. Dabei benutze ich drei verschiedene Aufbauten; eine konventionelle Mikro-Fokus Röntgenröhre (MFXT) aus der UDKM Arbeitsgruppe, die XPP-KMC-3-Beamline am BESSY II und die Plasma Röntgenquelle (PXS) aus der UDKM Gruppe. Setzt man $TbFe_2$ einem externen magnetischen Feld aus (MFXT und BESSY II), resultiert dies in einer Gitterverzerrung, abhängig von der Richtung des externen Feldes relativ zu der anfänglichen makroskopischen Magnetisierung der Probe. Eine wachsende relative Gitterausdehnung wird bei Rotation des externen Feldes beobachtet, welche verschwindet wenn die Magnetisierung und das externe Feld antiparallel stehen. Das Verhalten der Ausdehnung kann auf die Neigung und schließlich Neuausrichtung der Magnetisierung parallel zum externen Feld zurückgeführt werden. Dies habe ich modelliert, indem ich die konkuriende Anisotropieenergie E_A und Zeemanenergie E_H berechnet und bezüglich der Magnetisierungsrichtung minimiert habe, abhängig von der Richtung des externen Feldes. Bei den zeitaufgelösten Experimenten wird $TbFe_2$ von einem sub-Pikosekunden Laserpuls angeregt (BESSY II und PXS), was hauptsächlich in einer thermischen Ausdehnung resultiert. Die angeregten Elektronen equilibrieren thermisch mit dem Gitter und es folgt eine Wärmediffusion im Gitter auf einer Zeitskala von wenigen Nanosekunden. Außerdem weise ich auf einer Skala einiger Pikosekunden das Entstehen einer bipolaren, kohärenten Schallwelle an der angeregten Oberfläche und ihre Propagation durch $TbFe_2$ nach. Ferner weist die Auswertung der UXRD-Messung mithilfe der UDKM1DSIM-toolbox darauf hin, dass ein Prozess der ultra-schnellen Wärmediffusion in $TbFe_2$ zu beobachten ist, dessen Einfluss effektiv mit steigender Fluenz deutlicher wird.

Contents

Introduction

Magnetostriction, i.e. the interplay of magnetic properties and distortions of crystal lattices, was described first by J. P. Joule in the year 1847 [1]. Since his experiments on iron and steel bars, in which the magnetostrictive effects at room temperature are only of the order of 10^{-6}, 125 years elapsed until A. E. Clark and H. S. Belson discovered "*giant*" magnetostriction in $TbFe_2$ and $DyFe_2$ with up to 0.2% strain at room temperature [2]. Beginning with the work of N. S. Akulov in the 1930's [3], the development of models for magnetostriction launched, which were strongly stimulated by the work of C. Kittel in 1949 [4]. The discovery of huge magnetostriction at room temperature in rare earth alloys however, spurred the interest of the application driven research as it seemed now possible to utilise magnetostriction similar to piezo-electricity as a magneto-acoustic transduction mechanism. This amplified the experimental and theoretical coverage of magnetostriction, especially in rare earth alloys.

1. Motivation of my work

The ultrafast dynamics group (UDKM) in Potsdam has worked on this topic, especially on the ultrafast demagnetization by photo excitation and associated magnetostriction in dysprosium and holmium, cf. J. Pudell and A. von Reppert [5, 6]. The understanding and observation of magnetically induced magnetostriction by selectively manipulating the magnetic system has been less developed in the UDKM since they had focussed on the excitation of the electronic or phonon systems of ferromagnetic solids by light. Forced magnetostriction, i.e. the direct lattice distortion as a response to an applied external magnetic field is well documented by Clark since the 70's [7] and a theoretical description of the mechanics is well known as G. Engdahl summarises it in his book [8]. Nevertheless, an in depth study of the ultrafast magnetical and structural dynamics of $TbFe_2$ is, to my knowledge, yet to be presented. With the aim to develop faster and more efficient digital data processing and memory devices, ultrafast magnetic response and magnetostriction as a control or observation mechanism is a promising topic for future and contemporary storage devices [9, 10].

Eventually, a comprehensive understanding of the entirety of the solid's subsystems, including the electrons, magnons and phonons, is intended. In particular with respect to the future examination of newly approached multiferroic materials, such as $BiFeO_3$ [11]. The latter exhibit a combination of ferromagnetic and ferroelectric properties. Thus they can be treated with electric and magnetic fields to independently manipulate the specific subsystems so that the lattice is eventually indirectly distorted. Therefore, I engaged an extensive search at the beginning of my thesis work, concerning relevant literature about magnetostriction in $TbFe_2$ and the theory of static magnetostriction in general to provide a theoretical foundation for further advances in current magnetostrictive research in our group.

2. Structure of the thesis

This section presents an overview over the structure of this thesis:

Part I In the beginning I focus on providing a theoretical foundation for the subsequent parts of the thesis. I give an introduction to the formalisms of crystallography and X-ray diffraction as it is the experimental method of choice, employed to observe the crystalline distortions in of $TbFe_2$. After shortly discussing the magnetic properties of $TbFe_2$, I end the first part with an evaluation of literature concerning magnetostriction, especially in $TbFe_2$ resulting in a summary of the usual and relevant modelling approaches. Note that not the entire presented and summarized magnetostrictive theory and data are used during the remaining course of this thesis. Part I functions also as a compendium concerning magnetostriction in general to provide a concise description of magnetostriction for future research projects in the group.

Part II In the second part, I describe the experimental setups, the measurement routines and the data evaluation for the slow magnetostriction experiments which do not use laser excitation. As two experimental setups are used to perform forced magnetostriction, i.e. to distort $TbFe_2$ by the exposure to an external magnetic field, I compare data sets collected by X-ray diffraction and associate the findings with the characteristics of magnetostriction condensed in Part I. Furthermore, I discuss a model to predict the magnetostrictive response of our samples by calculations and simulations based on the magnetostrictive theory. In this framework I interpret the measurement results.

Part III In the final part I describe the experimental setups and data handling routines which are employed to describe time resolved pump probe measurements. The $TbFe_2$ sample is exposed to an ultrashort laser pulse as an excitation and subsequently and ultrashort X-ray pulse is diffracted which probes the lattice. Thus, the dynamics of the lattice after photo excitation is recorded and evaluated utilising a modelling tool provided by the UDKM group, the UDKM1DSIM-toolbox.

Part I.

Theoretical basis and tools

To achieve a detailed understanding of physical effects, it is essential to be familiar with the underlying principles resulting in observed effects. I review some essentials, such as crystallography, continuum mechanics, magnetism, magnetostrictive theory and X-ray diffraction as my choice of the basic experimental method in this work and relate them to $TbFe_2$.

Magnetostriction is the change of length or volume of a material under variation of the magnetization. I start with a description of the crystal structure of $TbFe_2$and describe the principles of X-ray diffraction which is a useful tool to determine the crystalline structure. Together with magnetic properties of Rare Earth alloys in particular the relevant magnetostrictive theory is illustrated with many references to the literature.

3. Crystallographic basics

3.1. Description of crystals (cf. [12])

The heavy rare earth transition metal alloy $TbFe_2$ consists of Terbium ($_{65}Tb$) and Iron ($_{26}Fe$). Terbium is a rare earth element of the lanthanoid series, neighboured by Gadolinium and Dysprosium. Iron is a transition metal which is one of the few ferromagnetic elemental metals at room temperature. Many of the heavy rare earth transition metal compounds have been studied because of their magnetic properties, for instance the observed giant magnetostriction in $TbFe_2$ in 1972 [2].

$TbFe_2$ crystallises in the cubic binary C15 Laves phase[1], which has a cubic conventional unit cell as depicted in Fig. 3.1. The lattice constant is $a_{\mathrm{TbFe_2}} = 7.347 \pm 0.001$ Å [17, 18] and $TbFe_2$ has a density of $\rho_{\mathrm{TbFe_2}} = 9.0\,\frac{\mathrm{g}}{\mathrm{cm}^3}$ [19] when forming a single crystal. A single crystal consists of plenty units cells which are equally oriented and sharing the atoms located at the border of a unit cell with its neighbours. Thus one corner ion of the unit cell will also be part of seven other neighbouring cells. Polycrystalline materials are different as they are made of many small single crystals with arbitrary orientations.

3.1.1. Description of crystal lattices

In solid state physics a single crystal is described as the combination of a lattice and a basis. The basis is associated with the unit cell and the lattice consists of three linear independent primitive lattice vectors $\vec{a}_1$, $\vec{a}_2$ and $\vec{a}_3$. Every point ($\vec{R}$) of the lattice can be expressed with a linear combination of those vectors:

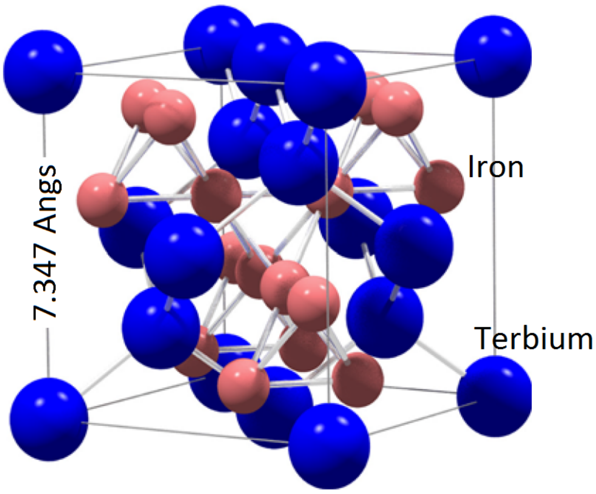

Figure 3.1: Schematic sketch of the unit cell, taken from Bentall et al. [20]. The blue spheres are the rare earth atoms and the rose ones are the transition metal atoms.

$$\vec{R} = n_1\vec{a}_1 + n_2\vec{a}_2 + n_3\vec{a}_3, \tag{3.1}$$

where n_{i} are integers. Placing a basis, i.e. unit cell, at every point of the lattice will create a crystal. For $TbFe_2$ which has basically a cubic lattice, $\vec{a}_{\mathrm{i}}$ are perpendicular, creating a Cartesian coordinate system $\hat{x}$, $\hat{y}$ and $\hat{z}$ which is aligned along the axes of the cubic unit cell. The length of $\vec{a}_{\mathrm{i}}$ is $a_{\mathrm{TbFe_2}}$.

---

[1] Often rare earth transition metal compounds form in a cubic Laves phase. It is named after F. Laves who wrote about this sort of structure first in 1934 [13]. One unit cell consists of two rare earth atoms with a tetrahedral (Td) site symmetry and four transition metal atoms with a D_3d symmetry [14]. A special type of Laves phases are binary Laves phases, where only two sorts of elements are included, such as $TbFe_2$. Furthermore, already more than 360 different binary Laves phases have been discovered. Every one of them has a unique ordered arrangement of atoms on the lattice sites [15]. $TbFe_2$ is part of the C15 subgroup of binary Laves phases, also called $MgCu_2$ structure, after the prototype of this special Laves phase. Laves phases are often considered, because of the magnetoelastic and magnetostrictive properties in rare earth transition metal alloys especially at room and higher temperatures, as it is discussed in the present thesis. Some alloys like HfV_2 and ZrV_2 even exhibit superconducting properties [16].

3.1.2. Crystal planes and Miller indices

The concept of crystal planes must be discussed because they will be needed in the derivation of X-ray diffraction. Looking at Fig. 3.1, we can see for example that the five Tb ions at the top lay in one plane. Also the five ions at the bottom. Those two planes extend over the whole single crystal and will always have the same distance to each other, since they are parallel. Because the crystal is also spatially extended perpendicular to those planes, there will be plane over plane and each of them can not be distinguished from each other. Equidistant, parallel planes are therefore indistinguishable so the set of such planes and their surface vectors are described by the Miller indices (hkl).

In Fig. 3.2, some examples of crystal planes in a conventional unit cell are depicted. For $\mathrm{TbFe_2}$, set $\mathbf{a} = a_{\mathrm{TbFe_2}}\hat{x}$, $\mathbf{b} = a_{\mathrm{TbFe_2}}\hat{y}$ and $\mathbf{c} = a_{\mathrm{TbFe_2}}\hat{z}$. The three numbers in brackets are sufficient to describe one set of parallel planes and are called Miller indices.

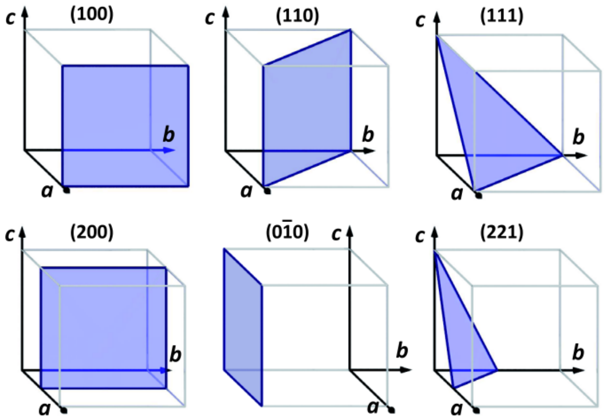

Figure 3.2: Examples for crystal planes with associated Miller indices, taken from Gross & Marx [12].

Each set of distinguishable planes can be associated with Miller's indices by noting the intersection points of planes and crystal axes in units of the lattice constants. Afterwards one takes the reciprocal value of those numbers and expand the resulting ratios to integers, which are the associated Miller indices for the discussed set of planes. The last plane in Fig. 3.2 for example is called the (221) plane because it intersects the $\hat{x}$ and $\hat{y}$ axis at $\frac{1}{2}$ of their unit length, giving $h = k = \left(\frac{1}{2}\right)^{-1} = 2$, and the $\hat{z}$ axis at one unit, giving $l = 1^{-1}$. Note that negative values are often visualised by a mark on top of the numbers, as we can see in the fifth example $(0\bar{1}0)$, meaning $h = l = 0$ and $k = -1$. The Miller indices are conventional tools and omnipresent in the research and literature concerning X-ray diffraction and crystallography.

Another use of the Miller indices, besides the specification of planes, is the definition of directions in crystals. Taking Eq. 3.1 and setting $n_1 = h$, $n_2 = k$ and $n_3 = l$, we will get a vector $\vec{R}$ which is perpendicular to the certain set of (hkl) planes. In general, the raw length of that vector is not a useful quantity. But with a normalization, which reduces to $(h^2 + k^2 + l^2)^{-1}$ for cubic lattices, it provides the lattice spacing according to:

$$d_{\mathrm{hkl}} = \frac{a}{\sqrt{h^2 + k^2 + l^2}}, \tag{3.2}$$

where a is the lattice constant and d_{hkl} the distance of two neighbouring planes.

3.1.3. Sample structure

The main sample used in this work is labelled TbFe42. It was grown using MBE[2] by K. Dumesnil at the IJL in Nancy, France, and its cross-section is depicted in Fig. 3.3 [22]. It consists of 2 nm titanium on the surface as a protection layer on top of a 500 nm single crystal $TbFe_2$. A 100 nm niobium buffer connects the thin film to the Sapphire substrate (Al_2O_3). All four layers are grown as single crystals with a fixed crystallographic direction. The (110) direction of the cubic $TbFe_2$ and niobium is perpendicular to the surface of the sample, as well as the $(11\bar{2}0)$ direction of the Sapphire substrate (it has an additional Miller indices because Sapphire crystallises in a hexagonal structure and has therefore another crystallographic symmetry). Thus it is clear that the (110)-planes of the $TbFe_2$ crystal is parallel to the surface and the $\hat{z}$ direction lies in plane, see the second example in Fig. 3.2.

Figure 3.3: TbFe42-sample.

3.2. Concepts of X-ray diffraction (cf. [12, 23])

The used sample of $TbFe_2$ has a crystalline structure, which changes when the lattice distorts due to magnetostriction. X-ray diffraction is a useful tool to examine small changes in the lattice which has been conducted on $TbFe_2$ from the seventies [24, 25] to the present [26]. Consequently we have to understand the principles of X-ray diffraction to be able to interpret collected data correctly or to design useful experimental setups.

3.2.1. Reciprocal lattice

Leading to X-ray diffraction, a theoretical model for the description of crystals is introduced first, the reciprocal lattice. In the associated chapter of Gross & Marx [12], the reciprocal lattice related to a crystal lattice is well defined, as it possess the same structure as the crystal lattice described beforehand. The reciprocal lattice is made of reciprocal lattice vectors $\vec{G}$ which can be written as a set of three unit vectors (in cubic systems), in analogy to Eq. 3.1:

$$\vec{G} = h\vec{b}_1 + k\vec{b}_2 + l\vec{b}_3, \tag{3.3}$$

where $\vec{b}_1 = \frac{2\pi}{V_C}\vec{a}_2 \times \vec{a}_3$ ($\vec{b}_2$ and $\vec{b}_3$ accordingly, cyclic permuted) and h, k and l are integers with $V_C = \vec{a}_1 \cdot (\vec{a}_2 \times \vec{a}_3)$, which is the volume of one unit cell in the crystal lattice. It is no coincidence that those integers and the Miller indices are labelled the same. There is a connection between the reciprocal lattice vectors and the planes in the real crystal lattice. According to Gross & Marx, to every set of planes (hkl), there are reciprocal lattice vectors $\vec{G}$ and vice versa, so that $\vec{G}$ is perpendicular to the planes. For the longest reciprocal lattice vector $\vec{G}_{\text{max}} = h\vec{b}_1 + k\vec{b}_2 + l\vec{b}_3$, it is:

$$|\vec{G}_{\text{max}}| = \frac{2\pi}{d_{\text{hkl}}}, \tag{3.4}$$

where d_{hkl} is the distance of two neighbouring (hkl) planes, defined by Eq. 3.2. The reciprocal lattice therefore contains vectors associated with every set of planes possibly found in the real crystal lattice. The direction of the reciprocal lattice vectors provide the orientation of the planes, since the reciprocal

---

[2] Molecular Beam Epitaxy was introduced by Cho and Arthur in 1975 [21]. It is an experimental technique to deposit crystalline structures on a single crystal substrate. In this technique one or several thermal molecular beams are merged on the substrate surface in ultra-high vacuum to grow a crystalline layer. Its advantage lies in the direct control of the atomic or molecular beam fluxes which allows a rapid change of the deposited species. Thus it is possible to grow crystals very precisely, layer by layer, enabling for example the deposition of 10 Å layers with alternating materials or compositions, a so called superlattice. Another benefit is the resulting epitaxy of the crystal layers on the substrate. It means that the lattices of the deposited layer and substrate are the same, although their respective lattice constants may differ. This mismatch is the reason for lattice distortions near the interface of layer and substrate. This is sometimes unwanted and can be reduced by placing a buffer between the substrate and layer, where the lattice constant of the buffer lies in between the lattice constants of the substrate and layer. For the depicted TbFe42 sample, 50 nm niobium is used to minimise the distortions in $TbFe_2$, making it nearly a single crystal.[22]

lattice vectors are perpendicular to their associated crystal planes. The reciprocal lattice is thus a representation of all possible crystal planes. With that in mind, we can now focus on the scattering or diffraction of X-rays from crystal structures.

3.2.2. Bragg's Law

In 1913, W. L. Bragg and his father W. H. Bragg introduced Bragg's law [27] as a quantitative method to describe X-ray diffraction patterns (or Laue photographs) observed by M. Laue and his group [28]. Son and father Bragg were awarded the Nobel price in 1915, and M. Laue in 1914 who invented a unified description of X-ray diffraction with his Laue equation, which reduces to Bragg's law. Nevertheless, we will first discuss the equivalent Bragg's law as it is less abstract and therefore easier to understand the main idea behind X-ray diffraction.

In the following, two basic assumptions are made. First, the wavelength of the X-ray light has the same order of magnitude as the lattice constants. Operating the MFXT or the PXS, the $K_{\alpha 1}$ line of Copper is used for X-ray radiation (see Sec. 6.1.1) which has an associated wavelength of approximately 1.54 Å, while the BESSY II setup is using a monochromator to freely chose a wavelength in the hard X-ray regime. So the first assumption is realised by the setups used and the second one is that X-rays are scattered elastically and therefore do not lose energy during the diffraction process.

Bragg stated, that a crystal may be divided into planes with a certain distance d and we already saw that this is a possible way to describe a crystal. Furthermore those planes are able to reflect X-ray radiation, so that an incoming wave will be partially reflected at each plane. The reflections and diffraction patterns of the Laue photographs are found exactly for those directions in which the reflected waves are interfering constructively. Assuming an incident X-ray with the wavelength λ under the angle ϑ onto planes with the distance d, constructive interference will be observed if the path difference between two X-ray beams reflected on neighbouring planes is a multiple of the wavelength. The situation is depicted in Fig. 3.4a and condenses in Bragg's law, the condition for constructive interference of X-ray scattered from adjacent crystallographic planes:

$$2d \sin\vartheta = n\lambda \qquad n = 1, 2, 3, \ldots \tag{3.5}$$

If the reflected intensity reaches a local maximum at a certain angle ϑ, one speaks of it as a (hkl) reflection, relating to the (hkl) set of planes on which the X-rays are reflected. Knowing the X-ray wavelength λ and the diffraction angle ϑ of a local maximum by using for example the diffraction pattern in Fig. 3.4b, we can calculate with Eq. 3.5 the distance d_{hkl}. However, we must now clarify some issues to understand the diffraction pattern depicted in Fig. 3.4b.

3.2.3. Interpretation of X-ray diffraction patterns

In Fig. 3.4b the $\mathrm{TbFe_2}$ peak is labelled (220). In the explanation of the Miller indices it was stated, that the numbers (hkl) must be reduced, which would not allow a triplet like (220). There are two equivalent interpretations of this notation. We could say, that it is the second order reflection of the (110) plane, manifesting in $n = 2$ in Eq. 3.5. Or we could define the (220) plane set as the planes which are still parallel to the (110) planes but just have half the distance to their neighbours, i.e. only every second plane of the (110) set is considered.

Next we need to explain why the displayed reflections of the $\mathrm{TbFe_2}$, Sapphire and niobium crystals differ in intensity, width and and shape. The answer lies partially in the amount of planes which are reflecting. A single atomic layer reflects 10^{-3} to 10^{-5} of the incident intensity, which means if there are only few planes, the maximal reflected intensity must be significantly smaller than it would be with many planes. If we take a look at the sample's cross section in Fig. 3.3, it is clear, that niobium can only reflect so little because it is only 100 nm thin, $\mathrm{TbFe_2}$ will reflect a bit more because of the 500 nm thickness and Sapphire will be of course the most intense reflection because it offers the highest amount of reflecting

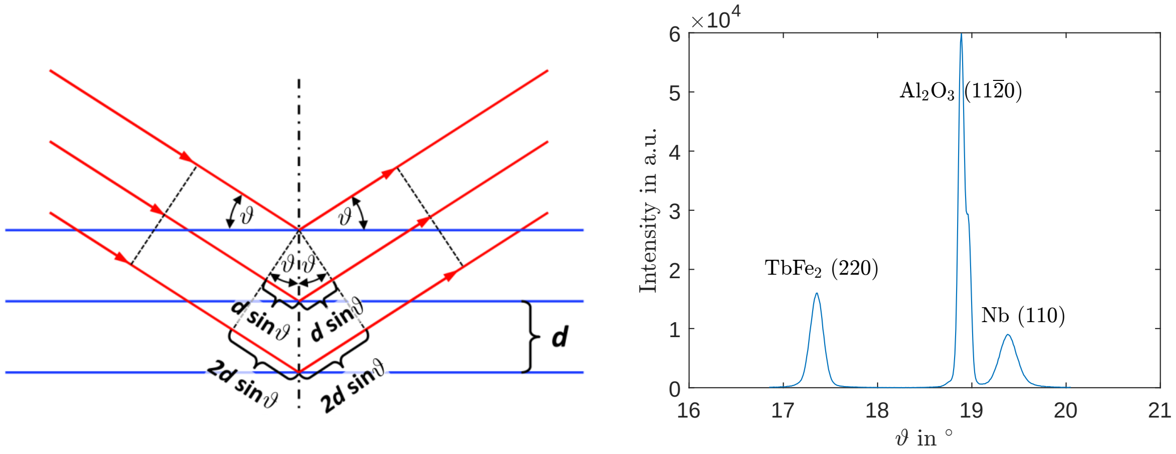

(a)

(b)

Figure 3.4: (a): Sketch of reflection of X-rays at equidistant planes of a crystal to visualise Bragg's law, adapted from Gross & Marx [12]. The red lines indicating the X-ray light reflected on the planes with a distance d. The path difference equals $2d\sin\vartheta$ and must be a multiple of the wavelength λ to achieve constructive interference. **(b)**: Diffraction pattern of the TbFe42 sample measured with the MFXT setup. Varying the diffraction angle ϑ results in different intensities measured. The (220) planes of $TbFe_2$, the $(11\bar{2}0)$ planes of sapphire and the (110) planes of niobium with their different distances d reflecting under certain angles only.

planes because of it's layer thickness.

However we can see, the intensity is not even remotely proportional to the thickness of the layers. Two other material-dependent properties are affecting the intensity, namely the penetration depth and the structure factor. The penetration depth results from the fact that crystals or matter in general scatter and absorb (in this case also reflect) X-rays and any other sort of light. This leads to an exponential decrease of incident intensity[3] the deeper particular reflective planes are located inside the sample. Due to the fact that the Sapphire substrate lies under 600 nm of absorbing and reflecting material the $(11\bar{2}0)$ Sapphire reflection is not some orders of magnitude higher than the other reflections are. The structure factor gives an explanation why some planes of some materials only reflect 10^{-5} and some up to 10^{-3} of the incoming intensity and it will be discussed later in relation to the scattering amplitude with Eq. 3.9.

The width of a peak is determined by the number of reflecting planes and the more there are, the sharper the peak will be. That is why the niobium reflection is the broadest, the $TbFe_2$ is a bit sharper and the Sapphire reflection is even sharper. That relationship finds its quantitative description in the lattice sum, also discussed in combination with the structure factor with Eq. 3.9.

Additionally, the sharpness of the Sapphire $(11\bar{2}0)$ reflection reveals another factor, which not only broadens the peaks but also changes their shape. In Fig. 3.4b we can see a weak shoulder at the right side of the Sapphire peak. This feature arises from the not fully monochromatic X-rays used in the MFXT

---

[3] The intensity-decrease is an interplay of mainly two interaction processes of X-ray with matter. At first, there is the inelastic Compton scattering where photons are colliding with free electrons inside the material changing their momentum and transferring energy to the electron hit. Those photons can not be used for X-ray diffraction any more. And there is the photoelectric absorption where a photon is fully absorbed by a bound electron which now has enough energy to escape its potential well of the nucleus. Fluorescent X-ray emission might be a secondary effect, but the generated light has no favoured direction and can also not be used for further X-ray diffraction. Quantitatively, the absorption is described by the Beer-Lambert law: $I(z) = I(z = 0)\exp(-\mu z)$, where $I(z)$ is the intensity after a depth of z and μ is the material-specific penetration depth, with $\mu = \frac{\rho_\mathrm{m} N_\mathrm{A} \sigma_\mathrm{a}}{A}$, where ρ_m, N_A, σ_a and A are the mass density, Avogadro's number, the absorbtion cross-section and the atomic mass number, respectively [23].

setup. Most photons used for X-ray diffraction here are in fact related to the K_{α_1} line of Copper, but a fraction comes from the K_{α_2} line and the bremsstrahlung background spectrum. Thus, Bragg's law is fulfilled for different parts of the X-ray spectrum at different angles and light is reflected at angles where Bragg's law is not fulfilled for K_{α_1} light but for different wavelengths λ. The shoulder does not appear at the niobium and $\mathrm{TbFe_2}$ peaks because they are already too broad because of the lattice sum, to make such a feature visible.

After this simple look at X-ray diffraction by Bragg's law, basically interpreting the lattice planes as partially reflecting mirrors, but still using the term of interference to explain measured intensity patterns of reflective crystals, a more mature, but still equivalent model must be presented. It is because Bragg's law confines itself to describe only symmetric reflections, meaning that the angle of incidence equals the reflection angle, in both cases ϑ. This allows only the reflection-detection and distance-determination of planes parallel to the surface of a sample. Reflections of planes inside a crystal that are not parallel to the surfaces, can not be seen if the angle of incidence and the reflection angle are the same and thus the distances between the planes can not be assigned[4]. The detection and description of so called asymmetric reflections, where the incident and reflection angle differ, is easier with the Laue equation.

3.2.4. Laue equation

If a plane electromagnetic wave $\mathrm{e}^{i\vec{k}\cdot\vec{r}}$ like X-ray enters a medium it can scatter elastically, meaning only changing the direction of its associated wave vectors from $\vec{k}$ to $\vec{k}'$. The related momentum change $\Delta\vec{k} = \vec{k}' - \vec{k}$ is often called $\vec{Q}$, the scattering vector, see Fig. 3.5a. In a crystal, there are many scattering centres placed equidistantly, the atoms with a large electron density. And the scattered waves with the wave vectors $\vec{k}'$ may interfere, if one condition is fulfilled which is basically the same as it is in Bragg's law; The path difference between adjacent scattering paths from neighbouring scattering centres must equal a multiple of the wavelength, which is anti-proportional to the wave vectors length ($|\vec{k}'| = |\vec{k}| = \frac{2\pi}{\lambda}$), see Fig. 3.5b:

$$|\vec{r}|\cos\varphi' - |\vec{r}|\cos\varphi = n\lambda \qquad n = 1, 2, 3, \ldots \tag{3.6}$$

where $\vec{r}$ is the origin of the electromagnetic waves, i.e. $\vec{r} = \vec{R}$ (because the scattering centres are distanced by $\vec{R}$ in a lattice, defined by Eq. 3.1), and φ and φ' are the incident and scattering angle, respectively. This equation looks similar to Bragg's law 3.5, and is actually the same, setting $|\vec{R}| = d$, $\varphi' = -\varphi$ and $\cos\varphi = \sin\vartheta$, as it is done to construct the situation in Fig. 3.4a. Even so, Eq. 3.6 can be further evaluated. With $|\vec{R}|\cos\varphi' = \vec{R}\cdot\hat{k}'$ and $|\vec{R}|\cos\varphi = \vec{R}\cdot\hat{k}$, it follows

$$(\vec{k}' - \vec{k})\cdot\vec{R} = 2\pi n \quad \Leftrightarrow \quad \mathrm{e}^{i\vec{Q}\cdot\vec{R}} = 1. \tag{3.7}$$

This relation is equivalent to the definition of reciprocal lattice vectors. Thus, all $\vec{Q}$ are reciprocal lattice vectors $\vec{G}$ to the crystal lattice defined by $\vec{R}$. The Laue equation in its reduced form is now derived:

$$\vec{Q} = \vec{G}, \tag{3.8}$$

meaning that constructive interference of X-rays scattered by a crystal lattice will appear, if the scattering vector $\vec{Q}$ equals any reciprocal lattice vector $\vec{G}$ of the crystal lattice. We are now able to calculate $\vec{Q}$ by setting $\vec{k}$ and measuring $\vec{k}'$, and we will then know the direction and length of $\vec{G}$, which will give us the associated set of (hkl) planes and their distance d_{hkl}, respectively (see Eq. 3.3 and 3.4). Because $\vec{k}$ and $\vec{k}'$ are vectors, all kinds of directions, i.e. incident and reflective angles are possible, almost every set of planes can be examined and described with the help of the reciprocal lattice as an essential theoretical model for X-ray diffraction techniques.

---

[4] It is important to note, that Bragg's law is of course viable for every set of planes, no matter how they are oriented. But in the experiment, we have a macroscopic sample with only one distinguished direction, the direction out-of-plane, perpendicular to the surface. So we do not know how planes are oriented in relation to the sample surface. With a $\vartheta/2\vartheta$-Scan where the sample is rotated by ϑ and the detector by 2ϑ in relation to the incident X-ray beam, only planes parallel to the surface will reflect. Thus we have to take different incident and reflection angles referred to the sample surface to see asymmetric reflections.

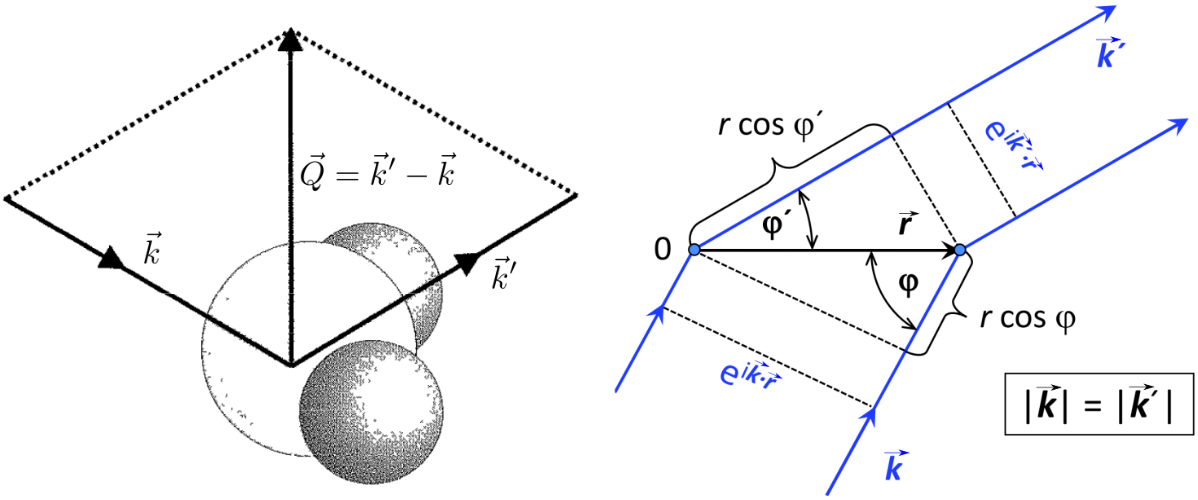

(a) **(b)**

Figure 3.5: **(a)**: Definition of the scattering vector $\vec{Q}$, adapted from Als-Nielson [23]. The depicted scattering centre is a molecule. **(b)**: Sketch of the scattering of an electromagnetic wave at two lattice points, adapted from Gross & Marx [12].

3.2.5. Scattering amplitude and intensity

With the Laue equation we can now associate the positions of reflections with a set of planes. So far the intensity and appearance of the Bragg peaks was only partly explained in relation with Fig. 3.4b. The lattice sum and the structure factor were the two parts missing to fully understand the measured X-ray intensity. Thus we recall basic scattering theory and define the scattering amplitude $\mathcal{F}$ of X-rays scattered by a certain crystal. It is the product of the structure factor and the lattice sum. Also, the scattered intensity $I(\vec{Q})$ is proportional to the square of $\mathcal{F}$ which is given by:

$$\sqrt{I(\vec{Q})} \propto \mathcal{F}(\vec{Q}) = \overbrace{\sum_{j=1}^{N} f_{\mathrm{j}}(\vec{Q}) \mathrm{e}^{i\vec{Q}\cdot\vec{r}_{\mathrm{j}}}}^{\text{structure factor: } S_{\mathrm{hkl}}} \; \overbrace{\sum_{n=1}^{M} \mathrm{e}^{i\vec{Q}\cdot\vec{R}_{\mathrm{n}}}}^{\text{lattice sum: } \mathcal{G}} , \tag{3.9}$$

where $f_{\mathrm{j}}(\vec{Q})$ are the atomic scattering factors, $\vec{r}_{\mathrm{j}}$ the place of the jth atom in the unit cell, N is the number of atoms in one unit cell, $\vec{R}_{\mathrm{n}}$ the place of the nth unit cell inside the scattering crystal and M the number of scattering unit cells.

The lattice sum $\mathcal{G}(\vec{Q})$ can be evaluated as follows: It approaches M if $\vec{Q} \rightarrow \vec{G}$ and for very large M rapidly converges to zero if $\vec{Q} \neq \vec{G}$. A large M is interpreted as a participation of many unit cells in the scattering process, i.e. many planes contribute to the reflection. The larger M gets, the more $\mathcal{G}(\vec{Q})$ resembles a set of δ-functions in the $\vec{Q}$ space. With a decreasing number of unit cells or planes contributing to the scattering, this set of sharp peaks is broadened and forms side maxima, see Fig. 3.6a. The number of the side maxima increases with M, as their absolute value decreases to converge to the δ-functions. That is the reason why a Bragg peak broadens and loses intensity as the thickness of a reflective layer reduces.

Closely linked to the discussed reflectivity of a crystal plane are the structure factor $S_{\mathrm{hkl}}(\vec{Q})$ and the atomic scattering factor $f_{\mathrm{j}}(\vec{Q})$. The latter gives the scattering strength of the jth atom in a unit cell and changes for different types of atoms. Generally it decreases monotonically with an increasing $\vec{Q}$ and is

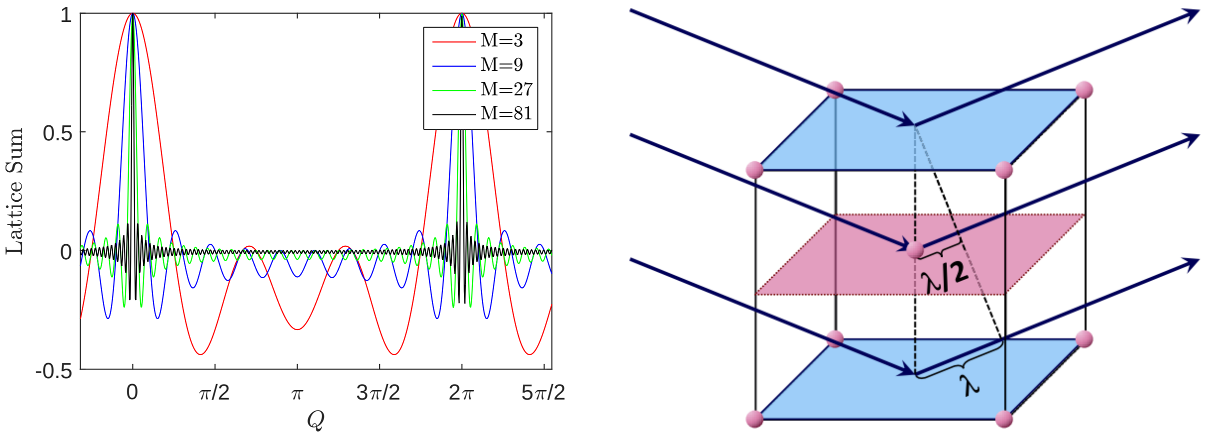

(a)

(b)

Figure 3.6: (a): Graphs of one dimensional lattice sums for four different M, normalised with $\frac{1}{M}$. $\vec{Q}$ and $\vec{R}$ are reduced to Q and n, respectively. Thus, following Eq. 3.9, the function of the graphs is $\frac{1}{M}\sum_{n=1}^{M}\cos(nQ)$, with $Q \in [-1, 8]$. One can see that the amplitude of the peaks at 0 and 2π is equal to M and that with an increase of M, side maxima and minima are decreasing relative to the main maxima, as latter are getting more narrow. **(b)**: Sketch of the situation leading to a forbidden reflection taken from Gross & Marx [12]. A unit cell of a bcc crystal (body-centered-cubic, crystal with cubic unit cell containing one centre atom) is sketched and the paths of X-ray are drawn just like in Fig. 3.4a. While the atoms in the planes on the top and bottom (blue) of the cube are fulfilling Bragg's equation, the atom in the centre does not. It is part of a plane (red) lying parallel to the top and bottom plane. Thus the path difference between two reflecting planes is now $\frac{\lambda}{2}$ which leads to destructive interference.

defined by:

$$f(\vec{Q}) \;= \int \rho(\vec{r})\; \mathrm{e}^{i\vec{Q}\cdot\vec{r}} d\vec{r}, \tag{3.10}$$

where $\rho(\vec{r})$ is the electron density of the described atom, with $f(\vec{G} \rightarrow \infty) = 0$ and $f(\vec{G} \rightarrow 0) = Z$, the atomic charge number. The scattering capabilities of all atoms in one unit cell are combined in the structure factor $S_{\mathrm{hkl}}(\vec{Q})$. It varies with $\vec{Q}$ but since $\mathcal{G}(\vec{Q})$ quickly drops to zero if $\vec{Q} \neq \vec{G}$, the product $\mathcal{F}(\vec{Q})$ is finite only at those $\vec{Q}$ where the Laue equation is fulfilled. Therefore the strucutre factor must only be evaluated for every Bragg reflection, for every set of reflecting planes and has therefore associated Miller indices (hkl).

In addition to the scattering properties of the atoms, $S_{\mathrm{hkl}}(\vec{Q})$ also encodes their positions in the unit cell. Several reflections must be measured to determine the structure factor and some reflections can not be observed, so called characteristic forbidden reflections with $S_{\mathrm{hkl}}(\vec{Q}) = 0$ for the (hkl) set of planes and present unit cell. An example for the occurrence of a so called forbidden reflection is depicted in Fig. 3.6b. Thus the intensity of a Bragg reflection is determined by the structure factor and the lattice sum.

3.2.6. Debye-Waller factor

Another important factor in the interpretation of X-ray diffraction patterns is the Debye-Waller factor. It reduces the intensity of reflections with increasing length of $\vec{G}$, if a finite temperature sets atoms into motion:

$$I_{\mathrm{hkl}} = I_0 \;\mathrm{e}^{-<u_{\mathrm{G}}^2>G^2}, \tag{3.11}$$

where I_0 is the intensity of the crystal lattice at rest as described by Eq. 3.9 and $< u_{\mathrm{G}}^2 >$ is the average of the squared deviation of the atomic positions along $\vec{G}$. Such a deviation originates from phonons, quantised lattice oscillations, which are thermally excited at finite temperatures (at $T = 0$ so called zero point fluctuations can also be observed), i.e. the movement of atoms around their equilibrium positions rises with increasing temperatures [29]. It reduces the intensity because not all planes interfere constructively, accompanied by a rise of the background noise commonly known as thermal diffuse scattering [12].

All in all, we can say that the structure analysis with X-ray diffraction has essentially two parts. The form and dimensions, i.e. the lattice constants,are determined by measuring the position of Bragg reflections because of Eq. 3.8, the Laue condition for constructive interference, also reappearing in the discussion of the lattice sum. Besides, the content of the unit cell is derived from the intensity because with Eq. 3.9 the intensity of a (hkl) reflection reduces to:

$$I_{\mathrm{hkl}} = M^2 \; S_{\mathrm{hkl}}^2 \; \mathrm{e}^{-< u_{\mathrm{G}}^2 > G^2}, \tag{3.12}$$

where $\mathrm{e}^{-< u_{\mathrm{G}}^2 > G^2}$ is the Debye-Waller factor, M is the number of reflecting unit cells and S_{hkl} is the structure factor, containing information of the electron density and thus the position of atoms. In fact, the Fourier transformation of S_{hkl} gives the electron density which can not be calculated directly but with help of, for example, the Patterson function[5]. Furthermore we may conclude, that the scattering amplitude of an X-ray diffraction pattern itself is basically a Fourier transformation of the electronic charge density of the crystal [29].

3.2.7. Reciprocal space maps

To determine the structure of a crystal with X-ray diffraction we therefore have to measure the scattered X-ray intensity as a function fo the scattering vector $\vec{Q}$, mapping the whole reciprocal lattice. A reciprocal space map is the result and an example, of the (220)-reflection of $\mathrm{TbFe_2}$, is displayed in Fig. 3.7. There we see a local maximum of intensity in the q_{z}-q_{x}-plane, a slice of the $\vec{Q}$-space with fixed $q_{\mathrm{y}} = 0$. At the maximum, $\vec{Q} = (q_{\mathrm{x}}, q_{\mathrm{y}}, q_{\mathrm{z}}) = \vec{G}$, the Laue condition, is fulfilled, as it must be for every observed local maximum in the reciprocal space.

Theoretically, a complete picture of the reciprocal space can be obtained if every $\vec{Q}$ is realised by adjusting $\vec{k}$ and $\vec{k}'$ and measuring the intensity. In the reciprocal space to be formed, every reciprocal lattice vector $\vec{G}$ could be found because it gives the place of a local maximum of intensity (except for those reflections which are forbidden because of vanishing structure factors). Thus the reciprocal lattice can be depicted inside the reciprocal space, which is basically empty ($I(\vec{Q}) = 0$) except for those areas where $\vec{Q} \approx \vec{G}$. Knowing the reciprocal lattice, i.e. all possible $\vec{G}$, the real crystal lattice can be derived, because they are connected by a Fourier transformation.

In reality, $\vec{Q}$ has a supremum $|\vec{Q}|_{\max} = k^2$, because the X-ray wavelength is often fixed and because we only describe elastic scattering, it is always $|\vec{k}'| = |\vec{k}| = \frac{2\pi}{\lambda}$. Also, the reciprocal space is isomorphous to the real space $\mathbb{R}^3$ therefore dense. Thus, discrete measurements of $\vec{Q}$ vectors are only an approximation of the reciprocal space. Usually, only the areas around Bragg reflections are measured, because everywhere else, the signal would be near zero anyway. To set up different $\vec{Q}$, it is necessary to rotate the sample and place the detector in certain relation to the incident X-ray beam as $\vec{Q} = \vec{k}' - \vec{k}$. The precise implementation and data acquisition for the MFXT, BESSY II and PXS setup is documented in the respective sections 6.1, 6.2 and 9, repectively.

---

[5] The Patterson function provides a way to calculate the electron density which can be written as a three-dimensional Fourier series of the form $\rho(x, y, z) = \sum_{\mathrm{hkl}=-\infty}^{\infty} S_{\mathrm{hkl}} \cdot \exp[2\pi i (\vec{G}_{\mathrm{hkl}} \cdot \vec{r})]$. The problem with a simple Fourier analysis lies in the determination of the appropriate phases for S_{hkl}. The method of Patterson however, enables a direct determination of interatomic distances and their directions. This technique was introduced in 1934 by A. L. Patterson [30].

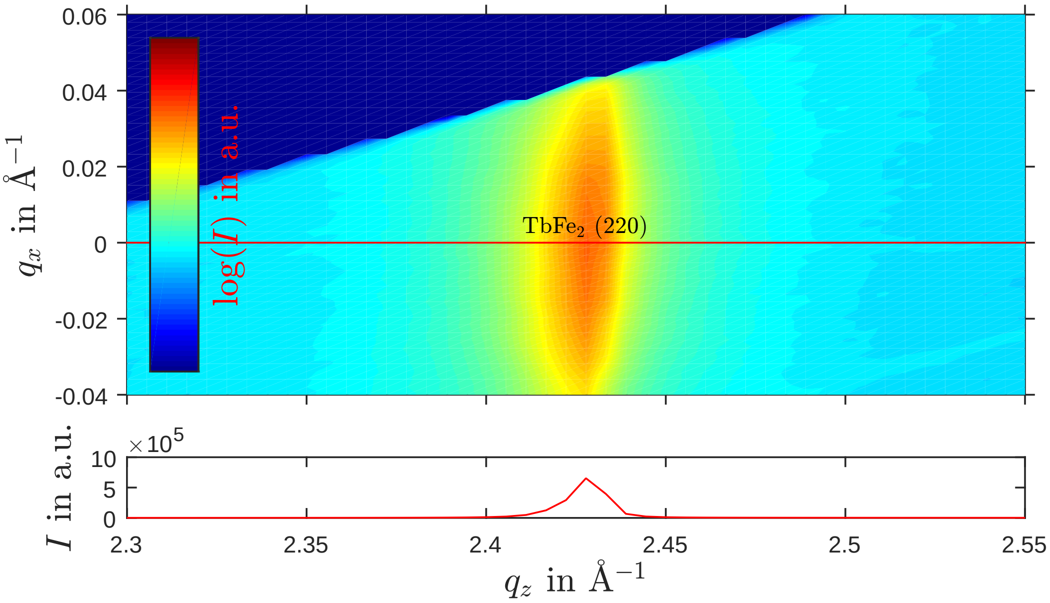

Figure 3.7: So called reciprocal space map (RSM) of the TbFe$_2$ (220) Bragg reflection. A slice of the reciprocal space at $q_\mathrm{y} = 0$ is depicted in the top colourplot. The blue area in the top left corner is an area of the RSM which was not scanned during the measurement, i.e. it is not a feature of the sample's reciprocal space. A slice along the q_z-axis (red line in the RSM) is plotted in the bottom plot, where $q_\mathrm{y} = q_\mathrm{x} = 0$. Apparently, the scattered intensity reaches its maximum at $q_\mathrm{z} \approx 2.43\,\text{Å}^{-1}$, where the Laue condition is fulfilled, associated with a lattice spacing of $d_{110} = 5.40\,\text{Å}$ or $a_{\mathrm{TbFe}_2} = 7.63\,\text{Å}$ according to Eq. 3.4 and 3.2. Compared to the literature value of $7.347\,\text{Å}$, a mismatch of four percent is registered here, which can be corrected by a more detailed calibration of the experimental setup. However, that is not necessary during the course of this thesis since mainly relative changes are examined in the following.

3.2.8. Summary of XRD signal interpretation

The previous short introduction to X-ray diffraction condenses into a set of features which can be seen if one is looking at one-dimensional X-ray diffraction patterns, such as the dependence of the intensity on a component of the scattering vector q_z in Fig. 3.7 or the diffraction angle ϑ in Fig. 3.4b. Mostly these kinds of plots are used to determine the interatomic distances in crystals, although they are in some cases one-dimensional projections of three-dimensional spaces defined by the spatial intensity distribution measured by X-ray detectors.

The following Fig. 3.8 provides a short summary of effects and processes inside the crystal lattice and how the diffraction pattern is influenced by them.

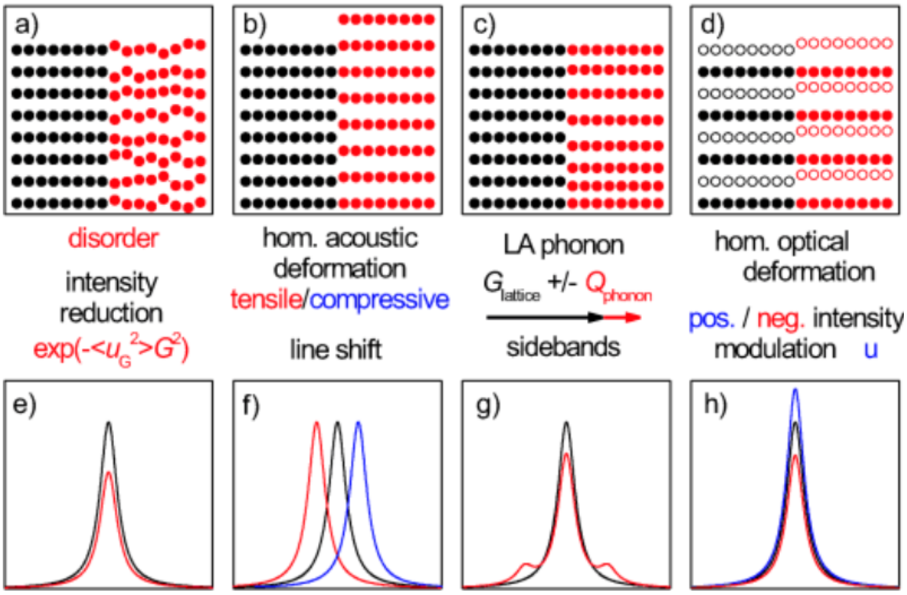

Figure 3.8: Variation of Bragg-peaks resulting from different types of distortions in the lattice taken from Bargheer et al. [29]. (a-d) are displaying the individual changes in the crystal planes, parallel to the reflecting surface, made up by atoms. (e-h) are visualizing changes of the associated reflections. Therefore the undistorted lattice and the changed lattices as well as their related Bragg reflections are pictured in black in red (or blue), respectively.

(a) and (e): A random disorder in the lattice due to motion of atoms at finite temperatures gives rise to the Debye-Waller factor $\mathrm{e}^{-<u_{\mathrm{G}}^2>G^2}$, which reduces the intensity of Bragg peaks with increasing temperature accompanied with an increased diffuse background.

(b) and (f): Homogeneous acoustic deformation of crystals are shifting the Bragg peaks, because the distance of reflecting planes changes. For a tensile or compressive deformation, the reflection shifts to smaller or higher reflection angles, respectively. This can be understood by recalling Bragg's law. The intensity does not change.

(c) and (g): Sidebands are appearing as longitudinal acoustic phonons, i.e. longitudinal lattice oscillations or sound waves, travel through the crystal. The Fourier-transformation-like relation between crystal lattices and their diffraction patterns can be seen here again. Convolving a periodically signal with another one, for instance the equidistant placing of atoms in the lattice with a periodically distortion of them, results in additional wave vectors in the Fourier spectrum, in this case additional peaks in the diffraction pattern. This can be described in the Laue formalism as the momentum of the phonon contributes in the scattering process as an extension or shortening of the reciprocal lattice vector.

(d) and (h): If optical phonons with $k = 0$ are excited in the crystal a negative or positive modulation of the intensity may be detected. This change can be related to a variation of the structure factor S_{hkl}, which varies as atoms are displaced in the unit cell. For $k \neq 0$, sidebands as in g) are to be expected.

4. Magnetism in TbFe_2

After the short introduction to crystallography, we now discuss the magnetic properties of TbFe_2. In combination of both topics lies the magnetostriction, the heart of this thesis. Therefore, I will shortly describe the origin of magnetism in TbFe_2, presenting the electronic configuration and the RKKY-Interaction. Furthermore the observation of a spontaneous macroscopic magnetization, is explained and underlined with multiple measurement results from different sources in the following sections.

4.1. Electronic configuration

The electronic configuration of terbium is $[\mathrm{Xe}](4f)^8(5d6s)^3$[12, p. 679], where the three $5d6s$ electrons are delocalised conduction band electrons in the Laves phase. One ion yields a magnetic moment of $\mu_{\mathrm{Tb}} = 9.0\,\mu_{\mathrm{B}}$ [8, p.6] which originates almost solely from the eight $4f$ electrons while a value of $\mu_{\mathrm{Fe}} = 1.6\,\mu_{\mathrm{B}}$ [26] is connected to the $3d$ electrons of the Iron sublattice. Iron has the electronic configuration $[\mathrm{Ar}](3d)^6(4s)^2$ and the $3d$ electrons of Fe participate in bonding to other atoms whereas the $4f$ charge cloud of Tb is localised at the nucleus and is screened by the conduction band electrons. The orbital of the $4f$ electrons looks like a pancake [14], which means it is oblate and has one preferential direction. This anisotropy is the origin of a magnetic anisotropy, see Sec. 5.1.2 and 5.4.

According to Hund's rules [12, p. 677], the rare earths are divided into heavy and light ones. In the light rare earths, the angular momentum $\vec{J}$ equals $\vec{S} - \vec{L}$, while it is the sum for heavy rare earths $\vec{J} = \vec{S} + \vec{L}$ as it is for Terbium in TbFe_2 [31]. For Tb the quantum numbers are $J = 6$, $S = 3$ and $L = 3$ and it is also important to note that a strong Spin-Orbit coupling is present [14]. It means, that $\vec{S}$ and $\vec{L}$ tend to align, which will result, in a reorientation of the anisotropic charge cloud of the $4f$ electrons, which is connected to $\vec{L}$, if the direction of the spin $\vec{S}$ is changing.

4.2. RKKY-Interaction and magnetic ordering

With the electronic configuration of Terbium in TbFe_2, it is possible to comprehend the magnetic properties of TbFe_2. Note at first that TbFe_2 is a ferrimagnet at room temperature [32], which means that the spins of the Iron ions are antiparallel to the spins of the Terbium ions. This leads to a net spontaneous magnetization, unlike an antiferromagnet. The ferrimagnetic nature of TbFe_2 can be understood by first recalling the RKKY exchange interaction together with the principles of spontaneous magnetization.

The $4f$ electrons contribute mostly to the large magnetic moment ($\mu_{\mathrm{Tb}} = 9.0\,\mu_{\mathrm{B}}$) of Terbium and are screened by conduction band electrons. Because the $4f$ electrons are located near the nucleus, they have no direct overlap with the $3d$ electrons of Iron. A direct exchange interaction between the spins of Tb $4f$ and Fe $3d$ electron is negligible due to the vanishing overlap of their wavefunctions. In 1971 Taylor wrote that the assumed exchange interaction is a simple RKKY mechanism as suggested by Wallace in 1968. [32].

The RKKY interaction is named after four scientists, M. A. Rudermann, C. Kittel, T. Kasuya and K. Yosida who described the interactions of stationary magnetic moments, like spins in solid state materials in their successively published work in 1954 [33], 1956 [34] and 1957 [35]. It is called a Two-Ion interaction because it explains the coupling of two neighbouring ions via a magnetization of the conduction band electrons. Thus it is an indirect effect and quantum mechanical calculations give an oscillating interaction strength (Fig. 4.1) which changes the sign of the Two-Ion interaction as a function of the distance. It means that two ions can have parallel spins while being at a certain distance to each other but if the distance between them is increased, the coupling can become antiparallel [36]. For TbFe_2 this model leads to the following pictorial view: the magnetic moment originating from the $4f$ electrons of Tb magnetise the conduction band electrons and they interact with the magnetic moment of the Fe $3d$ electrons. Because of the certain distance between Fe and Tb ions, the indirect coupling of the spins is of antiparallel nature, i.e. TbFe_2 is a ferrimagnet. The exchange interaction in TbFe_2 is described by an exchange Hamiltonian $\mathcal{H}_{\mathrm{ex}}$ [37, 38]:

$$\mathcal{H}_{\mathrm{ex}} = g\mu_{\mathrm{B}}B_{\mathrm{ex}}J_{\mathrm{z}}, \tag{4.1}$$

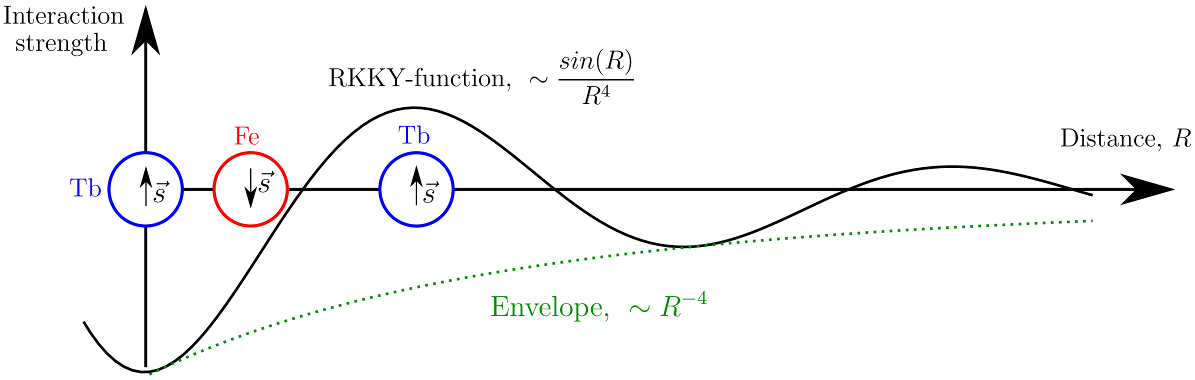

Figure 4.1: Pictorial view of the RKKY interaction and function with spins of terbium and the iron atom, adapted from Taylor [32, p.611]. The RKKY-function oscillates with the distance and reduces in strength by R^{-4}. Here, only the interaction function from the left terbium ion is depicted, coupling anti-ferromagnetic with the neighbouring iron ion, because the function is negative there. A ferromagnetic interaction persists with the neighbouring terbium ion on the right because the RKKY-function is positive at that distance R.

where g is the Landé factor, J_z the angular momentum of the rare earth ion and B_ex the magnetic exchange field, referring to the indirect interaction due to conduction band electrons, cf. Gross and Marx [12, p. 711]. The exchange Hamiltonian describes the energy of one ion resulting from the RKKY exchange interaction and will be used in Sec. 5.1.2.

4.3. Spontaneous magnetization

Since $\mathrm{TbFe_2}$ is a ferrimagnet, it exhibits a spontaneous macroscopic magnetization M_S, which is strongly temperature dependent. The spontaneous magnetization of the Tb and Fe sublattice as well as $\mathrm{TbFe_2}$ from various publications are displayed Fig. 4.2. Note, that at 0 K the measurements correspond well with the expected value of $\mu_\mathrm{Tb} = 9.0\,\mu_\mathrm{B}$. This magnetic moment can be translated into a net magnetization which equals $1.7\,\frac{\mathrm{A}}{\mathrm{m}}$, seen in the Figure at 0 K. In addition, the ferrimagnetic nature due to the RKKY interaction (Sec. 4.2) can be seen in Fig. 4.2, for example at 0 K:

$$M_\mathrm{TbFe_2}(0\,\mathrm{K}) = 1 \cdot 10^6\,\frac{\mathrm{A}}{\mathrm{m}} = 1.7 \cdot 10^6\,\frac{\mathrm{A}}{\mathrm{m}} - 2 \cdot 3.5 \cdot 10^6\,\frac{\mathrm{A}}{\mathrm{m}} \approx M_\mathrm{Tb}(0\,\mathrm{K}) - 2M_\mathrm{Fe}(0\,\mathrm{K}). \tag{4.2}$$

The temperature dependence shown in Fig. 4.2 is a well known phenomenon, see Ashcroft & Mermin [40]. Every ferro- or ferrimagnet has a Curie temperature at which it becomes paramagnetic. For $\mathrm{TbFe_2}$, T_C lies between 695 K [25] and 704 K [17]. Below T_C the spontaneous magnetization M follows a power law:

$$M(T) \propto (T_\mathrm{C} - T)^\beta, \tag{4.3}$$

with $\beta = 0.33(\dots)0.37$, which only applies for temperatures near T_C. Such a dependence appears in Fig. 4.2 and a theoretical derivation is explained in a few steps. At $T = 0$ all magnetic moments inside the crystal are aligned in one direction in the case of a ferromagnet. For $\mathrm{TbFe_2}$, all spins of the Fe and Tb sublattice are aligned, while the spins are antiparallel. This leads to a saturation magnetization m_S:

$$M_\mathrm{Tb}(0\,\mathrm{K}) \propto M_\mathrm{S} = g\mu_\mathrm{B}\frac{N}{V}S, \tag{4.4}$$

where g is the Landé factor, $\frac{N}{V}$ the atom-density and S the mean spin of each magnetic moment. If $T \neq 0$, the magnetization of all states has to be evaluated with a Boltzman factor $e^{-E/k_\mathrm{B}T}$. This leads to lower magnetization at finite temperature because of the excitation of spin waves. This process is dominant at low temperatures and it's magnetization reducing effect is called Bloch's $T^{3/2}$ law, which

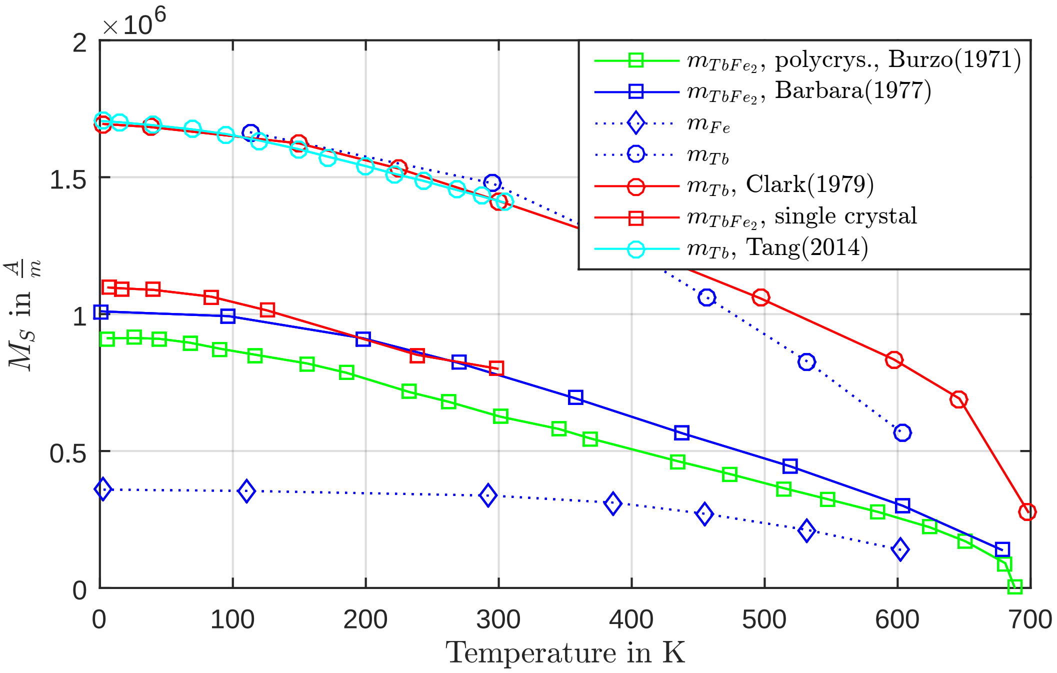

Figure 4.2: Literature values for the Temperature dependence of the spontaneous magetization of TbFe2 and its components. The data was taken from Bruzo [39], Clark [7], Tang et al. [26] and Barbara et al. [25]. The magnetization of the Iron and Terbium sublattice is depicted and one can see that the sum of the sublattice magnetization, evaluated with the ferrimagnetic nature, equals the net magnetization of $TbFe_2$. The magnetization shows a decrease to zero at a temperature of approximately 700 K, the Curie temperature.

states that the magnetization will differ from M_S by a value proportional to $T^{3/2}$ at low temperatures. Bloch's law transitions with rising temperatures to the empirical relation in Eq. 4.3.

4.4. Magnetic Domains, (cf. [40])

Although quantum mechanics predict a spontaneous magnetization in $TbFe_2$ at RT as in all ferro- or ferri-magnets below their Curie-Temperature, a macroscopic magnetization, i.e. the possession of a measurable external magnetic field is naturally non-existent. The reason is the magnetic dipole interaction of the material's spins. Between neighbouring spins, with a distance of some angströms, the RKKY exchange interaction occupies a dominant position as it is usually by a factor of 1000 stronger than the magnetostatic dipole interaction between magnetic moments. However, the impact of the RKKY interaction decreases much faster with rising distance as the dipole interaction does. While a parallel alignment of spins may minimise the RKKY interaction energy, a perpendicular or even antiparallel alignment of magnetic dipoles reduces the dipole interaction energy on the other hand. Thus it is energetically favourable to form magnetic domains with distinctive magnetization directions. In each domain, the exchange energy is minimised resulting in only one direction of magnetization (spontaneous magnetization) but concerning the whole sample, the dipole energy is minimised by many domains with different directions of magnetization. At the borders of domains, the exchange energy is admittedly increased but this is compensated by the relatively huge reduction of dipole interaction energy over the whole sample volume. Therefore, magnetic domains occur at sample sizes larger than the actual emerging domains which is for $TbFe_2$, 5 to 250 μm [41]. Most likely, our sample with a size of 5 mm times 5 mm times 500 nm will exhibit magnetic domains in-plane, but not in depth.

Despite the existence of magnetic domains in $TbFe_2$ it is possible to achieve a macroscopic magnetization. The domains are not fixed entirely, the borders between them (domain walls) can be moved to enlarge one domain to the benefit of another and thus removing the equilibrium of counteracting microscopic magnetizations. To move a domain wall, an external magnetic field B_{ext} must be applied to enhance one favourable orientation of spins. The response of a ferromagnet to an external field is strongly dependent on the state and properties of the domains and is usually depicted in so called hysteresis measurements. In Fig. 4.3 a schematic comparison between the magnetic response, i.e. the macroscopic magnetization M_{m}, of a single domain and a multi-domain specimen is shown if they are exposed to a variable magnetic field.

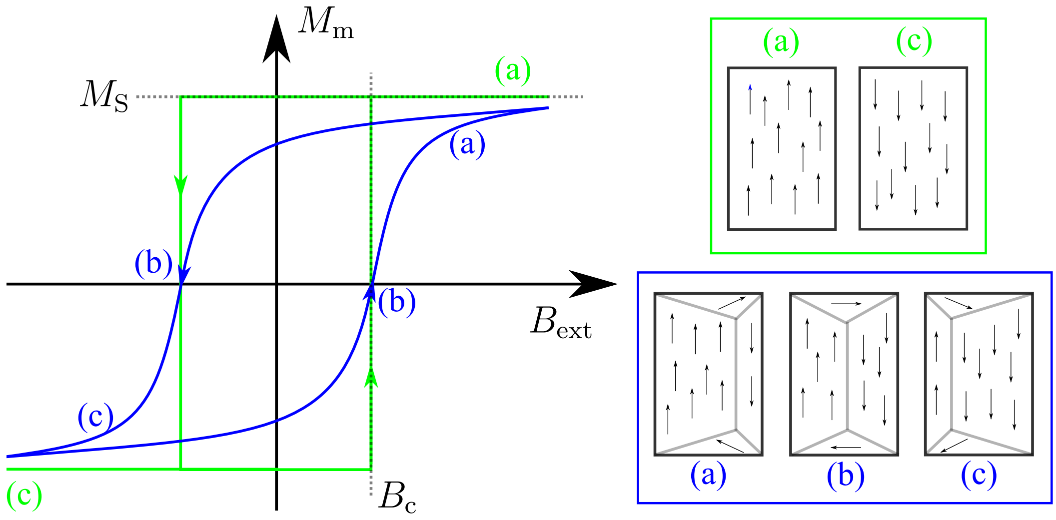

Figure 4.3: Sketch of hysteresis of single- (green) and multi-domain (blue) specimen, cf.[40]. The macroscopic magnetization M_{m} versus external magnetic field B_{ext} is displayed and commonly this response comes to light as the field is maximal at first (a), decreased to the negative maximum value (c) and back to the initial magnetic field. Going from (a) to (c), the top half of the hysteresis can be measured, accordingly following the arrows, from (c) to (a), the lower branch can be seen, completing one roundtrip, a hysteresis loop. A microscopic view of the magnetization state for associated points during the loop are depicted on the left side. Assuming only one domain (green), only two different states are possible and decreasing B_{ext} from (a) to be (c) switches the magnetization's sign at $-B_{\mathrm{c}}$ (coercive field). The way back looks similar, as M_{m} equals the spontaneous magnetization (M_{S}) all the way. Taking multiple domains into account (blue) results in a steadily decrease of M_{m}, vanishing at B_{c}, where all opposing domains are equally large, as the domain walls were moved ((a) to (b)). Further on, M_{m} decreases as the domain walls move on increasing the size of the aligned domain. At (c), M_{m} converges to $-M_{\mathrm{S}}$ not only by increasing the dominant domain even more but also by tilting the magnetization of the domains with an initial perpendicular magnetization direction in respect to the external field. Accordingly M_{S} is also called saturation magnetization, reached only for high magnetic fields. Completing the loop by going from (c) over (b) to (a) again shifts the domain walls and tilting the magnetization of not aligned domains towards the external field.

Hysteresis loop measurements therefore give information concerning the microscopic magnetic structure and were performed on $TbFe_2$ during the course of this thesis, see Sec. 7.1. Interestingly, the magnetic response of $TbFe_2$ is strongly dependent on the crystallographic axis originating from the anisotropy already mentioned in Sec. 4.1 and discussed in detail in Sec. 5.1.2 and 5.4.

5. Magnetostriction

Joule discovered magnetostriction of pure Iron in 1842 [1]. It is the relative change of volume V or length l caused by the change of the magnetization $\vec{m}$. The quantity λ is called linear magnetostriction or magnetostrictive constant and is defined by the relative change of l in one direction, for instance the (111) direction of a single crystal, when the magnetization is changed:

$$\lambda_{111} := \frac{l_{111}(\vec{m}_2) - l_{111}(\vec{m}_1)}{l_{111}(\vec{m}_2)} = \frac{\Delta l_{111}}{l_{111}}. \tag{5.1}$$

This magnetostrictive effect is two to three orders of magnitudes larger in $TbFe_2$ ($\lambda_{111,\mathrm{TbFe2}} = 2.4 \cdot 10^{-3}$ [42]) than it is in Iron ($\lambda_{111,\mathrm{Fe}} = -2.3 \cdot 10^{-5}$ [8]). Effects of the order 10^{-3} or larger are classified as giant magnetostriction and thus $TbFe_2$ has been such a popular subject for magnetostriction research and application for over 45 years now [2].

In addition, $TbFe_2$ and other alloys exhibit a change in the crystal lattice, below the Curie temperature, without applying an external magnetic field to change the magnetization. It is called spontaneous magnetostriction and its source is the spontaneous magnetization of the material, described in Sec. 4.3. The relationship between magnetization and magnetostriction is explained in Sec. 5.1 and 5.3. For now, I will focus on the existence and differentiation between polycrystalline and single crystal magnetostriction. To substantiate that, in Fig. 5.1 many measurements of magnetostriction are depicted. Not only spontaneous magnetostriction examined in single crystals, but also forced magnetostriction of polycrystalline $TbFe_2$ due to an applied field are displayed.

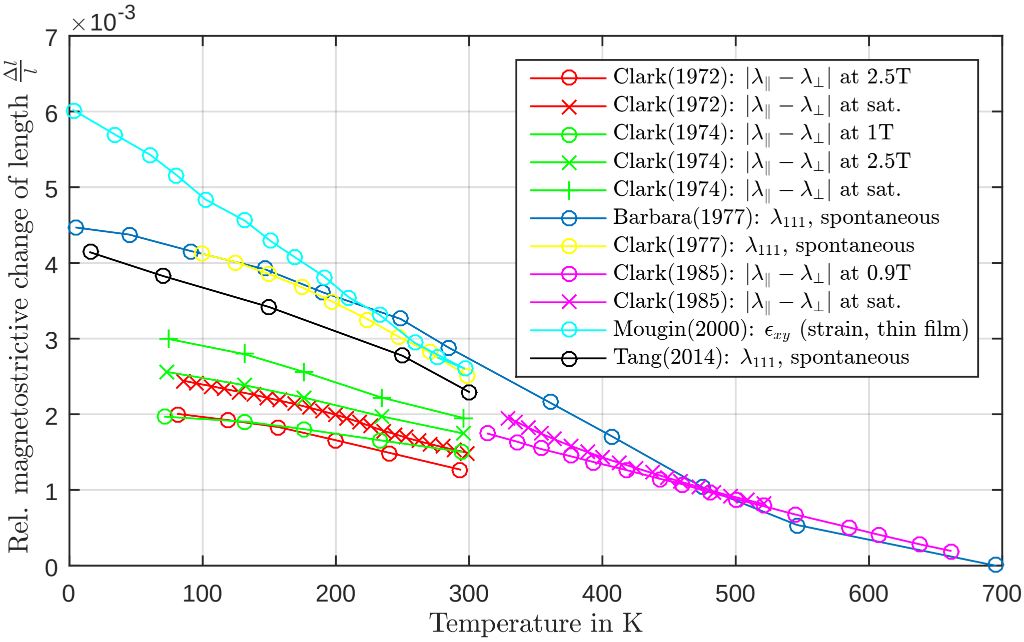

Figure 5.1: Spontaneous magnetostriction in $TbFe_2$: For polycrystalline materials $|\lambda_{\parallel} - \lambda_{\perp}|$ is the quantity of magnetostriction, Clark (et al.) 1972 [2], 1974 [43] and 1985 [44]. For single crystal $TbFe_2$ it is usually λ_{111}, as in Barbara et al. [25], Clark et al. (1977) [45] and Tang et al. [26]. Mougin et al. published a magnetostrictive and anisotropy strain term ϵ_{xy} of a thin film of $TbFe_2$ [46], plotted here for comparison. Some data was collected with an applied magnetic field. Generally the magnetostriction rises with the strength of the field up to a saturation (sat.) value of the magnetostriction. In Sec. 5.2.3, magnetostriction in polycrystalline materials caused by an external field will be described.

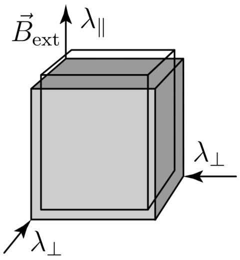

Figure 5.2: Polycrystalline magnetostriction, adapted from del Moral [47]

In polycrystalline $TbFe_2$, there is no distinguished [111] direction, which is why no spontaneous magnetostriction will appear below the Curie temperature. But by applying an external field $\vec{B}_{\mathrm{ext}}$, one direction is predetermined and magnetostriction will occur. There is a contribution, positive and parallel to the field $\lambda_{\parallel}$ and another, negative perpendicular $\lambda_{\perp}$, as one can see in Fig. 5.2 [2]. Therefore the material expands along to the magnetic field and contracts in the plane perpendicular to the applied field. In a single crystal there is also a contraction in the plane perpendicular to the (111) axis, but it is rarely discussed. For polycrystalline samples the only distinguished axis is given by the external field direction and the relationship between λ_{111} and $|\lambda_{\parallel} - \lambda_{\perp}|$ can be formulated. The latter is temperature dependent and is also determined by the strength of the external field. At saturation magnetization of the polycrystalline $TbFe_2$ however, the magnetostriction is also saturated and one can relate these two quantities by Eq. 5.2 [48]:

$$|\lambda_{\parallel} - \lambda_{\perp}| = \frac{3}{2}\lambda_{\mathrm{s}}, \tag{5.2}$$

with λ_{s} being the magnetostrictive constant at saturation. For a more detailed discussion, with a derivation of λ_{111}, λ_{s} and the exact relation between magnetization and magnetostriction see Sec. 5.2.2 and 5.3, respectively.

5.1. Theory of crystal field magnetostriction

A qualitative picture of magnetostriction can be obtained in the picture of crystal field magnetostriction. By applying an external magnetic field or varying the temperature of a magnetostrictive material, the magnetization may be changed. The reason why $TbFe_2$ shows strong magnetostriction is the anisotropic shape of the Tb $4f$ electron orbital and a strong spin-orbit coupling. It is known that the most part of the ionic magnetic moment originates from the spin of the $4f$ electrons. Also, the electron cloud in its special form can interact with the lattice via Coulomb interaction with the neighbouring atoms. Strongly coupling the spin system to the orbital system thus means to connect distortions in the lattice with the electron spins which make up the macroscopic magnetization. A scheme of this so called crystal field magnetostriction process is given in Fig. 5.3.

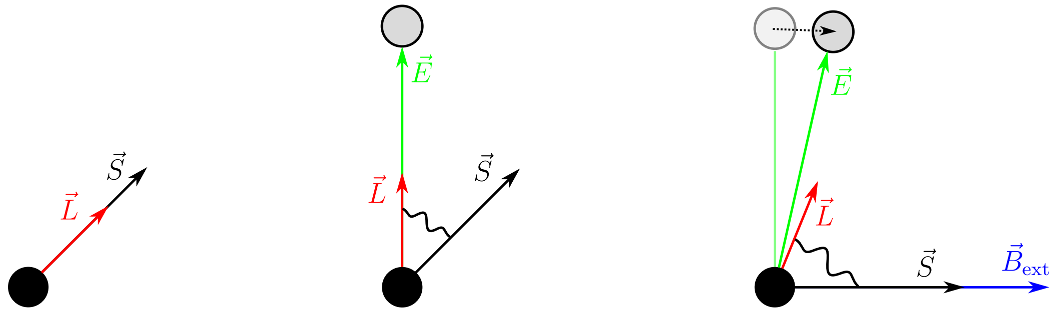

(a): Spin-orbit coupling **(b)**: Crystal field (Stark) effect **(c)**: Magnetic (Zeeman) coupling

Figure 5.3: Sketch of basic interactions responsible for magnetostriction, adapted from Dionne, 1979 [49]. **(a)**: The angular momentum of the spins $\vec{S}$ and the orbit $\vec{L}$ tend to align due to Spin-orbit coupling. **(b)**: Only the momentum of the orbit $\vec{L}$ interacts with the coulomb crystal field $\vec{E}$ of near atoms, called Stark interaction. **(c)**: The spins $\vec{S}$ can react to an external magnetic field $\vec{B}_{\mathrm{ext}}$, called Zeemann interaction and giving the orbit momentum $\vec{L}$ a tug to distort the lattice due to perturbation of the crystal field $\vec{E}$, resulting in a lattice distortion.

The picture of the crystal field magnetostriction establishes a qualitative connection between the magnetization and lattice change contained in magnetostriction. To calculate the latter and give predictions a balance of energy model is often applied. Containing all interactions in TbFe$_2$ and associating energy terms, a quantitative description can be obtained. There are five different terms to consider:

E_H , the *Zeeman energy*, associated with a magnetic moment in an external field,

E_A , the *magnetocrystalline anisotropy energy*, originating from crystal field and exchange energies,

E_ME , the *magnetoelastic energy*, a coupling energy between the magnetic and elastic system,

E_E , the *elastic energy* of a crystal, stored during deformations,

E_S , the external *stress energy*, added due to external compression or tension.

Together they form the total energy E_{total} of a magnetostrictive system which includes all interactions of impact on magnetostrictive effects:

$$E_{total} = E_\mathrm{H} + E_\mathrm{A} + E_\mathrm{ME} + E_\mathrm{E} + E_\mathrm{S}. \tag{5.3}$$

In this section, every energy term will be derived, explained and described to deduce magnetostriction through the appearance of E_{total}. The ground state of the equilibrated system is then determined by the minimum of its total potential energy E_{total}.

5.1.1. The Zeeman energy

The Zeeman E_H energy results from the response of a magnetic moment in a magnetic field. A magnetostatic potential energy can be associated with every magnetic dipole exhibiting a magnetization $\vec{M}$ inside an external field $\vec{B}_\mathrm{ext}$ [50]:

$$E_\mathrm{H} = -\vec{M} \cdot \vec{B}_\mathrm{ext}. \tag{5.4}$$

Thus if the dipole is aligned to the external field, the energy reaches a global minimum. If no alignment is present, the energy of the system will rise with the angle θ between $\vec{M}$ and $\vec{B}_\mathrm{ext}$. Thus, it is possible to change the direction of a magnetization by applying an external magnetic field, which I already mentioned in Sec. 4.4, where magnetic domains realign with an external field.

5.1.2. The anisotropy energy

To derive the anisotropy energy, I will follow the work of Atzmony and Dariel [37]. They took the One-Ion model from Callen and Callen [51], the fundamental theoretical model for magnetostriction in rare earth alloys (see Sec. 5.3), and constructed an Hamiltonian $\mathcal{H}_\mathrm{RE}$ for one rare earth ion. It includes the electrostatic and spin-orbit energy $\mathcal{H}_0$, the exchange energy $\mathcal{H}_\mathrm{ex}$ and the energy of the crystal field $\mathcal{H}_\mathrm{crys}$ which yields the interaction of the $4f$ electrons with the crystal field:

$$\mathcal{H}_\mathrm{RE} = \mathcal{H}_0 + \mathcal{H}_\mathrm{ex} + \mathcal{H}_\mathrm{crys}. \tag{5.5}$$

Assuming that $\mathcal{H}_0$ is not effected by neighbouring atoms, the interaction between atoms is approximated by an effective field described by $\mathcal{H}_\mathrm{ex}$ and $\mathcal{H}_\mathrm{crys}$. The complete anisotropy Hamiltonian per unit cell with N atoms in it is therefore given by:

$$\mathcal{H}_\mathrm{anis} = N(\mathcal{H}_\mathrm{ex} + \mathcal{H}_\mathrm{crys}). \tag{5.6}$$

A theoretical development of the Hamiltonians is described by Atzmony & Dariel, Hutchings and Bowden et al. which is not presented in this thesis [37, 38, 52, 53]. The phenomenological outcome however is a series expansion of the free energy which parametrises the Hamiltonian $\mathcal{H}_\mathrm{anis}$, introduced for cubic crystals by Becker & Döring in 1939 [54], see Eq. 5.7:

$$\begin{aligned} E_\mathrm{A} = K_0 &+ K_1(\alpha_\mathrm{x}^2\alpha_\mathrm{y}^2 + \alpha_\mathrm{y}^2\alpha_\mathrm{z}^2 + \alpha_\mathrm{z}^2\alpha_\mathrm{x}^2) \\ &+ K_2(\alpha_\mathrm{x}^2\alpha_\mathrm{y}^2\alpha_\mathrm{z}^2) \\ &+ K_3(\alpha_\mathrm{x}^4\alpha_\mathrm{y}^4 + \alpha_\mathrm{y}^4\alpha_\mathrm{z}^4 + \alpha_\mathrm{x}^4\alpha_\mathrm{z}^4) \\ &+ K_4(\dots), \end{aligned} \tag{5.7}$$

where E_A is the magnetocrystalline anisotropy energy, α_i are the direction cosines, i.e. the components of the unit vector of the magentization. They come into play, because both, $\mathcal{H}_\mathrm{crys}$ and $\mathcal{H}_\mathrm{ex}$, depend on the magnitude and direction of the magnetization. Furthermore, E_A rapidly decreases with a rise of temperature, described by the empirical bulk anisotropy constants K_i, which are displayed in Fig. 5.4.

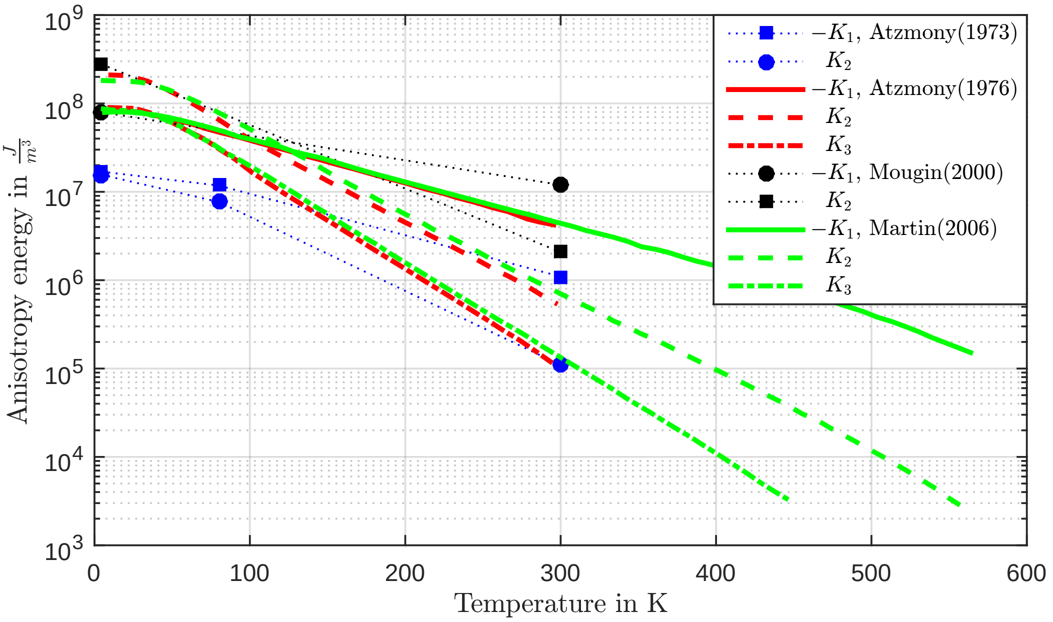

Figure 5.4: Anisotropy constants of $\mathrm{TbFe_2}$ as a function of the temperature. Atzmony and Dariel estimated the values of K_1 and K_2 first in 1973 for three temperatures [37]. They do not coincide well with the other data because the influence of the temperature on the exchange interaction was neglected. Subsequent calculations were one order of magnitude larger at 0 K and the data of Atzmony and Dariel from 1976 [52] matches with the values of Martin et al. [55] only with a small discrepancy. However, the experimental data from Mougin et al. [46] deviate at room temperature by a half of an order of magnitude. Note that on the one hand the data was given in $\frac{erg}{cm^3}$ or $\frac{K}{ion}$, with $10\frac{erg}{cm^3} = 1\frac{J}{m^3}$ and $\frac{8k_\mathrm{B}}{a^3}\frac{K}{ion} = 1\frac{J}{m^3}$. On the other hand, K_1 is always negative for $\mathrm{TbFe_2}$.

The ratio of the anisotropy constants as well as their sign are indicators for the easy magnetization direction of cubic Laves phase rare earth Iron compounds [46]. For example, if $K_1 < 0$ and $K_2 > 0$ as it is at every temperature for $\mathrm{TbFe_2}$, the easy magnetization direction is (111) or equivalent directions in cubic symmetry. In this context, 'easy' labels the direction in which the saturation magnetization M_S is reached at the smallest external magnetic field and thus determines the spontaneous magnetization direction of magnetic domains, as discussed in Sec. 4.4. Accordingly, the hard axis is the direction in which the saturation magnetization is reached only for large magnetic fields compared to the easy axis. The magnetocrystalline anisotropy energy thus describes the magnetization preferences of different crystallographic directions.

To understand this interpretation of E_A, it is useful to examine the interplay of the Zeeman energy and the anisotropy energy in a magnet with uniaxial anisotropy. A schematic two-dimensional single-domain magnet with distinguished easy and hard axis which is exposed to an external field is depicted in Fig. 5.5. In the situation on the left side of Fig. 5.5a, the Zeeman energy is zero since the external field is non-existent. The anisotropy energy is as $E_\mathrm{A} = -K\alpha_\mathrm{x}^2$, where $K > 0$ is an anisotropy constant. Thus E_A is minimised when $\alpha_\mathrm{x} = 1$, i.e. the spontaneous magnetization $\vec{M}_\mathrm{S}$ is entirely aligned with the X-direction, which is the magnetic easy axis. Applying a nonzero external field $\vec{B}_\mathrm{ext}$ along the hard axis however changes the situation since the Zeeman energy must be taken into account, see Fig. 5.5b. The scalar product $\vec{M}\cdot\vec{B}_{\mathrm{ext}}$ can be evaluated according to $E_{\mathrm{H}} = -M_{\mathrm{res}}B_{\mathrm{ext}}\cos\theta = -M_{\mathrm{res}}B_{\mathrm{ext}}\alpha_{\mathrm{y}}$ and thus the total energy of the system is:

$$E_{\mathrm{total}} = E_{\mathrm{A}} + E_{\mathrm{H}} = -K\alpha_{\mathrm{x}}^2 - M_{\mathrm{res}}B_{\mathrm{ext}}\alpha_{\mathrm{y}}, \tag{5.8}$$

without taking into account that the sample can distort via a strain. Minimising E_{total} with respect to θ, one will get:

$$B_{\mathrm{ext}}M_{\mathrm{res}}\sin\theta = 2K\sin\theta\cos\theta \quad\Rightarrow\quad \theta = \arccos\left(\frac{B_{\mathrm{ext}}M_{\mathrm{res}}}{2K}\right), \tag{5.9}$$

which is the angle the resulting magnetization of the sample $\vec{M}_{\mathrm{res}}$ will have to an external field $\vec{B}_{\mathrm{ext}}$, considering Zeeman and anisotropy energies, in contrast to $\vec{M}_{\mathrm{S}}$.

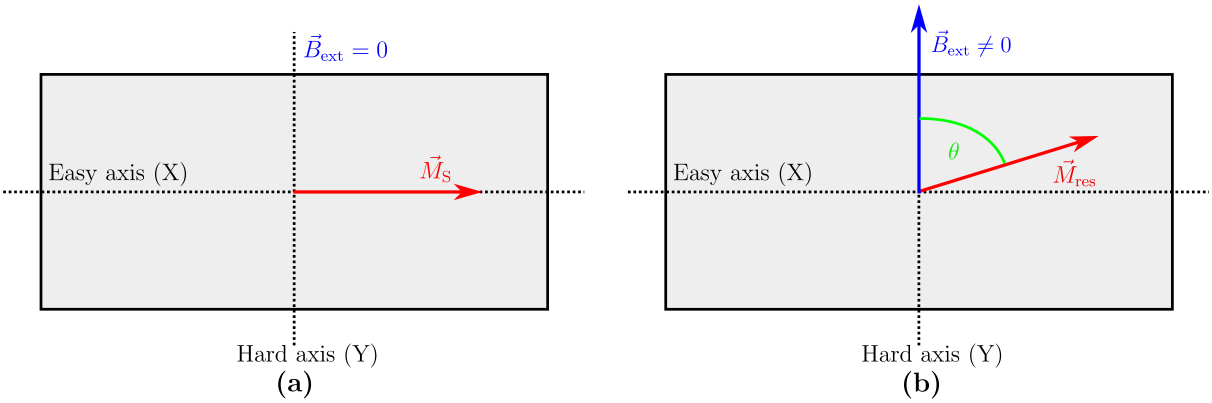

Figure 5.5: Scheme of a two dimensional single-domain sample (grey rectangle) with defined easy (X) and hard (Y) axis and resulting magnetization $\vec{M}_{\mathrm{res}}$ with **(b)** or with without **(a)** an applied external magnetic field, adapted from Engdahl [8]. In **(a)** the magnetization ($\vec{M}_{\mathrm{S}}$) is spontaneous aligned with the easy axis, minimising only the anisotropy energy as no external field is present. In **(b)**, the magnetization tilts towards the hard axis additionally minimizing the Zeeman energy since a magnetic field is applied along that direction.

5.1.3. The elastic and stress energy

The elastic energy is another important contribution to the presented model of magnetostriction. The quantity of the strain is essential for this energy contribution. The strain tensor ϵ_{ij} is defined bvia the displacements u_{i} of an atom along the coordinate i relative to the equilibrium position [12]:

$$\epsilon_{\mathrm{ij}} := \frac{1}{2}\left(\frac{\partial u_{\mathrm{i}}}{\partial r_{\mathrm{j}}} + \frac{\partial u_{\mathrm{j}}}{\partial r_{\mathrm{i}}}\right), \text{ with } \vec{r} = \begin{pmatrix} r_{\mathrm{x}} \\ r_{\mathrm{y}} \\ r_{\mathrm{z}} \end{pmatrix}. \tag{5.10}$$

A change of atomic distances manifests itself in form of a strain. These changes of length may result from external stresses σ applied to the solid. Hook's law states, the distortion coded in ϵ must be proportional to the applied stress, as the force $\vec{F}$ is to the elongation $\Delta\vec{l}$:

$$\vec{F} = -C\Delta\vec{l} \quad\leftrightarrow\quad \sigma = C\epsilon. \tag{5.11}$$

The spring constant C is called Young's modulus for solids. Just like the strain, the stress σ has a three dimensional interpretation. In one dimension it is the ratio of a force applied to an area $\vec{A}$, thus in solids:

$$\sigma_{\mathrm{ij}} := \frac{F_{\mathrm{i}}}{A_{\mathrm{j}}}, \text{ with } \vec{F} = \begin{pmatrix} F_{\mathrm{x}} \\ F_{\mathrm{y}} \\ F_{\mathrm{z}} \end{pmatrix} \text{ and } \vec{A} = \begin{pmatrix} A_{\mathrm{x}} \\ A_{\mathrm{y}} \\ A_{\mathrm{z}} \end{pmatrix}. \tag{5.12}$$

Composing the stress and strain 2nd-order symmetric tensors $\overleftrightarrow{\sigma}$ and $\overleftrightarrow{\epsilon}$, it is necessary to have a 4th-order elastic tensor $\overleftrightarrow{C}$ in place for connection:

$$\overleftrightarrow{\sigma} = \overleftrightarrow{C}\,\overleftrightarrow{\epsilon} \quad \Leftrightarrow \quad \sigma_{\mathrm{ij}} = \sum_{\mathrm{kl}} C_{\mathrm{ijkl}}\epsilon_{\mathrm{kl}}, \text{ with}$$
$$\overleftrightarrow{\sigma} = \begin{pmatrix} \sigma_{\mathrm{xx}} & \sigma_{\mathrm{xy}} & \sigma_{\mathrm{xz}} \\ \sigma_{yx} & \sigma_{\mathrm{yy}} & \sigma_{\mathrm{yz}} \\ \sigma_{zx} & \sigma_{zy} & \sigma_{\mathrm{zz}} \end{pmatrix} \text{ and } \overleftrightarrow{\epsilon} = \begin{pmatrix} \epsilon_{\mathrm{xx}} & \epsilon_{\mathrm{xy}} & \epsilon_{\mathrm{xz}} \\ \epsilon_{yx} & \epsilon_{\mathrm{yy}} & \epsilon_{\mathrm{yz}} \\ \epsilon_{zx} & \epsilon_{zy} & \epsilon_{\mathrm{zz}} \end{pmatrix}. \tag{5.13}$$

The elastic tensor in cubic materials, such as $\mathrm{TbFe_2}$ looks particularly simple due to many arguments of symmetry [56]. There are only three independent coefficients, C_{11}, C_{12} and C_{44} using the compressed Voigt notation[6]:

$$\overleftrightarrow{C} = \begin{pmatrix} C_{11} & C_{12} & C_{12} & 0 & 0 & 0 \\ C_{12} & C_{11} & C_{12} & 0 & 0 & 0 \\ C_{12} & C_{12} & C_{11} & 0 & 0 & 0 \\ 0 & 0 & 0 & C_{44} & 0 & 0 \\ 0 & 0 & 0 & 0 & C_{44} & 0 \\ 0 & 0 & 0 & 0 & 0 & C_{44} \end{pmatrix}. \tag{5.14}$$

Under an external stress $\overleftrightarrow{\sigma}$, a crystal is deformed by $\overleftrightarrow{\epsilon}$. The ratio of stress and the resulting strain is given by the elastic constants. The elastic energy stored in a distorted crystal can therefore be specified by Eq. 5.15, just like the potential energy of a stretched spring $C\Delta l^2/2$:

$$\begin{aligned} E_{\mathrm{E}} &= \frac{1}{2}C_{11}(\epsilon_{\mathrm{xx}}^2 + \epsilon_{\mathrm{yy}}^2 + \epsilon_{\mathrm{zz}}^2) \\ &+ \frac{1}{2}C_{12}(\epsilon_{\mathrm{xx}}\epsilon_{\mathrm{yy}} + \epsilon_{\mathrm{xx}}\epsilon_{\mathrm{zz}} + \epsilon_{\mathrm{yy}}\epsilon_{\mathrm{zz}}) \\ &+ \frac{1}{2}C_{44}(\epsilon_{\mathrm{xy}}^2 + \epsilon_{\mathrm{xz}}^2 + \epsilon_{\mathrm{yz}}^2). \end{aligned} \tag{5.15}$$

To deduce the external stress energy, let us recall the model of a linear compressed spring. The work W is needed to compress a spring. By the compression elastic energy from Eq. 5.15 is stored in the crystal. In the process of compression with a constant force F, the mechanical work is defined by Eq. 5.16 [58].

$$W := -\int F\,dl = -F\Delta l. \quad \leftrightarrow \quad E_{\mathrm{S}} = -\sigma\epsilon \tag{5.16}$$

For crystals, the variables corresponding to F and Δl are σ and ϵ, respectively. In one dimension, the external stress energy can therefore be written as showed and is of course zero when no stress is applied. In connection with the elastic term, the sum $E_{\mathrm{E}}+E_{\mathrm{S}}$ can be minimised as in Sec. 5.1.2, but now in respect to the strain ϵ under a certain applied stress σ. What will follow logically is a strain dependence of the stress and Young's modulus, as in Eq. 5.13: $\epsilon = C^{-1}\sigma$. This is shown in more detail in Engdahl's book [8].

Note that in many publications and in the following, values of so called Young's moduli are actually combinations of components of $\overleftrightarrow{C}$, for example in cubic crystals $C = \frac{(C_{11}-C_{12})(C_{11}+2C_{12})}{C_{11}-C_{12}}$ [59]. For polycrystalline samples of $\mathrm{TbFe_2}$ only an average can be given, $C = 9.4\,\frac{\mathrm{J}}{\mathrm{m}^3}$ [19]. The components of $\overleftrightarrow{C}$ are not available in the literature for $\mathrm{TbFe_2}$ but Clark and Belson stated that the elastic moduli of rare earth transition metal alloys can be considered equal for simplicity [2]. For $\mathrm{Tb_{0.3}Dy_{0.7}Fe_2}$, $C_{11} = 11.7$, $C_{12} = 4.02$ and $C_{44} = 3.84 \cdot 10^{10}\,\frac{\mathrm{J}}{\mathrm{m}^3}$ were measured [60], so similar values can be expected for $\mathrm{TbFe_2}$.

---

[6] Notation of Tensors introduced by W. Voigt in 1910 [57]. Because $\overleftrightarrow{\sigma}$ and $\overleftrightarrow{\epsilon}$ are symmetric tensors, there are only six independent entries: (xx), (yy), (zz), (xy), (xz) and (yz). Thus Voigt suggested to create a 1×6-vector instead of using the 2nd order tensors: $\overleftrightarrow{\sigma} \longmapsto \vec{\sigma}$ with the entries σ_{xx}, σ_{yy}, σ_{zz},σ_{xy},σ_{xz} and σ_{yz}. Applying the same for $\overleftrightarrow{\epsilon}$, $\overleftrightarrow{C}$ condenses into a 6×6-matrix, displayed in Eq. 5.14. In particular $C_{11} = C_{\mathrm{xxxx}} = C_{\mathrm{yyyy}} = C_{\mathrm{zzzz}}$, $C_{12} = C_{\mathrm{xxyy}} = C_{\mathrm{yyzz}} = C_{\mathrm{zzxx}}$, $C_{44} = C_{\mathrm{yzyz}} = C_{\mathrm{zxzx}} = C_{\mathrm{xyxy}}$, and every other entry equals zero.

5.1.4. The magnetoelastic coupling energy

Last but not least, the magnetoelastic energy must be described. It is the connection between the elastic energy from Sec. 5.1.3 and the energy due to the magnetocrystalline anisotropy in the undistorted lattice. E_{ME} describes therefore the interaction energy of the magnetic and elastic subsystems in magnetostrictive materials. The energy E_{ME} is deduced, in a similar way as E_{A} in Sec. 5.1.2, from the magnetoelastic Hamiltonian $\mathcal{H}_{\mathrm{me}}$ of Callen and Callen's One-Ion model (Sec. 5.3) and composed by the magnetization direction cosines α_{i} and the strains ϵ_{ij} to represent the magnetic and elastic response, respectively. The magnetoelastic coupling constants b_{i} come into play as the link [38, 46, 61]:

$$\begin{aligned} E_{\mathrm{ME}} &= b_1(\epsilon_{\mathrm{xx}}\alpha_{\mathrm{x}}^2 + \epsilon_{\mathrm{yy}}\alpha_{\mathrm{y}}^2 + \epsilon_{\mathrm{zz}}\alpha_{\mathrm{z}}^2) \\ &\quad + b_2(\epsilon_{\mathrm{xy}}\alpha_{\mathrm{x}}\alpha_{\mathrm{y}} + \epsilon_{\mathrm{xz}}\alpha_{\mathrm{x}}\alpha_{\mathrm{z}} + \epsilon_{\mathrm{yz}}\alpha_{\mathrm{y}}\alpha_{\mathrm{z}}). \end{aligned} \tag{5.17}$$

The original idea to write the magnetoelastic coupling in the form displayed in Eq. 5.17 was published by Kittel in 1949 [4]. He stated that the b_{i} constants "*may in principle be calculated knowing the details of the interactions in the solid*" [4, p. 556], for example E_{ME} depends on the deviation from sphericity of the $4f$ electrons [62]. Here they are also defined by an expansion of the anisotropy energy in Taylor's series of the strains, meaning:

$$\begin{aligned} \frac{\partial E_{\mathrm{A}}}{\partial \epsilon_{\mathrm{xx}}} &= b_1\alpha_{\mathrm{x}}^2; \quad & \frac{\partial E_{\mathrm{A}}}{\partial \epsilon_{\mathrm{xy}}} &= b_2\alpha_{\mathrm{x}}\alpha_{\mathrm{y}}; \\ \frac{\partial E_{\mathrm{A}}}{\partial \epsilon_{\mathrm{yy}}} &= b_1\alpha_{\mathrm{y}}^2; \quad & \frac{\partial E_{\mathrm{A}}}{\partial \epsilon_{\mathrm{xy}}} &= b_2\alpha_{\mathrm{x}}\alpha_{\mathrm{y}}; \\ \frac{\partial E_{\mathrm{A}}}{\partial \epsilon_{\mathrm{zz}}} &= b_1\alpha_{\mathrm{z}}^2; \quad & \frac{\partial E_{\mathrm{A}}}{\partial \epsilon_{\mathrm{yz}}} &= b_2\alpha_{\mathrm{y}}\alpha_{\mathrm{z}}; \end{aligned} \tag{5.18}$$

for cubic crystals. Callen and Callen claimed in their seminal publication [51] that b_{i} are temperature dependent, corresponding to their derivation where they are dependent on E_{A}. In Fig. 5.6 some anisotropy constants and magnetoelastic constant are summarised in one graph for comparison. Because α_{i} and ϵ_{ij} are unitless, both K_{i} and b_{i} have the units of energy density. Also, K_{i} contribute to the anisotropy energy in a product with potencies of α_{i} which have values between 0 and 1 while b_{i} are multiplied by potencies of α_{i} and ϵ_{ij}. The strains usually show values around 10^{-3} or smaller, which is why the product $b_{\mathrm{i}}\lambda_{\mathrm{s}}$ is plotted to provide an estimate of the energy distribution of the competing E_{A} and E_{ME}. λ_{s} is chosen as the quantity which measures the saturation strain due to magnetostriction. The K_{i} have a strong temperature dependence as their absolute values decrease up to three orders of magnitude from 0 to 300 K, whereas $b_2\lambda_{\mathrm{s}}$ stays rather constant with -11.6 to $-6.48 \cdot 10^5\,\frac{\mathrm{J}}{\mathrm{m}^3}$, being up to two orders of magnitude smaller than the anisotropy constants at 0 K and about the same at room temperature. Because the contribution of E_{ME} is relatively weak compared to E_{A} at low temperatures, the magnetization will be aligned along the easy magnetization direction (111), minimizing mainly the anisotropy energy. At room temperature however, a magnetostrictive shear strain can be observed in thin films of $\mathrm{TbFe_2}$ as the magnetoelastic contribution rises significantly [46].

An estimation of the energy density of the different contributions is provided by Clark et al. from 1973 [19]. For polycrystalline $\mathrm{TbFe_2}$ they report a value for the Young's modulus, $C = 9.4 \cdot 10^{10}\,\frac{\mathrm{J}}{\mathrm{m}^3}$, and in their work, C is multiplied by the saturation magnetostriction λ_{s} of polycrystalline $\mathrm{TbFe_2}$. It is made clear by Clark et al. that $\frac{1}{2}C\lambda_{\mathrm{s}}^2 = 1.45 \cdot 10^5\,\frac{\mathrm{J}}{\mathrm{m}^3}$ is an energy density which can be interpreted as the amount of magnetic energy which can be transformed to elastic energy per volume of $\mathrm{TbFe_2}$. The energy stored in a compressed spring looks accordingly, see Eq. 5.16 in 5.1.3. This amount of energy stored in the magnetoelastic system of $\mathrm{TbFe_2}$ is thousand times larger compared to other ferromagnetic materials like nickel.

Another magnetoelastic effect is the so called ΔE effect ($C = E$ means Young's modulus), which is the resulting change of Young's modulus because of an initial magnetization change, introduced by Mason in 1956 [63]. C is the ratio between the applied stress and the observed total strain. It is possible to change the strain and therefore C only due to a different magnetization, because of the coupling

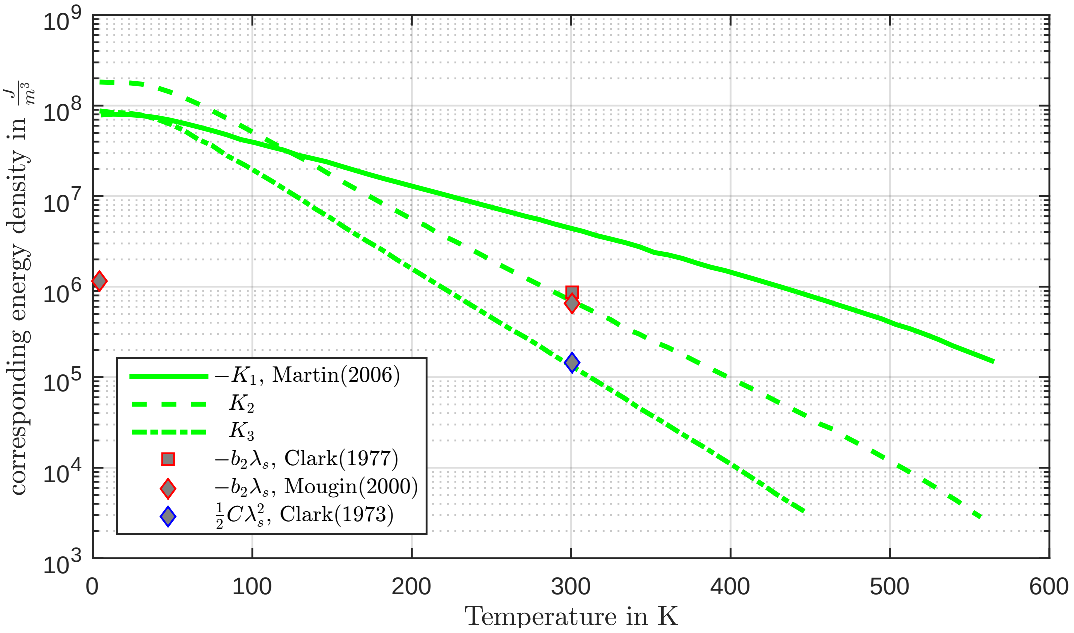

Figure 5.6: Anisotropy and magnetoelastical parameters of $TbFe_2$. K_1, K_2 and K_3 from Martin et al. [55] are the same as in Fig. 5.4. Values for $b_2\lambda_s$ are given by Clark et al. [45] and Mougin et al. [46] whereas b_1 was nowhere reported. The quantity $\frac{1}{2}C\lambda_s^2$ is a quantitative representatives of the energy stored in the elastic interactions described by E_E in Sec. 5.1.3 are depicted for comparison, taken from Clark et al. [19].

described by Eq. 5.17. The quantity to describe the strength of the ΔE effect is the ratio:

$$\mathcal{C} := \frac{\Delta C}{C_0} = \frac{C_0 - C_s}{C_0}, \tag{5.19}$$

where C_0 is the Young's modulus of the material without magnetization and C_s at saturation magnetization and thus magnetostriction. For $TbFe_2$, measurements showed that the ΔE effect is large with that due to magnetostriction. At 77 K, $\mathcal{C}$ equals 45% and at room temperature $\mathcal{C}$ reaches 55% while the sample is magnetised in a field of 2.5 T, which is not enough to reach a state of saturation [62]. In the publication of Clark et al. $C_0 = 5.9 \cdot 10^{10}\,\frac{\mathrm{J}}{\mathrm{m}^3}$ and $C_s = 11.1 \cdot 10^{10}\,\frac{\mathrm{J}}{\mathrm{m}^3}$ are given. This implies $\mathcal{C} = 90\%$, i.e. the elastic constant of $TbFe_2$ can be modified by 90% by applying a magnetic field [19].

Therefore, the ΔE effect leads to an increase of the sound velocity by 37% when the external magnetic field rises from zero to high fields as the sound velocity is given by $\sqrt{\frac{C}{\rho}}$, where ρ is the mass density of the material. Engdahl accordingly suggested to compare the Young's moduli for very high magnetic fields, at saturation, to make comparisons of different materials unambiguous. The magnetoelastic coupling softens the effective elastic constants below saturation as he shows in explicit calculations [8, 59].

5.1.5. Summary of and connection between the energy terms

Now all the energy terms can be summarised and used to calculate the magnetostrictive quantities via minimizing with respect to the strain and the magnetization direction. To recall all energies and their dependences, an overview is given to quickly see the connections in Fig. 5.7. With all that in mind, an actual calculation of the magnetostriction λ can be carried out.

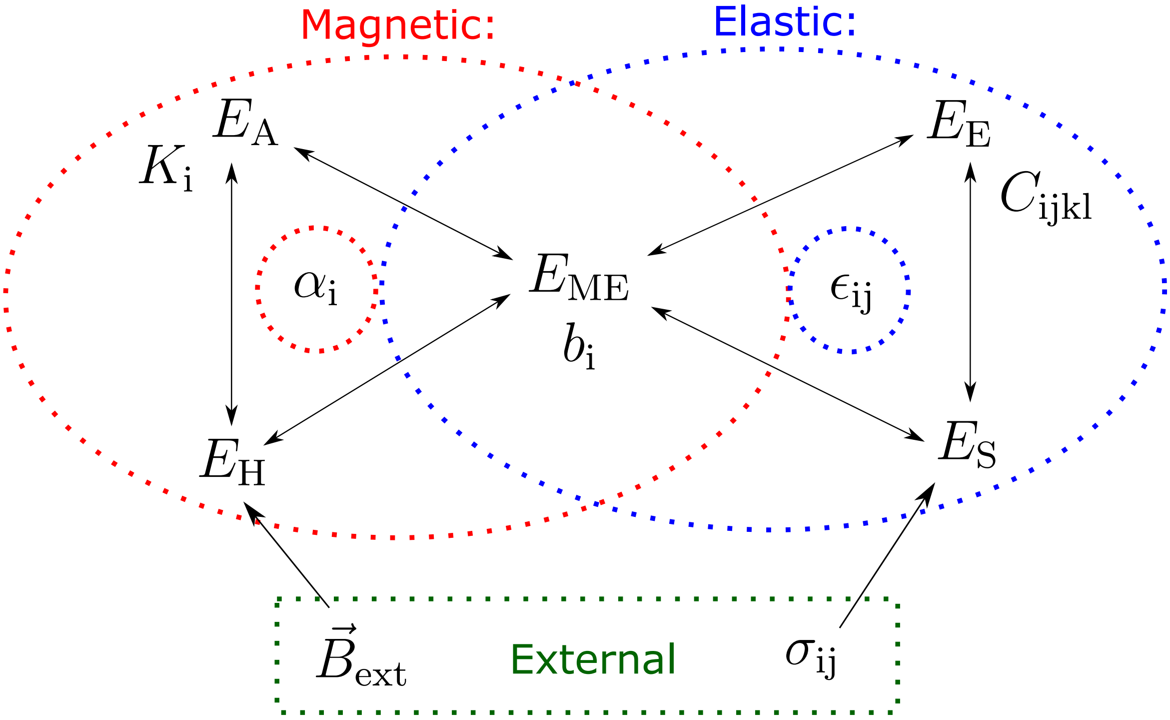

Figure 5.7: Pictorial view of all interaction energies participating in magnetostrictive effects in $\mathrm{TbFe_2}$. The energies are divided in magnetic (red) and elastic (blue) origin. One term the magnetic energy is the anisotropy energy E_{A}, dependent on the anisotropy constants K_{i} and the direction cosines α_{i}. The second magnetic term is the Zeeman energy E_{H}, arising from an external (green) magnetic field $\vec{B}_{\mathrm{ext}}$, interacting with the magnetization coded in α_{i}. The magnetoelastic energy E_{ME} builds the heart of magnetostrictive interactions, connecting α_{i} via the magnetoelastic constants b_{i} with the strain field ϵ_{ij}, which is the main quantity of the elastic system. The latter consists of the elastic energy E_{E} with its Young's modulus C_{ijkl} and the stress energy E_{S} originating from an external stress σ_{ij} applied to the system.

5.2. Magnetostrictive calculations

In this section, the sum E_{total} will now be used to calculate magnetostrictive effects in TbFe$_2$. This will explain forced and spontaneous magnetostriction in single crystal TbFe$_2$. To calculate for example magnetostrictive strains one has to minimize the total energy of the system.

5.2.1. The equilibrium strain

Assuming that no external field and no stress is applied to a magnetostrictive alloy ($E_{\mathrm{H}} = E_{\mathrm{S}} = 0$), there is still magnetostriction. It follows directly by minimizing the total Energy of this case with respect of ϵ_{ij} and because E_{A} does not depend on the strain, only $E_{\mathrm{E}} + E_{\mathrm{ME}}$ must be considered cf. [4]:

$$\begin{aligned} 0 &\overset{!}{=} \frac{\partial}{\partial \epsilon_{\mathrm{ij}}} \left[E_{\mathrm{E}} + E_{\mathrm{ME}}\right] \\ &= \frac{\partial}{\partial \epsilon_{\mathrm{ij}}} [\tfrac{1}{2} \left(C_{11}(\epsilon_{\mathrm{xx}}^2 + \epsilon_{\mathrm{yy}}^2 + \epsilon_{\mathrm{zz}}^2) + C_{12}(\epsilon_{\mathrm{xx}}\epsilon_{\mathrm{yy}} + \epsilon_{\mathrm{xx}}\epsilon_{\mathrm{zz}} + \epsilon_{\mathrm{yy}}\epsilon_{\mathrm{zz}}) + C_{44}(\epsilon_{\mathrm{xy}}^2 + \epsilon_{\mathrm{xz}}^2 + \epsilon_{\mathrm{yz}}^2)\right) \\ &\qquad + b_1(\epsilon_{\mathrm{xx}}\alpha_{\mathrm{x}}^2 + \epsilon_{\mathrm{yy}}\alpha_{\mathrm{y}}^2 + \epsilon_{\mathrm{zz}}\alpha_{\mathrm{z}}^2) + b_2(\epsilon_{\mathrm{xy}}\alpha_{\mathrm{x}}\alpha_{\mathrm{y}} + \epsilon_{\mathrm{xz}}\alpha_{\mathrm{x}}\alpha_{\mathrm{z}} + \epsilon_{\mathrm{yz}}\alpha_{\mathrm{y}}\alpha_{\mathrm{z}})]. \end{aligned} \tag{5.20}$$

There are six different ϵ_{ij} and each derivative of E_{total} has to be zero, which leads to:

$$\begin{aligned} 0 &= b_1\alpha_1^2 + C_{11}\epsilon_{\mathrm{xx}} + C_{12}(\epsilon_{\mathrm{yy}} + \epsilon_{\mathrm{zz}}), \\ 0 &= b_1\alpha_2^2 + C_{11}\epsilon_{\mathrm{yy}} + C_{12}(\epsilon_{\mathrm{xx}} + \epsilon_{\mathrm{zz}}), \\ 0 &= b_1\alpha_3^2 + C_{11}\epsilon_{\mathrm{zz}} + C_{12}(\epsilon_{\mathrm{xx}} + \epsilon_{\mathrm{yy}}), \\ 0 &= b_2\alpha_1\alpha_2 + C_{44}\epsilon_{\mathrm{xy}}, \\ 0 &= b_2\alpha_1\alpha_3 + C_{44}\epsilon_{\mathrm{xz}} \text{ and} \\ 0 &= b_2\alpha_2\alpha_3 + C_{44}\epsilon_{\mathrm{yz}}. \end{aligned} \tag{5.21}$$

Thus the equilibrium strains only depend implicitly on K_{i} via the direction cosines of the magnetization α_{i}. Only terms up to second order were considered because of their large size compared to higher order terms. The solutions of this linear system are:

$$\epsilon_{\mathrm{ij}} = \begin{cases} \dfrac{b_1(C_{12} - \alpha_{\mathrm{i}}^2(C_{11} + 2C_{12}))}{(C_{11} - C_{12})(C_{11} + 2C_{12})}, & \text{if } i = j, \\ \dfrac{-\, b_2\alpha_{\mathrm{i}}\alpha_{\mathrm{j}}}{C_{44}}, & \text{if } i \neq j, \end{cases} \tag{5.22}$$

the so called equilibrium strains which a magnetostrictive alloy will exhibit when not being exposed to a stress or magnetic field ($E_{\mathrm{H}} = E_{\mathrm{S}} = 0$). It is a magnetostrictive effect, because the equilibrium strains are a function of the magnetoelastic constants, which are only non-vanishing in magnetostrictive materials. This equilibrium strain may be interpreted as the spontaneous magnetostriction mentioned as a property of TbFe$_2$, shown in Fig. 5.1.

5.2.2. Magnetostrictive constants and Akulov's law

A possibility to describe magnetostriction macroscopically is presented by Becker and Döring who found in 1939 that magnetostriction λ_γ of cubic crystals along a certain direction of interest $\vec{\gamma}$ can be described by the Eq. 5.23 [54]. In his book, Engdahl uses the same description as Kittel [4, 8], and in the book of Bjelow [64] the following Eq. 5.23 is called as Akulov's law. Akulov published in 1930 two articles about magnetization and magnetostriction [3, 65], which contain equations basically equivalent to:

$$\lambda_\gamma = \frac{\Delta l_\gamma}{l_\gamma} = \frac{3}{2}\lambda_{100} \left(\sum_{\mathrm{i}}^{x,y,z} \alpha_{\mathrm{i}}^2\gamma_{\mathrm{i}}^2 - \frac{1}{3} \right) + 3\lambda_{111} \left(\sum_{i \neq j}^{x,y,z} \alpha_{\mathrm{i}}\alpha_{\mathrm{j}}\gamma_{\mathrm{i}}\gamma_{\mathrm{j}} \right), \text{ with } \vec{\gamma} = \begin{pmatrix} \gamma_{\mathrm{x}} \\ \gamma_{\mathrm{y}} \\ \gamma_{\mathrm{z}} \end{pmatrix}, \tag{5.23}$$

where α_{i} are the direction cosines of the magnetization and λ_{111} and λ_{100} are the magnetostriction constants, the saturation values for longitudinal magnetostriction along the (111) and (100) directions of cubic crystals. Equation 5.23 is used in the analysis of experimental measurements, because it can predict the magnitude of magnetostriction in any direction $\vec{\gamma}$, for a given magnetization. λ_{111} and λ_{100} can be expressed by the introduced magnetoelastic constants (b_i) and elastic constants (C_ij). To do so, one must write the relative change of length in a certain direction as a function of the strains (See Eq. 5.10) and the chosen direction:

$$\frac{\Delta l_\gamma}{l_\gamma} = \sum_{i \geqq j}^{x,y,z} \epsilon_\mathrm{ij}\gamma_\mathrm{i}\gamma_\mathrm{j}, \text{ (meaning } x > y > z). \tag{5.24}$$

Inserting the equilibrium strains from Eq. 5.22 into 5.24, the following relation can be obtained:

$$\begin{aligned}\frac{\Delta l_\gamma}{l_\gamma} =& - \frac{b_1}{C_{11}-C_{12}} \left(\sum_\mathrm{i}^{x,y,z} \alpha_\mathrm{i}^2\gamma_\mathrm{i}^2 - \frac{1}{3} \right) - \frac{b_2}{C_{44}} \left(\sum_{i \neq j}^{x,y,z} \alpha_\mathrm{i}\alpha_\mathrm{j}\gamma_\mathrm{i}\gamma_\mathrm{j} \right) \\ &+ \frac{b_1 \left(\frac{4}{3}C_{11} + \frac{2}{3}C_{12} \right)}{(C_{11}-C_{12})(C_{11}+2C_{12})} \underbrace{\sum_\mathrm{i}^{x,y,z} \gamma_\mathrm{i}^2}_{=1},\end{aligned} \tag{5.25}$$

which is basically Akulov's Eq. 5.23 if the last term is neglected because it is constant with respect to α_i and γ_i [4]. Thus, the magnetostrictive constants can be identified as:

$$\lambda_{100} := -\frac{2}{3}\frac{b_1}{C_{11}-C_{12}} \quad \text{and} \quad \lambda_{111} := -\frac{1}{3}.\frac{b_2}{C_{44}}. \tag{5.26}$$

5.2.3. Akulov's law applied to isotropic materials

Magnetostriction has been reported also in isotropic materials such as polycrystalline $\mathrm{TbFe_2}$ [4, 8], as shown in Fig. 5.1. It is described by the term $|\lambda_{\|} - \lambda_{\perp}|$. In isotropic samples, one does or can not distinguish between (100) and (111) direction, and therefore Akulov's law reduces with an average magnetostrictive constant λ_s to:

$$\begin{aligned}\lambda_{\gamma,\mathrm{poly}} = \frac{\Delta l_\gamma}{l_\gamma} &= \frac{3}{2}\,\lambda_\mathrm{s} \left[\left(\sum_\mathrm{i}^{x,y,z} \alpha_\mathrm{i}\gamma_\mathrm{i} \right)^2 - \frac{1}{3} \right] \\ &= \frac{3}{2}\,\lambda_\mathrm{s} \left[\cos^2\theta - \frac{1}{3} \right],\end{aligned} \tag{5.27}$$

with θ being the angle between the magnetization vector, coded in α_i, and the examined direction $\vec{\gamma}$. Equation 5.27 agrees with the data and discussion in Sec. 5, if we identify $\lambda_{\|}$ and $\lambda_{\perp}$ as $\lambda_{\gamma,\mathrm{poly}}$ at $\theta = 0$ and $\frac{\pi}{2}$, respectively. This implies:

$$\begin{aligned}\lambda_{\|} = \lambda_{\gamma,\mathrm{poly}}(\theta = 0) &= \frac{3}{2}\,\lambda_\mathrm{s} \left[\cos^2(0) - \frac{1}{3} \right] = \lambda_\mathrm{s} \\ \lambda_{\perp} = \lambda_{\gamma,\mathrm{poly}} \left(\theta = \frac{\pi}{2} \right) &= \frac{3}{2}\,\lambda_\mathrm{s} \left[\cos^2\left(\frac{\pi}{2} \right) - \frac{1}{3} \right] = -\frac{1}{2}\lambda_\mathrm{s} \\ \Rightarrow |\lambda_{\|} - \lambda_{\perp}| &= \frac{3}{2}\lambda_\mathrm{s},\end{aligned} \tag{5.28}$$

as already stated in Eq. 5.2. Note that $\lambda_\mathrm{s} < \lambda_{111}$ when comparing λ_s for polycrystalline and λ_{111} for a single crystal of $\mathrm{TbFe_2}$. Together with the Zeeman interaction as a function of $\vec{B}_\mathrm{ext}$ and α_i it is now clear, why $|\lambda_{\|} - \lambda_{\perp}|$ depends on the strength of the applied magnetic field.

5.2.4. Magnetostriction induced anisotropy energy change

Because of magnetostriction, the anisotropy energy will change and the difference can be calculated, cf. Kittel [4]. E_A will increase, because the derivation in Sec. 5.1.2 was given under the assumption that no distortion of the lattice is present. Would it be possible to hold the lattice, to clamp it, the experimentally deduced anisotropy constants and therefore the energy had a different look. In reality however, the spontaneous magnetostriction sets the lattice under constant stress producing a strain and thus changes the anisotropy energy. I.e. to first order:

$$K_1(\alpha_x^2\alpha_y^2 + \alpha_y^2\alpha_z^2 + \alpha_z^2\alpha_x^2) \longmapsto (K_1 + \Delta K_1)(\alpha_x^2\alpha_y^2 + \alpha_y^2\alpha_z^2 + \alpha_z^2\alpha_x^2). \tag{5.29}$$

To derive ΔK_1 one simply has to take the sum $E_A + E_E + E_{ME}$ from Sec. 5.2.1 and insert the equilibrium strains in a similar way as it was done in Sec. 5.2.1. After that, one has to replace the magnetoelastic constants b_i with the magnetostrictive constants according to Eq. 5.26 and it will follow:

$$\Delta K_1 = \frac{9}{4}\left[(C_{11} - C_{12})\lambda_{100}^2 - 2C_{44}\lambda_{111}^2\right]. \tag{5.30}$$

Paes and Mosca performed this calculation for a single crystal of TbFe$_2$, assuming $2.6 \cdot 10^{-3} = \lambda_{111} \gg \lambda_{100}$ (see Sec. 5.4) and therefore neglecting λ_{100} [61]. Setting $C_{44} = 11.5 \cdot 10^9\,\frac{\mathrm{J}}{\mathrm{m}^3}$, they calculated the effective first order anisotropy constant $(K_1 + \Delta K_1) = -3.5 \cdot 10^6\,\frac{\mathrm{J}}{\mathrm{m}^3}$ at room temperature. Taking their reference value $K_1 = -7.6 \cdot 10^6\,\frac{\mathrm{J}}{\mathrm{m}^3}$ (from Geshev et al. [42]), a strong decrease by almost 50 % is registered, originating from the magnetoelastic coupling.

5.3. The One-Ion Model

In which exact form the magnetostriction arises from a change in the magnetization was made clear by Callen and Callen in 1963 [51]. In their publications they displayed a theoretical model to connect the magnetization to the later measured magnetostriction of, for example, TbFe$_2$. It has many names, such as One-Ion, Single-Ion or Molecular-Field model and is used in many publications to the present day as justification and explanation for the appearance of magnetostriction in TbFe$_2$ [2, 7, 25, 26, 44, 43, 66, 67].

The One-Ion model is described in the original work of Callen and Callen as a restriction "*for the sake of analytic simplicity*" [51, p. 579], meaning they assumed the magnetoelastic coupling arises only from the "*interactions of single spins with the strain field*" [51, p. 579]. The sum of all those interactions contributes to the magnetoelastic Hamiltonian $\mathcal{H}_{me}$, on which the calculations of magnetostriction and other physical quantities are based. The approach is mainly of quantum mechanical nature, containing symmetry arguments, spin-operator functions, group theory and so called Tensor Cubic Operators and thus I will not elaborate the formalism in detail.

A simple consequence of the model is the following: It suggests a dependence of the magnetostriction on the magnetization in the following form:

$$\lambda_{111} \propto \mathrm{I}_{\frac{5}{2}}[\mathcal{L}^{-1}(m_R)] \approx m_R^3, \tag{5.31}$$

where $\mathrm{I}_{\frac{5}{2}}$ is the hyperbolic Bessel function, $\mathcal{L}^{-1}$ the inverse Langevin function and m_R is the reduced magnetization, see Eq. 5.32. The magnetostriction of a single crystal TbFe$_2$ along the (111)-axis is approximately proportional to the reduced magnetization m_R cubed. The reduced magnetization is of course temperature dependent as one can see in Fig. 4.2 and is defined by

$$m_R(T) = \frac{\mu_{Tb}(T)}{\mu_{Tb}(0\,\mathrm{K})}, \tag{5.32}$$

following Callen and Callen. Here, $\mu_{Tb}(T)$ is the mean magnetic moment one Terbium ion in the TbFe$_2$ crystal at a certain temperature T. Besides the power law, a more detailed relation between magnetization and magnetostriction lies in the term $\mathrm{I}_{\frac{5}{2}}[\mathcal{L}^{-1}(m_R)]$. $\mathrm{I}_{\frac{5}{2}}$, the hyperbolic Bessel function, is received due to quantum mechanical perturbation theory and internal field approximation and describes the temperature and magnetization dependence of the magnetostriction. To compare the theory with experimental data, the influence of the temperature has to be extracted, as realised by the inverse Langevin function $\mathcal{L}^{-1}$, giving a connection of T and m_R. Thus λ_{111} is a function of only m_R, which is indeed temperature dependent.

Looking at Fig. 5.8, a good agreement becomes apparent. The reduced magnetostriction $\lambda_{111,R}$, is plotted from two different publications by Barbara et al. [25] and Clark [7]. Magnetization data were published in the same articles as well, which I took to calculate $\lambda_{111,R}$ via the m_R^3 power law and the detailed One-Ion model $\mathrm{I}_{\frac{5}{2}}[\mathcal{L}^{-1}(m_\mathrm{R})]$. One can see the good agreement of the calculated dashed and dashed-dotted lines with the measured magnetostriction, indicated by the solid line.

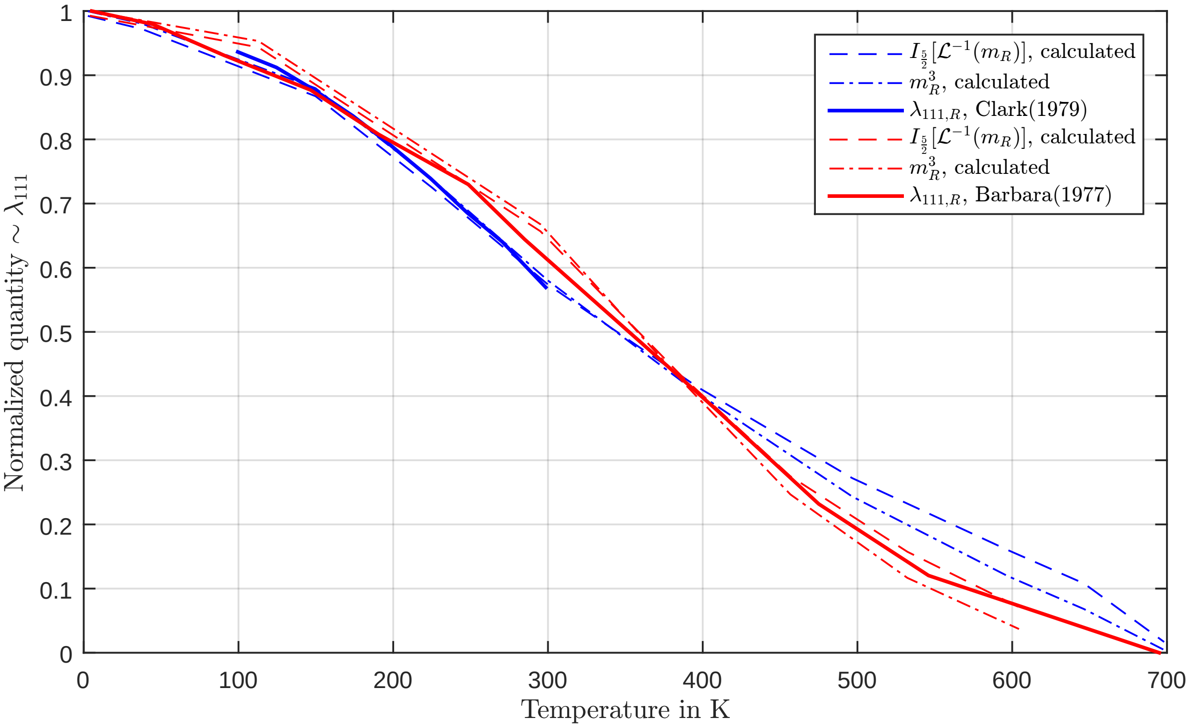

Figure 5.8: Reduced measured magnetostriction $\lambda_{111,R}$ and calculated values. To calculate $\mathrm{I}_{\frac{5}{2}}[\mathcal{L}^{-1}(m_\mathrm{R})]$ I took the graph of the function in [51, p. 587] and digitised it. The data was then fitted polynomial in m_R with an order of 4 which was used to calculate the values $\lambda_{111,R}$ for individual data points. A good agreement of the measured and the calculated magnetostriction can be seen as it is mentioned in the publications used.

5.4. Magnetostrictive anisotropy

The magnetostrictive constants of for example $\mathrm{TbFe_2}$ are highly anisotropic, which is confirmed experimentally by Cullen and Clark in 1977 [14, 44, 45]. In particular, $\lambda_{111} \gg \lambda_{100}$ with a ratio of more than $50:1$ [68]. They presented a simple model to explain this magnetocrystalline anisotropy.

Cullen and Clark claimed that this anisotropy arises from the shape of the $4f$ electron cloud which is realigned in an external magnetic field via spin-orbit coupling (see Sec. 5.1) and thus distorts the unit cell via coulomb interaction dependent on the alignment direction. This situation is depicted in Fig. 5.9 and thereby Cullen and Clark presented a plausible and graphic explanation for the highly anisotropic magnetostriction in $\mathrm{TbFe_2}$. However, Buck and Fähnle re-evaluated the situation in 1999 and found that the effects explained by Cullen and Clark are of minor importance considering the anisotropic magnetostriction. They calculated the magnetostrictive constants via an "*ab initio electron theory in local-density approximation with constraints for the 4f states and by the full-potential linear-muffin-tin-orbital method*", a theoretical approach [69]. They found that the intrinsic electronic structure is mainly responsible for the measured anisotropy in contrast to the developed explanation of Cullen and Clark. Nevertheless, I present the idea of Cullen and Clark as it is an comprehensive and intuitive example of a magnetostrictive process.

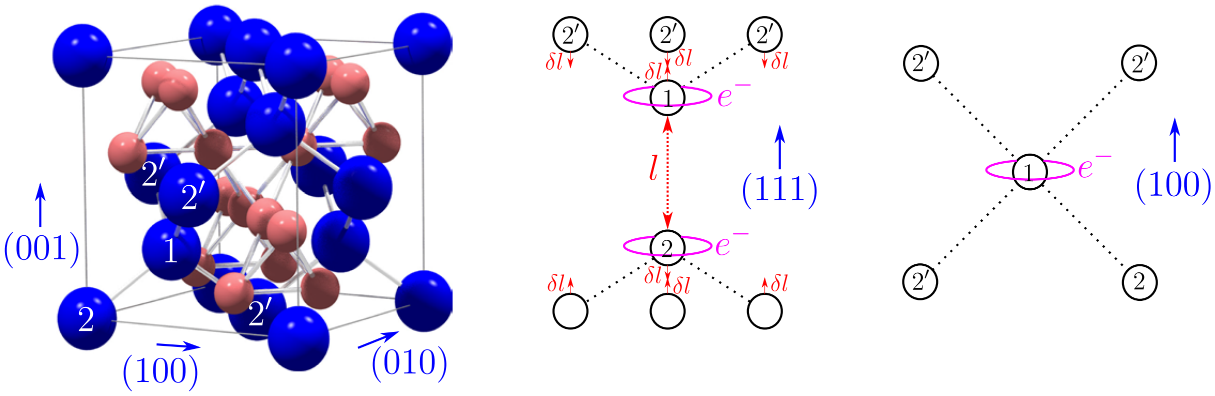

(a) **(b)** **(c)**

Figure 5.9: **(a)**: Sketch of the unit cell of $TbFe_2$ in which the blue spheres represent the Tb atoms and the red spheres the Fe atoms. The sketch is adapted from Bentall et al. [70] and three crystallographic axes are added as well as a numbering of several atoms used during the explanation of magnetostrictive anisotropy in (b) and (c). **(b)**: Two dimensional projection of a part of the unit cell, adapted from Cullen and Clark [71]. If applying a magnetic field along the (111) direction, the $4f$ electron orbitals of Tb atoms outlined around atom number 1 and 2 align as shown. Because of the electron cloud alignment, the $4f$ electrons of atom number 1 move closer to the atoms 2', but not closer to the remaining neighbouring atom number 2, resulting in a net coulomb attraction with the 2' nuclei. Consequently, a distortion δl occurs, pulling atom number 1 towards the atoms number 2'. The same applies for atom number 2 and three neighbouring atoms, according to the cubic symmetry. Ultimately, this results in an elongation of l, associated with λ_{111}. **(c)**: Two dimensional projection of a part of the unit cell, adapted from Cullen and Clark [71]. If applying a magnetic field along the (100) direction, the $4f$ orbital aligns as shown and the electrons of atom number 1 equally move closer to all 2' atoms and the atom number 2. Thus, the coulomb attraction is equally strong to each neighbouring atom and thus no distortion is present because the net coulomb force vanishes. This is associated with the significantly smaller λ_{100}.

Part II.
Forced magnetostriction measurements

Having introduced the basic relations leading to magnetostriction as well as X-ray diffraction I will now focus on experiments conducted by me as part of the UDKM group in order to get a better comprehension of magnetostriction in $TbFe_2$. The presented theoretical overview is used to predict the response of $TbFe_2$ when an external magnetic field is applied. This feedback is called forced magnetostriction since the distortions in the lattice due to magnetoelastic coupling can be enforced by the change of the magnetization which is coupled via the Zeeman interaction to the external magnetic field. In Part II, I show the following observations, measurements and simulations, which consist mainly of three distinguishable parts.

XRD measurements on the $TbFe_2$ sample were performed with the MFXT with a magnetic field of 150 mT and at BESSY II with a field of 550 mT where the field was applied parallel to the sample surface. The direction of the magnetic field was rotated in the plane of the sample surface within one measurement routine and a shift of the Bragg peak associated with the (110) set of planes were observed. A change in the lattice spacing d_{110} is related to that shift. The experiment shows that an out-of-plane distortion is caused by a rotation of a magnetic field in plane. The measured strain is linear in the strength of the applied magnetic field. ϵ_{110} was found to be $6 \cdot 10^{-5}$ at 550 mT and $1.7 \cdot 10^{-5}$ at 150 mT, which is the same ratio as the respective magnetic field strengths.

The qualitative response of the sample depends on the amplitude of the applied field. While ϵ_{110} has a sinusoidal dependence on β with a $360\,^\circ$ symmetry at the MFXT, the measured strain at BESSY II shifts back to zero after reaching its maximum around $\beta = 180\,^\circ$. Until that point, the strain follows the same path in both cases, reaching its maximum when the external magnetic field is aligned antiparallel to the initial magnetization. This shift is caused by the magnetic field of 550 mT which is sufficient to switch the magnetization of the sample, as shown by Vibrating Sample Magnetometer (VSM) measurements conducted in the group of K. Dumesnil at the IJL in Nancy, France. They show not only a coercive field of roughly 500 mT along the easy-axis in-plane, but also give the magnetization during a rotation of an external field with the strength of 550 mT.

Since the magnetization in the VSM-measurements also shows a switch, I work out a self-consistent model which is based on a simulation of the interplay of anisotropy energy and Zeeman energy by minimizing the energy of the magnetic system, it was possible to predict the magnetization state of the sample. From there, magnetostrictive calculations based on Akulov's law are used to predict the resulting strain. A fit can only be obtained under the assumption that magnetic domains are present in the sample. Such domains have been shown to exist by Sery et al. in bulk $TbFe_2$ [41]. The magnetization lies in one of two different directions (equivalent to the (111) direction because of cubic symmetry) in each domain, which are equally distributed over the sample. Thus, a macroscopic magnetization can be measured which is smaller than the spontaneous magnetization of single crystal $TbFe_2$. A qualitative agreement of simulated and measured strain is achieved, however the amplitude differs by a factor of 3 which is might indicate an epitaxial clamping to the substrate in thin films of rare earth alloys [18, 46, 80].

6. Experimental setup and data acquisition

The working principle of the MFXT and BESSY II is the same. In both cases X-ray diffraction is used to measure interatomic distances of the single crystal of the $TbFe_2$-sample and a magnetic field is applied to force magnetostriction. However, some differences lay in the exact implementation of the experiments. An overview of the setup parameters is given in table 6.1.

Table 6.1: Comparison of MFXT and BESSY II setup parameters

	Micro Focus X-ray Tube [72]	BESSY II-Beamline [73][7]
X-ray source	55 kV acceleration voltage, 600 μA electron current, 50 μm electron spot on Cu anode	dipole D13.1 magnet at the electron storage ring BESSY II
X-ray optics	poly capillary X-ray optics with HAPG-Monochromator, focusing to a $(5\,\mathrm{mm})^2$ spot with $5\cdot10^7\,\frac{\mathrm{photons}}{\mathrm{s}}$	*XPP-KMC3-Beamline*: parabolic mirrors and a double crystal monochromator, creating a $(350\,\mu\mathrm{m})^2$ focus with a flux of approximately $10^{11}\,\frac{\mathrm{photons}}{\mathrm{s}}$
Energy/wavelength	8.048 keV/1.54 Å (Cu-K_{α_1})	10 keV (Synchrotron)
Goniometer geometry	symmetrical (θ,2θ)	four circle diffractometer (ω,θ,ϕ,χ)
Detector System	*Pico Harp 300* (PicoQuant) scintillation point detector with photomultiplier and time correlated single photon counting module, 7 mm aperture diameter	*Pilatus 100k* (Dectris) fast read-out CMOS (complementary metal-oxide conductor) two-dimensional X-ray detector, 172 μm pixel size
Data handling	diffraction angle θ dependent intensity is measured, Bragg peaks are evaluated with respect on position, width and intensity	the diffraction angle set dependent 2D intensity portrait on the detector is transformed, into a three dimensional array $I(\vec{Q})$, several projections of the intensity to components of $\vec{Q}$ are evaluated with respect on position width and amplitude
External magnetic field	strength of approximately 150 mT (±30 mT), rotated indefinitely	strength of approximately 550 mT (±50 mT), rotated indefinitely

6.1. Micro Focus X-Rray Tube

A detailed description of the MFXT and its operation is given in my Bachelor Thesis [72]. It shows in addition that time-resolved measurements can be conducted with that setup as well, as the idea of the Bachelor Thesis project was to get a fully functional, small, simple and cost efficient way to conduct time-resolved X-ray diffraction in the UDKM group. In this work, the setup was used without time resolution to observe forced magnetostriction, thus the experimental setup, the functional principles and data handling are shortly summarised in the following.

---

[7] Web page directions: > Neutron and photon source > Photon source > Instruments BESSY II > List of Beamlines > XPP-KMC3-Beamline and > Neutron and photon source > Photon source > Electron Storage Ring BESSY II.

6.1.1. Experimental setup and functionality

The micro-focus X-ray tube is essentially a Coolidge tube, see Fig. 6.1a, where electrons are emitted by a filament and are accelerated into an anode as a result of an applied external voltage of 55 kV. The difference to the Coolidge tube lies in the fact, that the electron beam of 600 μA is focused on a spot with a 50 μm diameter. This leads to point-like source of X-rays, the major advantage of micro focus X-ray tubes over conventional ones.

Entering the anode material, in this case Copper, the electrons are decelerated emitting Bremsstrahlung, see Fig. 6.1b, a spectrum of light, reaching from zero to 55 keV. Along their way through Copper, some electrons collide with tightly bound electrons in the K shell of Cu atoms, ionizing the latter. During the transition of weakly bound electrons in the L shell to the hole in the K shell, monochromatic light known as X-ray fluorescence is therefore emitted, see Fig. 6.1c. There are as many discrete fluorescent lines as there are allowed transitions in the atoms, which can be seen in the spectrum. The selected transition line of the MFXT setup is the K_{α_1} line of Copper with an energy of 8.048 keV as it is the most intense part of the spectrum. Because of the electron beam's micro-focussing, the X-ray light is that of a point source and needs to be collimated. Capillary optics are therefore installed at the output of the tube which are made from microscopic hollow glass fiber bundles. A monochromator between the optics and the sample selects a certain energy or wavelength of the spectrum. In this case, it is diffracting HOPG[8] which guides the K_{α_1} light to the centre of the goniometer.

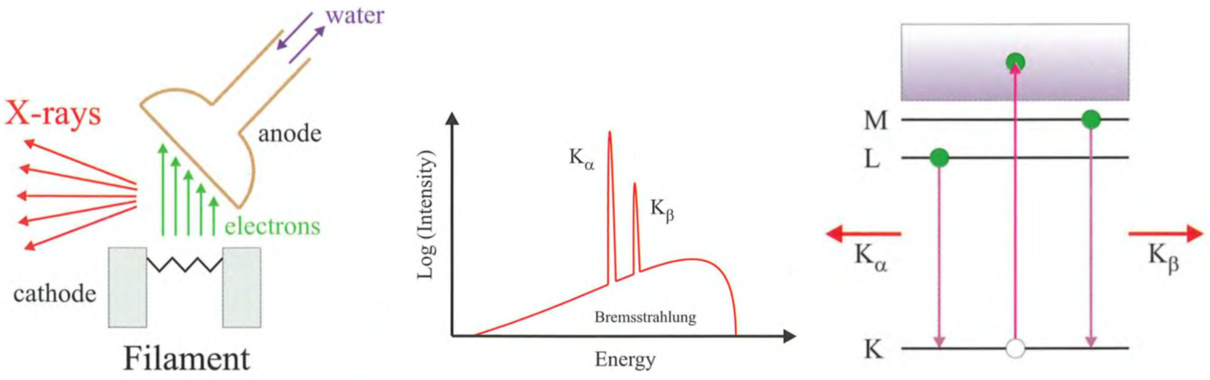

(a) (b) (c)

Figure 6.1: **(a)**: Sketch of a Coolidge X-ray tube, taken from Als-Nielson [23]. Emitted electrons from a filament are accelerated to the water cooled anode and emitting X-ray as they enter the anode. **(b)**: Simplified spectrum of a X-ray tube, taken from Als-Nielson [23]. It consists of the continuous Bremsstrahlung originating from decelerated electrons and the discrete fluorescent material dependent lines. **(c)**: Simplified energy scheme of atom with some possible electronic transitions, taken from Als-Nielson [23]. An atom can be ionised (middle) and L or M shell electrons can take the free place in the K shell, associated with discrete lines in the spectrum, called X-ray fluorescence.

There, the sample is mounted in front of a cylindrical magnet which results in a magnetic field of 150 mT in the sample plane, which can be rotated by the angle β as shown in Fig. 6.2a. The sample itself is rotated by the angle ϑ to diffract the incoming X-rays under angles which fulfil Bragg's equation 3.5. The detector with a 0.5 cm slit for screening scattered X-rays put in front of it, is set under the angle 2ϑ relatively to the incident X-ray beam. A top-view of the MFXT setup is schematically depicted in

---

[8] Highly Oriented Pyrolytic Graphite made purely from Carbon has a crystalline structure but is not a single crystal. It consists of many small single crystals with a grain size of circa 0, 2 mm, i.e. it has a mosaicity where the planes of the small grains are tilted relative to each other by a maximum of 0, 1 °. Thus using HOPG as a monochromator results in a higher intensity but the light is not monochromised as much as light from for example a silicon monochromator, because not only one wavelength at a time is fulfilling Bragg's equation but many. For more information, see the Optigraph GmbH web page [74].

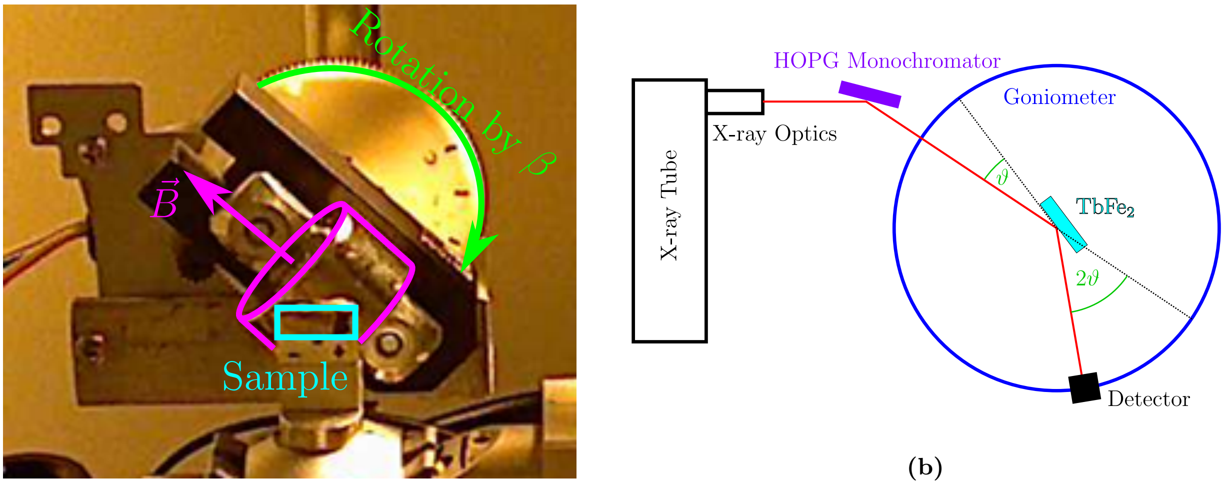

(a)

(b)

Figure 6.2: (a): Picture of the sample in the turquoise rectangle in front of the cylindrical magnet (violet outlined) centred and mounted on the goniometer. The stray field of the magnet along the cylinder jacket where the sample is placed is nearly homogeneous around 150 mT, measured with a Hall probe. The magnetic field will penetrate the sample only in-plane and can be rotated by β, indefinitely. **(b)**: Top view of the MFXT setup with the important parts; X-ray tube and optics to create a collimated X-ray beam, which is monochromatised and deflected by HOPG to the centre of the goniometer onto the sample penetrated by a magnetic field and finally diffracted to the detector.

Fig. 6.2b. Simply by rotating the sample by ϑ and the detector by 2ϑ after calibration, a $\vartheta/2\vartheta$-Scan can be performed and a possible result is depicted in Fig. 3.4b in Sec. 3.2.3. With Bragg's equation 3.5, the distance of the (110) planes can be derived from such scan.

6.1.2. Data acquisition and processing routine

Magnetostriction can now be performed and examined by applying and rotating a magnetic field in-plane of the sample. For those measurements, the sample was magnetised before the measurement in a homogeneous magnetic field of a permanent magnet with a strength of more than 1 T to assure the sample's state is the same at the beginning of each measurement. Afterwards, the sample was mounted in the centre of the goniometer while the magnetic field of the cylindrical magnet behind it pointed in the same direction as the magnetizing field of the 1 T magnet from before, again to assure the magnetization state of the sample stays the same. A $\vartheta/2\vartheta$-Scan can now be performed and the direction of the magnetic field in-plane was changed after each scan, i.e. β was varied in 45 ° steps, eight times per measurement loop to get the full 360 °.

The lattice spacing d_{110} of the (110) planes is calculated from the ϑ-position of the $TbFe_2$ (220) reflection from the $\vartheta/2\vartheta$-Scans via Bragg's equation. Equation 6.1 was used to calculate the COM of the $TbFe_2$ reflection, where every measured angle ϑ is linearly weighted with the corresponding intensity $I(\vartheta)$.

$$COM = \frac{\int_{\vartheta_1}^{\vartheta_2} I(\vartheta) d\vartheta}{\int_{\vartheta_1}^{\vartheta_2} d\vartheta}, \tag{6.1}$$

where ϑ_1 and ϑ_2 are angles defining the end of the $TbFe_2$ peak. It is not that important to know the exact values of ϑ_1 and ϑ_2 since we are only interested in relative changes in the COM, but the whole peak has to stay in between these two bounds and also has to be the only one. Looking at Fig. 3.4b, 16.5 ° and 18 ° are suitable bounds. This way, the COM of the $TbFe_2$ peak is measured as a function of the magnetic field orientation β. Repeating the measurement loop 30 times, the mean change in the $TbFe_2$ reflection' COM position because of magnetostriction could be examined, see Fig. 6.3. The corresponding lattice spacing shift in the MFXT and also BESSY II measurements are compared and discussed in Sec. 7, after the introduction of the BESSY II setup.

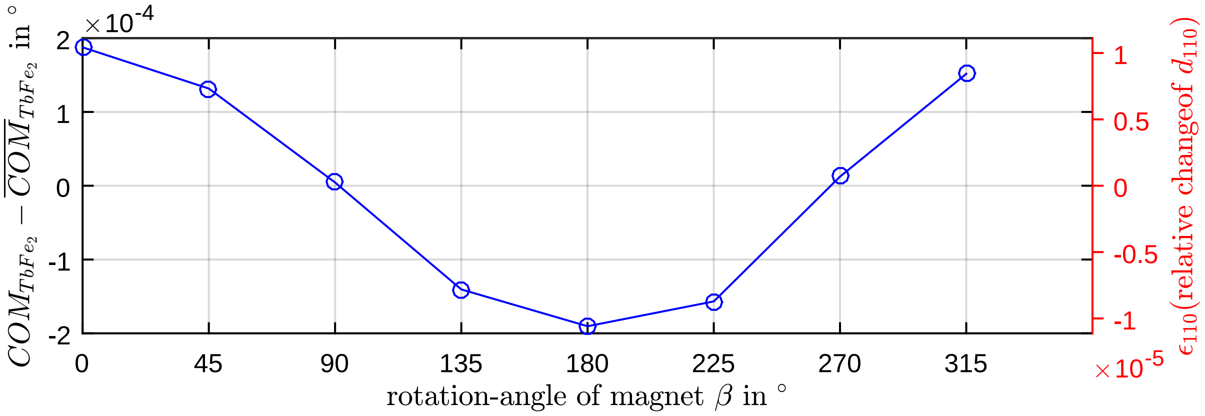

Figure 6.3: Absolute change in the COM position of the $TbFe_2$ reflection in relation to the mean value $\overline{COM}_{TbFe_2}$. At $\beta = 0\,°$, the applied field points in the same direction as the sample was magnetised before and there the COM position of the $TbFe_2$ peak has the lowest value. It follows the rotation of the magnetic field, reaching its maximum at $\beta = 180\,°$, where the applied field points in the opposite direction of the magnetization. After that, the COM of the peak converges back to the initial value performing a sinusoidal-like dependence. The change in the COM position of the Bragg peak is associated with a change of d_{110} which is indicated with the axis red on the right.

6.2. BESSY II Beamline

Thanks to the collaboration of the UDKM group at the University of Potsdam and the Helmholtz Zentrum Berlin (HZB) which operates the synchrotron BESSY II, it was possible to conduct not only similar measurements to the MFXT setup but also timeresolved XRD, discussed in Sec. III. Although the principles are the same as they are at the MFXT setup, BESSY II operates in many aspects on a much larger scale, i.e. higher X-ray intensity, size of source and amount of collected data.

6.2.1. X-ray source

BESSY II[9] is an electron storage ring with a circumference of 240 m in which preaccelerated electrons with an energy of 1.7 GeV are circulating with a current of 200 mA. They are guided by 32 deflecting or bending magnets through multiple insertion devices (usually Wigglers and Undulators) to supply roughly 50 beamlines with 50 ps X-ray pulses of enormous intensity.

In the centre of the BESSY II storage ring, an electron gun fires 70 keV electrons into a racetrack microtron which accelerates to 50 MeV. A Booster synchrotron fills the gap and accelerates the electrons to the 1.7 GeV electron beam energy [75]. When these high energetic electrons travel through a dipole magnet, i.e. a homogeneous magnetic field which is directed perpendicular to their current trajectory, not only will they be deflected in a circular manner due to the Lorentz-Force but they also will emit light as they are accelerated. The so called synchrotron radiation is radiated in a cone, see Fig. 6.4a, with the emitting electron as a point source and an opening angle proportional to $\frac{1}{\gamma} = \frac{cm_0}{E}$, where c is the speed of light, m_0 the mass of an electron and E the energy of the electrons. The spectrum of the syncrotron light from a bending magnet is continuous (Fig. 6.4b) [23].

---

[9] cf. [73] as all information in this section regarding BESSY II and the beamline is taken from this web page or otherwise is cited.

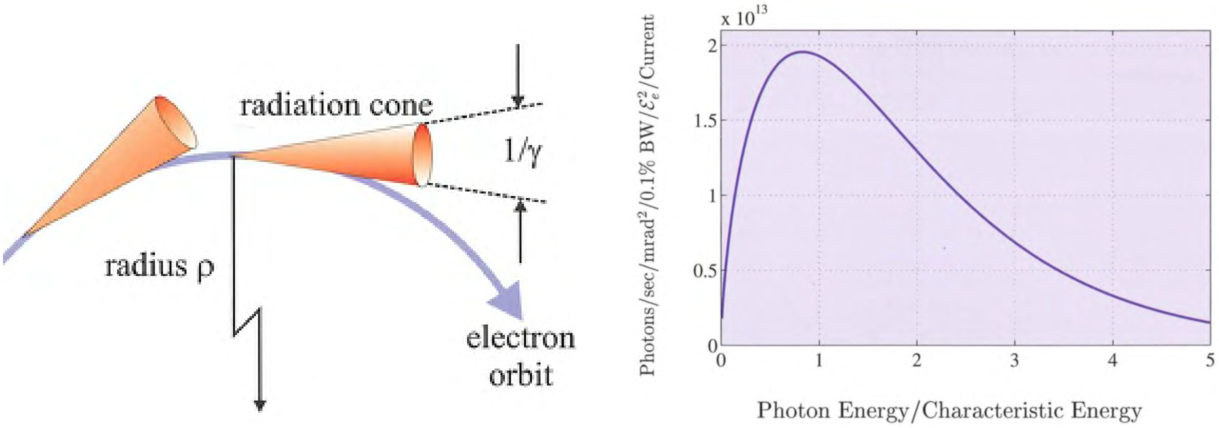

(a)

(b)

Figure 6.4: (a): Radiation cone originating from electrons accelerated on a circular arch with the radius ρ. The cone's opening angle is proportional to γ^{-1} and its axis is always parallel to the current trajectory of the electron, tangential to the circle. Taken from Als-Nielson [23]. **(b)**: Normalised energy dependent brilliance of a synchrotron radiation source. Brilliance is proportional to the flux ($\frac{photons}{s}$) but also normalised in terms of the solid angle ($mrad^2$), the bandwidth (0.1% BW), the energy ($\mathcal{E}^2$) and the current of the electron beam. Taken from Als-Nielson [23].

The dipole magnet used to supply this experiment with X-ray light is number D13.1, the front end of the XPP-KMC-3-Beamline which monochromatises and guides the light to the centre of the goniometer inside the experimental hutch to perform X-ray diffraction. A layout-plan of the beamline can be seen in Fig. 6.5. In all of the following measurements, the photon energy was set to 10 keV.

6.2.2. Goniometer setup and data acquisition

The centre of the four axis goniometer lies in the focal spot of the beamline. It is placed inside the experimental hutch in a vacuum chamber which can be used to perform XRD at low temperatures. A picture of the goniometer centre can be seen in Fig. 6.6a where θ is the angle of the detector in relation to the incident X-ray beam and ω, χ and ϕ are the angles by which the sample can be tilted and rotated in relation to the incident X-ray beam. In addition, the sample can be moved in every direction to ensure placing it in the focal spot of the beamline.

When varying only ω and θ in such manner that $2\omega = \theta$, a conventional $\vartheta/2\vartheta$-Scan can be performed. Decoupling ω and θ and varying χ and ϕ as well results in the possibility to detect asymmetrical reflections of the sample, meaning the reflection of a set of planes which does not lie parallel to the sample surface. In fact, this goniometer allows to map the reciprocal space as discussed in 3.2.7, because a much larger amount of scattering vectors $\vec{Q}$ can be achieved than in a simple $\vartheta/2\vartheta$-Scan. With the set of angles at this goniometer, basically every $\vec{Q}$ can be realised and an associated intensity can be measured creating a three dimensional reciprocal space map. In Fig. 6.6b one can see that four angles are sufficient to define the direction of the incoming and outgoing wave vector of the X-ray beam, K_i and K_h respectively. Therefore, their difference, i.e. $\vec{Q}$, can be calculated using Eq. 6.2, [77]:

$$\begin{aligned} q_x &= K(\cos\alpha_f \sin\theta_f + \cos\alpha_\mathrm{i} \sin\theta_\mathrm{i}) \\ q_y &= -K(\cos\alpha_f \cos\theta_f - \cos\alpha_\mathrm{i} \cos\theta_\mathrm{i}) \\ q_z &= K(\sin\alpha_f + \sin\alpha_\mathrm{i}). \end{aligned} \tag{6.2}$$

Considering Fig. 6.6b and Eq. 6.2 one has to keep in mind that the angles and also the transformation are not the same as they are at the XPP-KMC-3-Beamline but they are similar. To calculate $\vec{Q}$

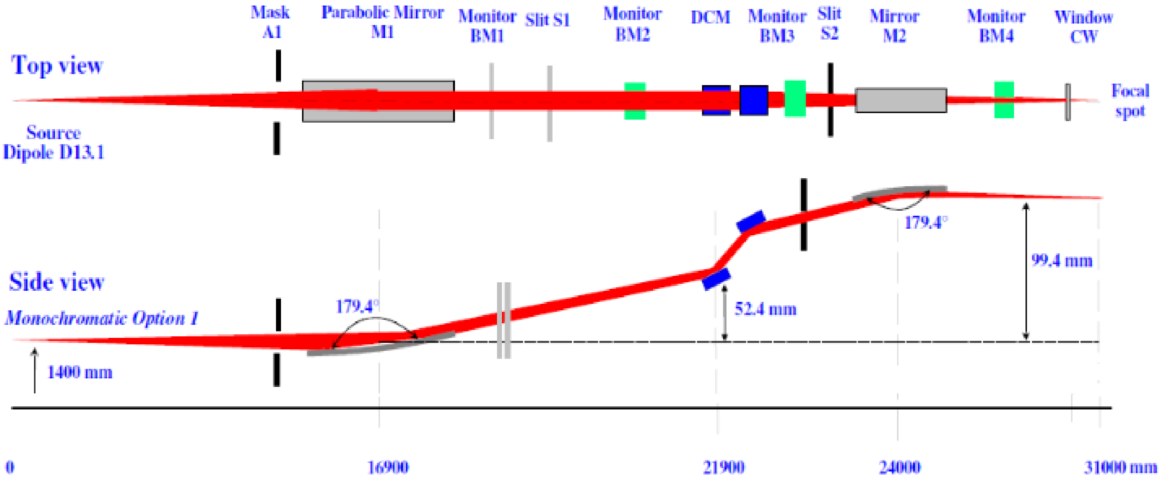

Figure 6.5: Top and side view of the 31 m long beamline and its elements which is supplied by the synchrotron light of the D13.1 Magnet at BESSY II. The Elements are: a mask (A1), to shield the beamline from scattered light inside of the storage ring, a parabolic mirror (M1) to collimate the cone of light vertically and horizontally and tilt it upwards by 0.6 ° through a monitor (BM1), a slit (S1) to select the desired fraction of the incoming beam and block everything else, into another beam monitor (BM2), followed by the double crystal monochromator (DCM) where symmetric XRD is used to select the desired energy for the experiment, a third beam monitor (BM3) and a slit (S2), a second parabolic mirror (M2), reversing M1 and a final monitor (BM4) in front of the window (CW) which acts as the transition from the ultra high vacuum of the storage ring and the beamline to the focal point centred in the goniometer.

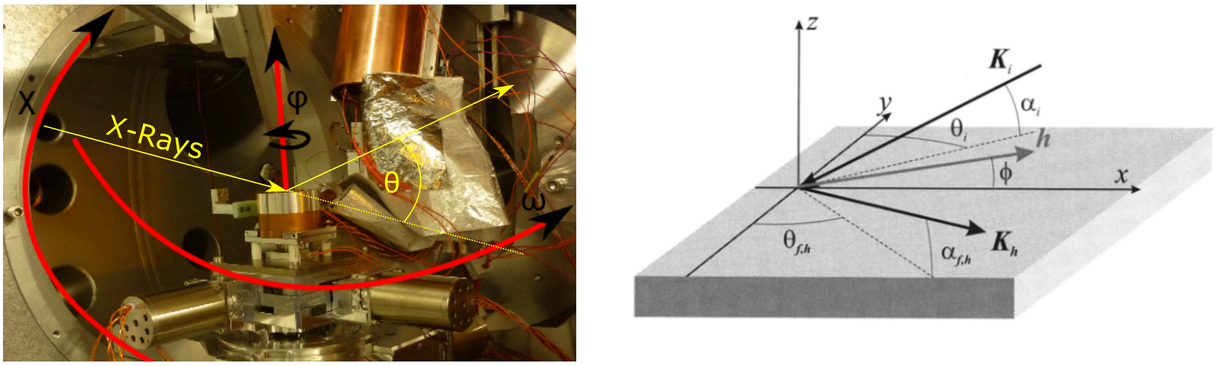

(a) **(b)**

Figure 6.6: **(a)**: Photo of the goniometer centre at the XPP-KMC-3-Beamline. The yellow solid line is the path of an X-ray beam diffracted by the angle θ at the sample. φ rotates the sample around the out-of-plane axis. χ rotates the sample around the direction of the incident X-ray beam and ω is the polar angle which rotates the sample around the same axis as the detector is rotated by θ. Taken from Reinhardt and Leitenberger [76]. **(b)**: Sketch of a diffracted X-ray beam on a surface with definition of all angles to define the scattering vector **h**, taken from Pietsch and Holý [77]. K_i and K_h are the incoming and diffracted X-ray beams respectively, $\theta_{\mathrm{i,f,h}}$ and $\alpha_{\mathrm{i,f,h}}$ are the associated diffraction angles. Together with Eq. 6.2, this set of angles equivalent to $(\theta,\omega,\chi,\phi)$ from Fig. 6.6a, can be used to calculate the scattering vector and map the reciprocal space.

from the set of angles the Python package *xrayutilities* is used, see [78]. It uses the same principles presented here and also considers the type of detector used at the experiment. It is a *Pilatus 100k* hybrid pixel area detector from Dectris [76] which is important because an area detector simultaneously measures different $\vec{Q}$, as a unique set of angles is associated with every different spot on the detector area.

All in all, this setup can be used to map areas of the reciprocal space, as *xrayutilities* gives the scattering vector $\vec{Q}$ and the associated intensity to every set of angles $(\theta,\omega,\chi,\phi)$ chosen. The instrument control and data acquisition software is called *spec*[10]. It allows to program crystal structure of the sample and its orientation in order to scan certain reflections automatically when handing over the scan parameters, i.e. $(\theta,\omega,\chi,\phi)$ and their range.

To examine magnetostriction, the sample was again magnetised before a magnetic field was applied in plane in the same manner as it was done in the MFXT setup. It has a strength of $(550 \pm 50)\,\mathrm{mT}$ and can be rotated in-plane by the angle β. The field is provided by two cubic magnets with a side length of 1 cm positioned on opposite sides of the sample. At the sample surface the magnetic field is nearly homogeneous.

6.2.3. Data processing and interpretation

For every β set up, a scan of the reciprocal space was performed. Therefore one Bragg reflection was chosen and scanned in every dimension of $\vec{Q}$ with the help of *spec*. The result is a three dimensional data set of the intensity distribution $I(\vec{Q})$, the reciprocal space map (RSM). Commonly a slice of the reciprocal space is shown, see Fig. 6.7, as the RSM is hard to visualize in its three dimensional form.

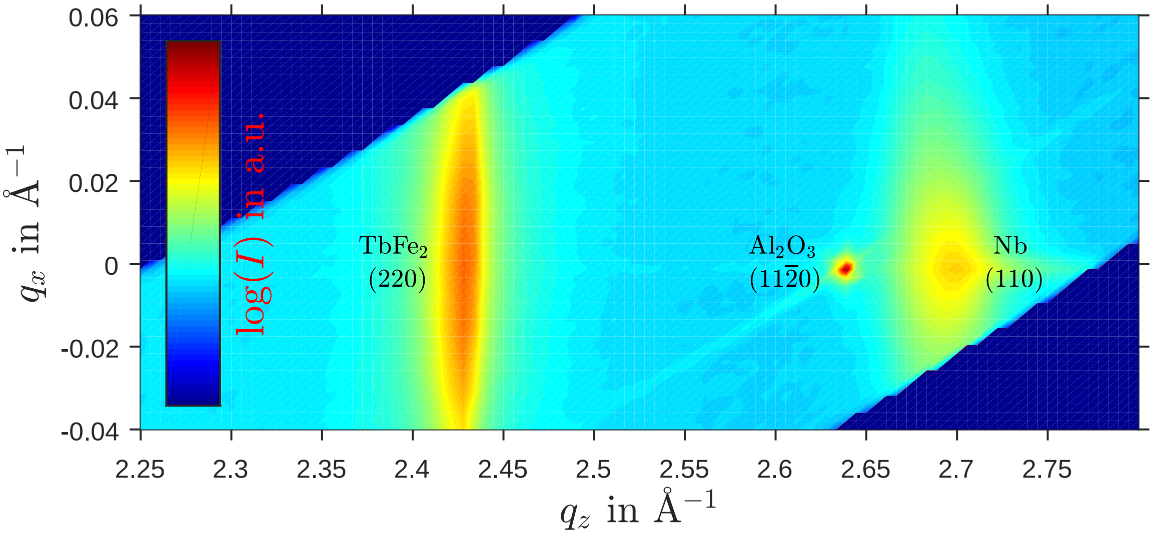

Figure 6.7: RSM: slice at $q_\mathrm{y} = 0$. One can see the reflections of the TbFe$_2$ (220), the Sapphire (11$\bar{2}$0) and the Nb (110) planes as local maxima of the intensity in the reciprocal space. Following the same algorithm as in Fig. 3.7 in Sec. 3.2.7, the reflection of TbFe$_2$ corresponds to the (220) set of planes which is parallel to the surface. The dark blue areas at the top left and bottom right are due to the angle range which was chosen at this particular scan. They are not an actual feature in the reciprocal space.

As the reflection of interest is the specular (220) reflection of TbFe$_2$, the peak can be integrated in q_x and q_y direction to get an intensity distribution along the q_z direction, which equals a $\vartheta/2\vartheta$-Scan. For asymmetrical reflections, the $\vec{Q}$-Space is rotated by *xrayutilities* to create an RSM that looks like one of a

---

[10] "*Spec is a UNIX-based software package for instrument control and data acquisition widely used for X-ray diffraction at synchrotrons around the world and in university, national and industrial laboratories.*", cf. [79].

specular reflection, such that the position of the intensity maximum only differs from zero in q_z direction. That makes the data processing considerably easier, because one can again just integrate over q_x and q_y and perform a COM calculation in one dimension instead of three.

This way, the length of the scattering vector with the maximum of the diffracted intensity can be derived for every direction of the magnetic field in plane. For this particular scattering vector, the Laue equation 3.8 is fulfilled and the length of $\vec{Q}$ equals mainly q_z and corresponds via Eq. 3.4 to the distance of the set of planes associated with the reflection. The calculated absolute and relative change of the lattice spacing from the scattering vector's length is displayed in Fig. 6.8 as a function of β. The calculated strain ϵ_{110} is compared with the data from the MFXT setup and is evaluated further in relation to theoretical predictions, simulations and magnetization measurements in the following sections.

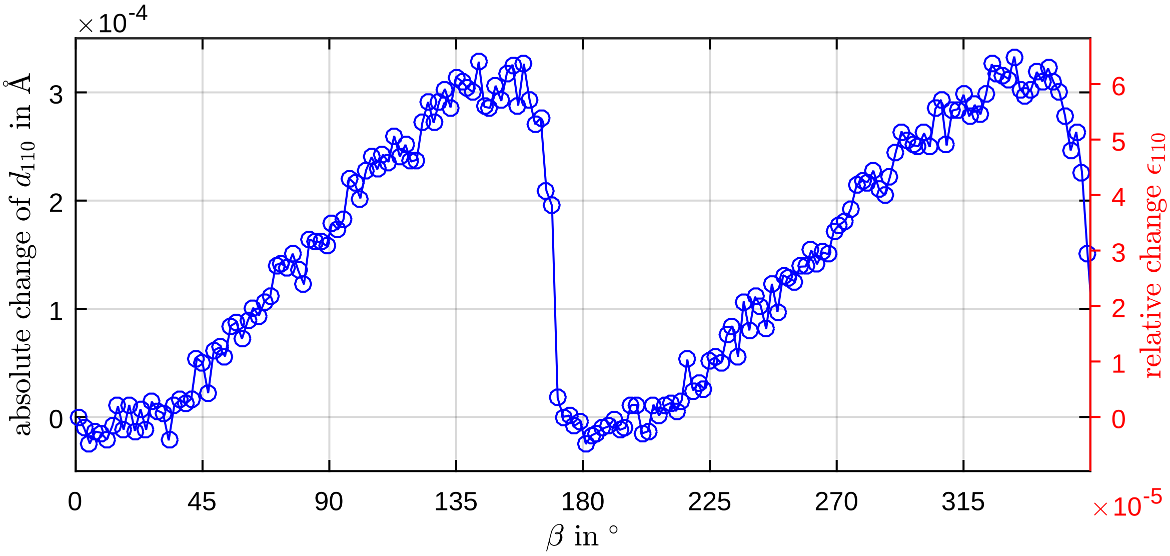

Figure 6.8: Corresponding absolute change of the lattice spacing d_{110} provided by the evaluation of the (220) reflection of $TbFe_2$ as a function of β, the angle of the applied magnetic field in plane. One can see that there is a strong dependence on the rotation of the applied magnetic field. At $\beta = 0\,°$, the spacing grows almost sinusoidal to a maximum around $\beta = 150\,°$ where the magnetic field in plane points almost to the opposite direction of the field with which the sample was magnetised before the measurement. At this point, a shift in the lattice spacing can be observed. Rotating the magnetic field even further repeats this observation periodically.

7. Comparison and Interpretation

The XRD at BESSY II and the MFXT yield the out-of-plane strain ϵ_{110} of $TbFe_2$ in dependence of an external in-plane rotating magnetic field. Also, I numerically calculate the expected strain with MATLAB and compare the results to the experimental outcomes. The measured and simulated results are displayed in Fig. 7.1. As the original data from BESSY II is displayed, the strain measured at the MFXT is normalised by the ratio of the applied magnetic fields $\frac{B_\mathrm{B}}{B_\mathrm{M}} = \frac{550}{150} \approx \frac{7}{2}$, to emphasise the similarities between the results. The response of the lattice as a result of the magnetostrictive interaction seems to be the same for both measurements during the first 150 °, in which the strain is normalized by the magnitude of the applied field. The simulated strain shows a good qualitative agreement in both cases, although it is likewise normalised by a factor of three. This discrepancy might indicate the well documented epitaxial clamping to the substrate in thin films of rare earth alloys [18, 46, 80].

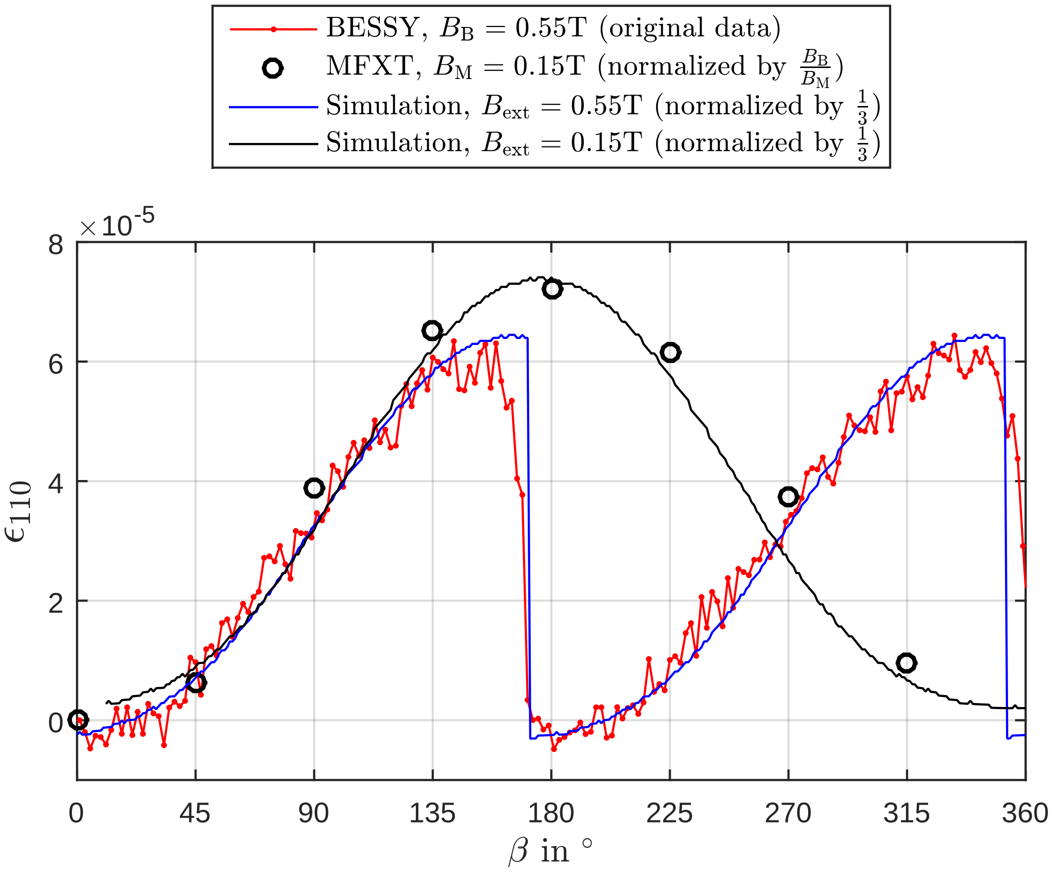

Figure 7.1: Measured and simulated strain in (110) direction of $TbFe_2$ in dependence of the direction of an applied magnetic field. The MFXT data is normalised with the quotient of B_M and B_B improving the visibility of similarities and differences. The simulated strain is normalised by a factor of three for the same reason. The first 150 °, both strains have the same sinusoidal route which the MFXT strain follows further after reaching the maximum at 180 °. The strain measured at BESSY II however shifts to zero at 180 °, repeating this trajectory at larger angles. The simulation shows the same qualitative results but is calculated to be three times higher than measured.

A rotation of the magnetic field over 150 ° to the initial magnetization reveals the different nature of the two measurements. As the strain at the MFXT with the small magnetic field is continuously following a sinusoidal path after reaching its maximum at 180 °, the strain at BESSY II jumps back to zero when the stronger magnetic field is pointing in the opposite direction of the initial magnetization. Afterwards the latter strain follows the same path as it does in the first 150 °, holding a 180 ° symmetry unlike the

360 ° symmetry of the strain measured at the MFXT.

One very simple way to explain that response is to say that the strain is an expression of an internal stress produced by a magnetic field which is not aligned with the magnetization of the sample, which would explain why the strain is always maximal if the external field is antiparallel to the initial magnetization. Furthermore the 360 ° symmetry of the strain at the MFXT is reasonable since 150 mT are not enough to magnetise the sample in another direction, so the sample stays in the initial magnetic state all the time. For BESSY II measurement, the magnetization actually is switched by the applied field of 550 mT. After the switching of the magnetization, the field and magnetization are aligned, so the stress and therefore the strain is zero again.

To substantiate this qualitative discussion I compare in the following sections 7.1 to 7.3 numerous experimental results to numerical calculations based on aspects of magnetostrictive theory discussed in Sec. 5.1 and 5.2. All presented VSM measurements were performed by Arnaud Huillon in the group of Karine Dumesnil at the IJL in Nancy, France. They can give not only a precise magnetic in-plane analysis of the sample but also valuable crystallographic information if compared to other measurements.

The VSM-Hysteresis measurements of **Sec. 7.1** indicate the existence of magnetic domains in $TbFe_2$ as previously reported by Sery et al. [41]. Furthermore, a coercive field of roughly 0.5 T in the $(1\bar{1}0)$ direction was found. This field has to be overcome to actually remagnetise the sample in that direction, and as the measurement at BESSY II was conducted with a slightly higher field, a remagnetisation, or a switch of the magnetization to the opposite side is thus expected.

In **Sec. 7.2**, the magnetization of the sample was measured in a VSM setup while rotating the external field with a strength of 550 mT, basically repeating the measurement conducted at BESSY II, but measuring $\vec{M}$, not ϵ_{110}. In good accord with the BESSY II data, the magnetization exhibits a switch around $\beta = 180\,°$. The interpretation of the experimental result is that the sample is macroscopically magnetised along the $(1\bar{1}0)$ direction at the beginning and for the first 150 to 180 ° and then switches its sign, pointing in the opposite direction of the sample's initial magnetization.

I use the VSM data as an input to the simulation I conducted and documented in **Sec. 7.3**. There, I minimised the total energy of the sample's magnetic system given by energy terms, discussed in Sec. 5.1 in respect to the magnetization's direction for every angle β. Using the calculated minima as input for Akulov's law (Sec. 5.2.2) it was possible to calculate the strain. Doing so, it turned out that although the sample was macroscopically magnetised in $(1\bar{1}0)$ direction, microscopically it is equally divided into domains which are magnetised along two different crystallograpic directions equivalent to a (111) direction (in cubic symmetry). Both directions have a component along $(1\bar{1}0)$ and the perpendicular components compensate each other which is why it can't be macroscopically seen by the VSM measurement in Sec. 7.2. Assuming the state of the sample's magnetization differently would have lead to a different simulation result in terms of the strain which would not match with the measured data at BESSY II as well as the reported existence of magnetic domains. Thinking of only one magnetic domain with one distinct direction of magnetization would have resulted in a rather different simulated strain dependence, see Fig. A.5 in the appendix. This is a contradiction to the measurement as the maximum strain occurs at an angle β, where $\vec{M}$ and $\vec{B}_{\mathrm{ext}}$ are antiparallel, before the magnetization get switched to be aligned again and the strain vanishes (or decreases monotonically in case of the MFXT measurement). Only the sum of two strains of different magnetic domains is consistent with the measurements.

7.1. VSM-Hysteresis Measurements

In this experiment, the sample was put into a Vibrating Sample Magnetometer[11] to gain information of its magnetic response. Thus, hysteresis loops were recorded at different orientations of the external magnetic field with respect to the crystal lattice. The result is displayed in **(a)** of Fig. 7.2. Additionally, the associated in-plane coordinate system is displayed in **(b)** and a sketch of the microscopic magnetic ordering in form of domains similar to Fig. 4.3 is visualized in **(c)** and **(d)**.

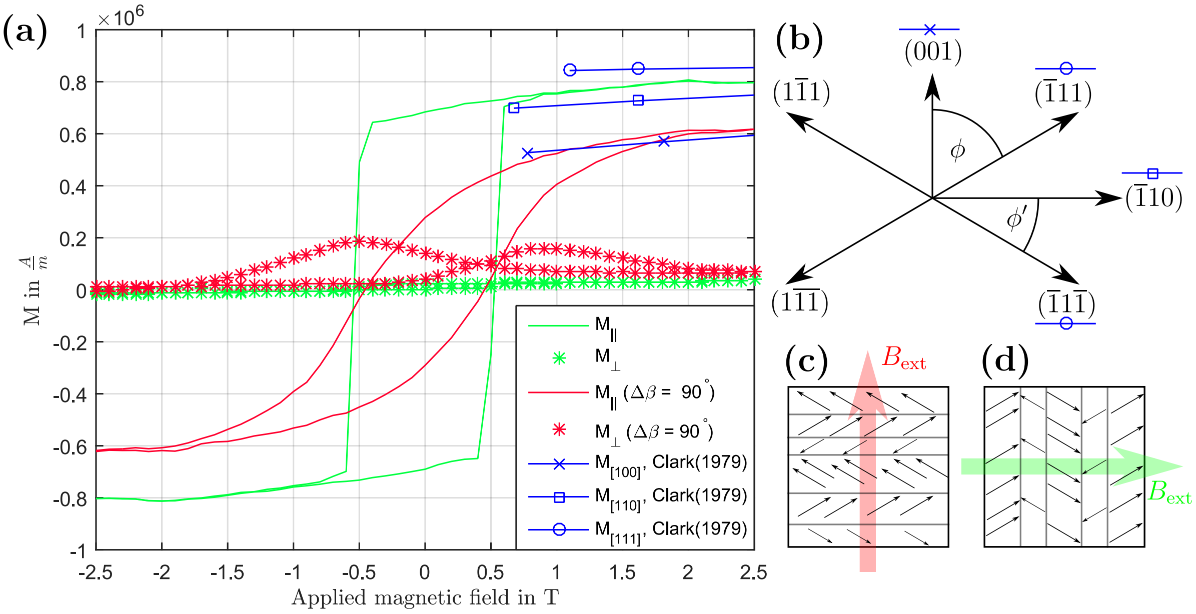

Figure 7.2: **(a)**: Hysteresis loops of $\mathrm{TbFe_2}$ sample via VSM (green and red) and single crystal $\mathrm{TbFe_2}$ magnetization data from Clark (blue) [7]. The plain green graph depicts the magnetization in plane along the direction of the external field and the dotted graph shows the magnetization in plane perpendicular to the field, while the sample's ($\bar{1}10$) direction is aligned with the magnetic field. This situation is visualised in **(d)**, where the external field is pointing along the ($\bar{1}10$) of the coordinate system in **(b)**. The red graph in **(a)** can be assigned similarly, where the external field is rotated by 90 ° so that the (001) direction is aligned with the external magnetic field, outlined in panel **(c)**. Because the hysteresis in **(a)** is not a rectangle in any case, magnetic domains must be present which was already found by Sery et al. [41]. They saw straight parallel domains with walls perpendicular to the aligned field accordingly shown here and in every domain itself the magnetization is aligned to a direction equivalent to (111), the magnetic easy axis [18, 41, 45, 52].

Clark's data and the magnetization in Fig. 4.2 give a spontaneous (or saturation) magnetization of $8.5 \cdot 10^5\,\frac{\mathrm{A}}{\mathrm{m}}$, which is not reached in our VSM measurement. This is in accord with the domain pattern shown in the panels **(c)** and **(d)** of Fig. 7.2. If the external magnetic field is aligned to the ($\bar{1}10$) direction (Fig. 7.2**(d)**), each domain's magnetization projection along that direction is larger and thus the total macroscopic magnetization is larger as if the field is aligned to the (001) direction (Fig. 7.2**(c)**). Looking at the coordinate system in panel **(b)** of Fig. 7.2 this becomes apparent. The angle between the (001) direction and directions equivalent to (111), named ϕ is larger than ϕ', the angle between the ($\bar{1}10$) and (111)-equivalent directions, resulting in different magnetization projections. This is visible in the hysteresis in Fig. 7.2**(a)** as the green graph reaches a larger magnetization as the red graph does. Nevertheless,

---

[11] VSM: A device to measure magnetization of samples inside of homogeneous magnetic fields. Around the sample there are small induction coils (pickup-coils) which can detect small changes in the magnetic flux when the sample is moved. The sample vibrates with known parameters and according to the changing magnetic flux a voltage is induced in the coils. Carefully adjusted and calibrated, one can calculate the magnetization of the sample inside the homogeneous magnetic field along the field direction and perpendicular to it, just by measuring the induced voltage.[81]

the saturation is not reached in both cases, because there are always components of the magnetization of neighbouring domains which cancel each other out, reducing the total amount which is measured. The magnetic field of maximal 2.5 T is therefore not sufficient to erase the small opposing domains and tilt the magnetization in the domains towards the field direction to prevent such compensation mechanism and reach saturation along the field's direction.

Another information we can gather from this hysteresis measurements is a coercive field of 550 mT which is the field at which the net magnetization is zero along the direction of the applied magnetic field. In case of the green graph (where the $(1\bar{1}0)$ direction is parallel to the applied field), this field strength is also basically the same at which the magnetization switches from one plateau to the other with a small change of the external field of roughly 50 mT. This value of the coercive field corresponds well to the observations concerning the strain. While 150 mT is not enough to produce a discontinuously progression in the strain, 550 mT is sufficient. The switch in strain could be associated with the switch in the magnetization at a magnetic field of 550 mT, because the field's projection is only big enough at angles near $\beta = 180\,^{\circ}$, to actually switch the magnetization almost instantaneously, as it happens in this VSM measurement. Thus relieving the sample of the stress originating from an anti-parallelism of magnetization and external field, gives a quick change in strain back to zero as observed at BESSY II.

7.2. Magnetization in field-rotation

With the VSM, A. Hiullion, at the IJL in Nancy, France, was able to record the magnetization under the same conditions under which we conducted experiments at BESSY II and the MFXT. The sample was magnetised with 2.5 T along the $(1\bar{1}0)$ direction and put into an external field of 550 mT, which was rotated by the angle β. The result is depicted in Fig. 7.3. At the beginning, $\mathrm{M}_{||}$ is at maximum, while $\mathrm{M}_{\perp}$ is near zero, because the sample's magnetization is aligned with the external field. Rotating the field does not change the magnetization direction and thus $\mathrm{M}_{||}$ decreases and reaches zero at $90\,^{\circ}$. At the same time, $\mathrm{M}_{\perp}$ increases, because the magnetization's component perpendicular to the external field grows if the magnetization stays in the the same state as before. Furthermore, $\mathrm{M}_{\perp}$ reaches the maximum value of $\mathrm{M}_{||}$ just as the latter changes its sign. The first $150\,^{\circ}$ can be explained just by assuming a rigid magnetization in a certain direction. Associated with a rotating framework, the two components change within the rotation process.

At $150\,^{\circ}$ however, something changes. The magnetization reverses its direction. For a short period of rotation, the net magnetization in-plane reaches almost zero during the switch. $\mathrm{M}_{||}$ reaches its maximum after the switch at roughly $180\,^{\circ}$, because there, the magnetization and the external field are fully aligned again. This process repeats itself after $180\,^{\circ}$, every time the component of the external field parallel to the magnetization is actually strong enough to force a switch, which was already concluded from the strain measurements at BESSY II.

In conclusion, applying and rotating a magnetic field of 550 mT, which equals slightly more than the coercive field of the sample, results in a switch of strain and magnetization when the external field is close to pointing in the opposite direction of the initial macroscopic magnetization of the sample. The magnetization switches because the component of the external field along its direction is strong enough to re-magnetise the sample, so that external field and macroscopic magnetization are aligned again. That explains the rapid loss of strain, because the internal stress associated with it vanishes because of the re-alignment of magnetization and external field. The switch of the macroscopic magnetization must also be interpreted in a multi-domain approach. Initially magnetizing the sample along $(\bar{1}10)$, produces a microstructure shown in panel **(c)** of Fig. 7.2 (green arrow), where almost each domain possesses a magnetization along $(\bar{1}11)$ or $(\bar{1}1\bar{1})$. The sample keeps this state until β reaches $180\,^{\circ}$. There, the domain walls move to enlarge domains with magnetizations along $(1\bar{1}\bar{1})$ or $(1\bar{1}1)$ directions and to decrease the size of the previously dominant domains. As pointed out, the maximum magnetization of $6 \cdot 10^5\,\frac{\mathrm{A}}{\mathrm{m}}$ measured in Fig. 7.2 indicates that not all of the sample is magnetised in the same direction. Lest, the maximum value would have to be around $8.5 \cdot 10^5\,\frac{\mathrm{A}}{\mathrm{m}}$, which equals the saturation magnetization of TbFe_2 at RT. To support my interpretations of the displayed measurements, I simulated the experiment in the following by utilizing the magnetostrictive theory and calculations, illustrated in Sec. 5.2 and 5.1.

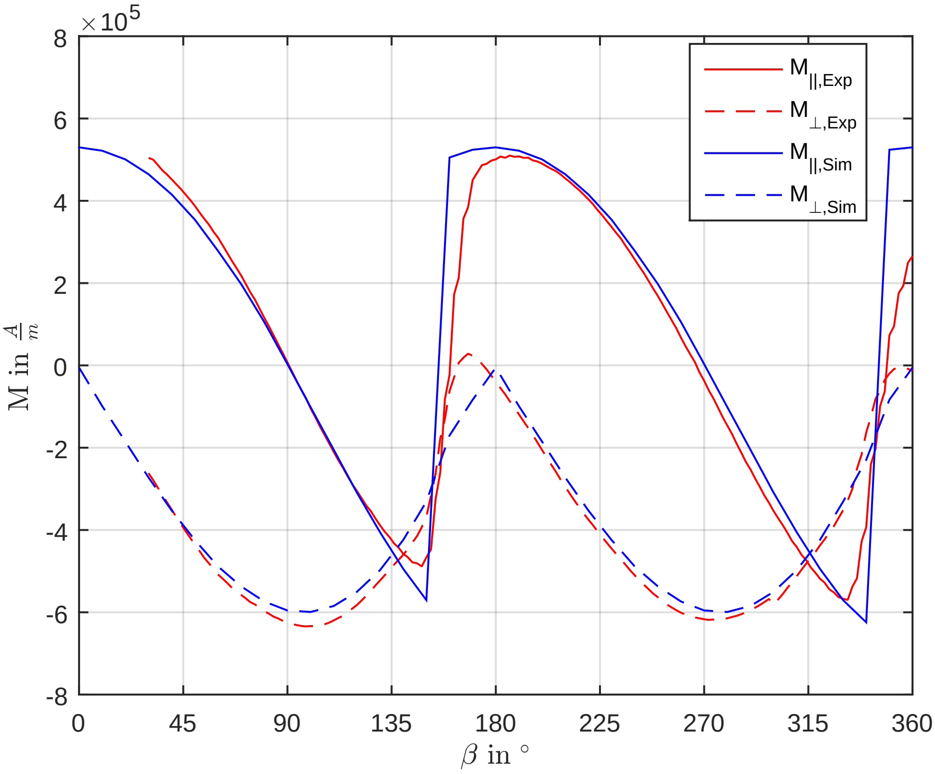

Figure 7.3: VSM measurement: Dependence of magnetization in sample plane perpendicular ($M_\perp$) and parallel ($M_{||}$) to the external field which is rotated by angle β. The progression corresponds to a magnetization which lies in-plane in a certain direction and does not alter its direction or amplitude very much while rotating the external field up to 150 °. While $M_{||}$ decreased monotonically and switches the sign, $M_\perp$ reaches its minimum. Then $M_\perp$ reaches almost zero as $M_{||}$ switches its sign and jumps from the minimum to the maximum in a short period of β. This progression repeats every 180 °. Furthermore, a maximal magnetization value of $5 \cdot 10^5$ to $6 \cdot 10^5\ \frac{\mathrm{A}}{\mathrm{m}}$ was recorded which is an indicator that the sample has microscopical magnetic domains as visualized in the panels **(c)** and **(d)** of Fig. 7.2. Those domains partly compensate each other in terms of magnetization. Otherwise, the maximum of the magnetization should be equal to the spontaneous magnetization of $\mathrm{TbFe_2}$ at RT which is $8.5 \cdot 10^5\ \frac{\mathrm{A}}{\mathrm{m}}$. This measurement supports the existence of domains magnetised along directions equivalent to (111).
The blue lines represent the results of my simulation from the next section. They fit well with the measured data and they contain the assumption of two magnetic domains with different magnetization directions and thus compensating themselves to some extent.

7.3. Simulation of field-rotation

In this section I will use the models and understandings of Sec. 5.2 and 5.1 to simulate the experiment of putting the sample in a rotating magnetic field of 550 mT and observe the magnetization as well as the resulting strain. Together with the measurements of the previous sections, it was possible to visualise and understand the microscopic processes of our sample. A scheme of the simulation's principles is shown in Fig. 7.4.

I took the sum of two energy terms E_A and E_H, the anisotropy energy and Zeeman energy and minimised it, for a constant magnetic field. The idea is that the magnetization, which is parameterised by α_i, has to occupy the state of the lowest energy at any given strength and rotation angle β of the external field.

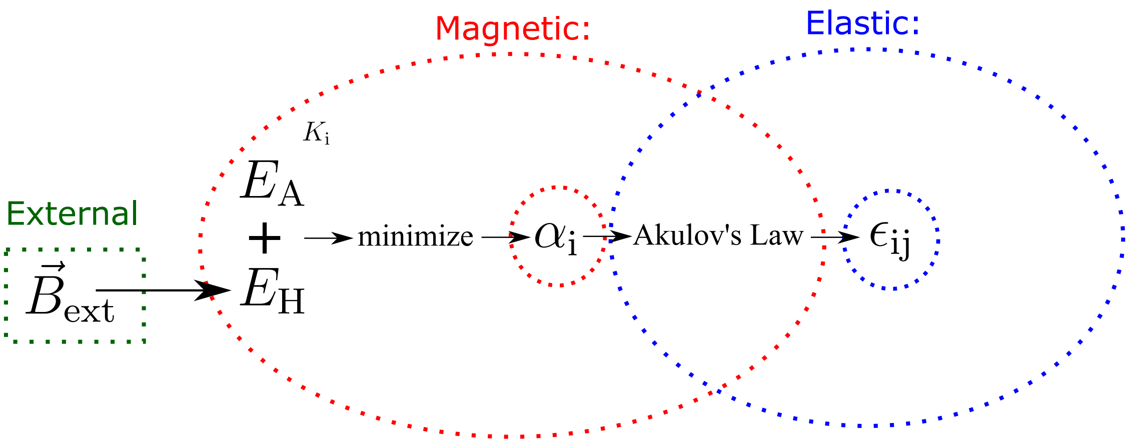

Figure 7.4: Flow chat of the simulation: An external field determines the Zeeman energy E_{H}. The sum of E_{H} and the anisotropy energy E_{A} is minimized to obtain the resulting magnetization direction, parameterised by α_{i}. The α_{i} are used as input for Akulov's law to obtain the strain strain. Therefore then strain and the magnetization state are the results of the simulation.

The outcome of the minimization process is therefore a set of α_{i}, which determine the direction of the magnetization in the sample. This idea was presented by Kovalenko et al. [82]. Due to magnetostriction, the direction of the magnetization has an impact on the lattice, described by the interaction energy E_{ME}, the magnetoelastic coupling energy, see Sec. 5.1.4 and 5.1.5. Akulov's Law (Sec. 5.2.2) gives the strain in any direction for crystallographic cubic materials just by knowing the direction of the magnetization, i.e. handing over the set of α_{i}. Akulov's Law can be seen as a function of the magnetization which maps the strain. Taking the magnetization given by the minimization, the strain can be calculated. Thus, not only the magnetization can be calculated and compared with the data, but also the strain.

To understand the results of the simulation it is first necessary to get used to the chosen nomenclature and to understand relevant definitions . In Fig. 7.5, the outline of an unit cell of TbFe_2 is depicted with crystallgraphic axes, the external field, the magnetization vector and angle parameters used in the simulation.

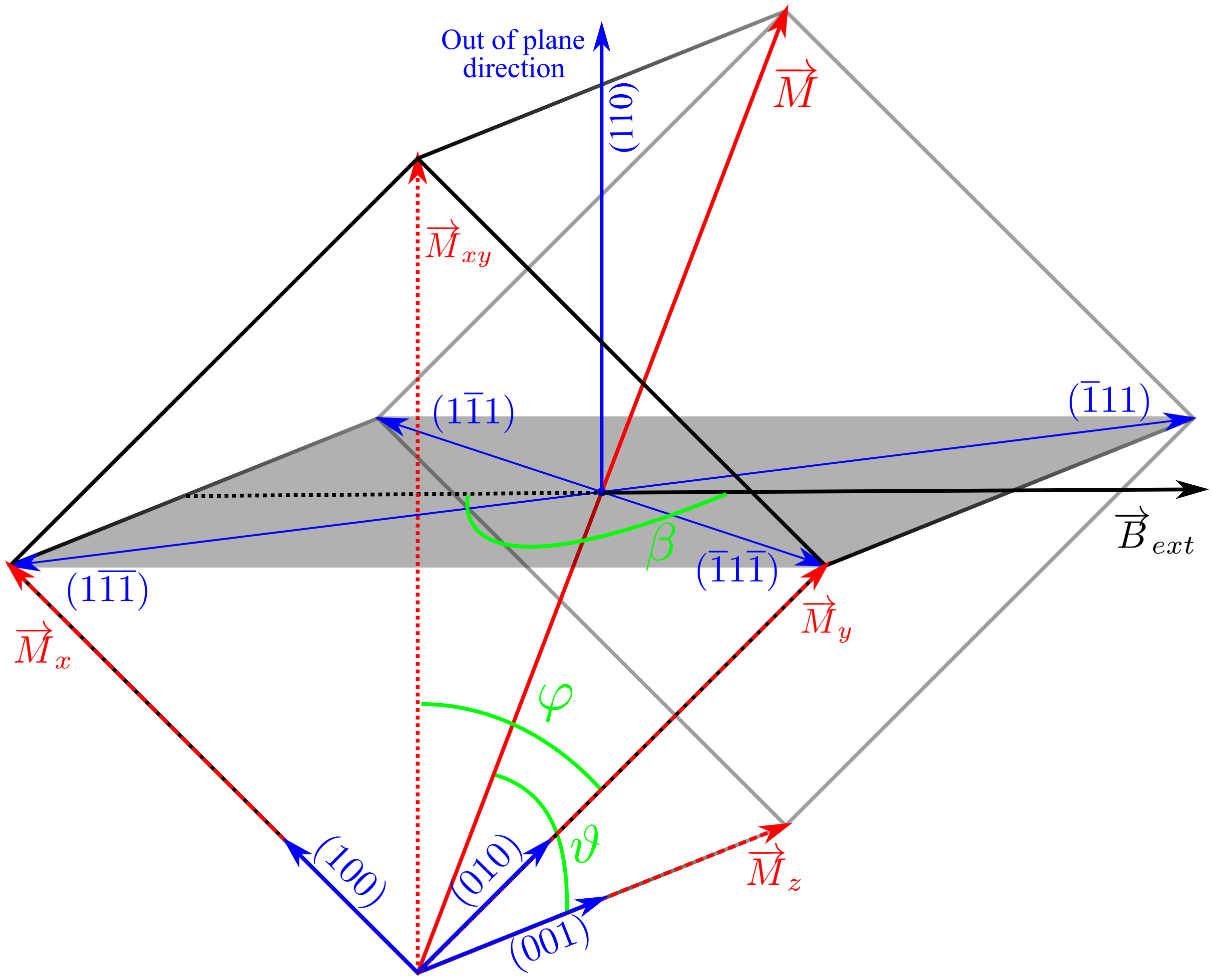

Figure 7.5: Outline of an unit cell of $TbFe_2$ with relevant crystallographic directions (blue), angles (green), the magnetization and its components (red), as well as plane of the sample surface and the external magnetic field, lying in-plane.

Recalling the energy expressions from previous sections (Eq. 5.7 and 5.4) and also taking another energy term into account, the macroscopic shape anisotropy energy E_{shape}, the total energy can be derived, see Eq. 7.1. The shape anisotropy does not originate from an internal, microscopic anisotropy of the material but from the shape of the sample. The favourable direction of the magnetization is parallel to the sample plane (in-plane) for a thin film (500 nm thin, but 0.5 cm in width and length) and a demagnetizing energy can be associated [83] which Kittel mentioned seventy years ago [4]. The direction does not have to coincide with any crystallographic axis or anisotropy. Kovalenko et al. considered this energy term as well in their publication [82]. The total energy is:

$$\begin{aligned} E_{\text{total}} =& E_{\text{A}}(K, \vec{M}) + E_{\text{H}}(\vec{B}_{\text{ext}}, \vec{M}) + E_{\text{shape}}(\vec{M}) \\ =& K_1(\alpha_{\text{x}}^2\alpha_{\text{y}}^2 + \alpha_{\text{y}}^2\alpha_{\text{z}}^2 + \alpha_{\text{z}}^2\alpha_{\text{x}}^2) + K_2(\alpha_{\text{x}}^2\alpha_{\text{y}}^2\alpha_{\text{z}}^2) \\ & - MB_{\text{ext}}\left((-\alpha_{\text{x}} - \alpha_{\text{y}})\frac{\sin(270^\circ - \beta)}{\sqrt{2}} + \alpha_{\text{z}}\cos(270^\circ - \beta)\right) \\ & + \frac{\mu_0 M^2}{2}(\alpha_{\text{x}} + \alpha_{\text{y}})^2, \end{aligned} \tag{7.1}$$

where K are the anisotropy constants, $K_1 = -3.5 \cdot 10^6\,\frac{\text{J}}{\text{m}^3}$ and $K_2 = 7 \cdot 10^5\,\frac{\text{J}}{\text{m}^3}$ (cf. Sec. 5.1.2 and 5.2.4).

The vector $\vec{M}$ is parameterised in terms of α_i, where $\vec{B}_\mathrm{ext}$ only depends on β. The strength of the magnetization was chosen to be $M = 8.5 \cdot 10^5\,\frac{\mathrm{A}}{\mathrm{m}}$ as it is the spontaneous magnetization of $\mathrm{TbFe_2}$ at room temperature, see Fig. 4.2 in Sec. 4.3. Corresponding to the coordinate system in Fig. 7.5, I used the the following notation for the simulation:

$$\vec{M} = \begin{pmatrix} M_\mathrm{x} \\ M_\mathrm{y} \\ M_\mathrm{z} \end{pmatrix} = M \begin{pmatrix} \alpha_\mathrm{x} \\ \alpha_\mathrm{y} \\ \alpha_\mathrm{z} \end{pmatrix} = M \begin{pmatrix} \sin(\vartheta)\sin(\varphi) \\ \sin(\vartheta)\cos(\varphi) \\ \cos(\vartheta) \end{pmatrix} \text{ and } \vec{B}_\mathrm{ext} = \frac{B_\mathrm{ext}}{\sqrt{2}} \begin{pmatrix} -\sin(270^\circ - \beta) \\ \sin(270^\circ - \beta) \\ \sqrt{2}\cos(270^\circ - \beta) \end{pmatrix}. \tag{7.2}$$

Note that the product $-\vec{M} \cdot \vec{B}_\mathrm{ext}$, i.e. E_H, is not just an energy in this case, it describes an energy density, just like E_A, an amount of energy normalised by a volume. This can be understood by recalling that in Sec. 5.1.1, an energy is assigned to one magnetic moment adjusting inside of an external field. But what we need to describe are many of these moments, that are forming a macroscopic magnetization. Thus, $\vec{M}$ and $\vec{B}_\mathrm{ext}$ are given in such manner that their product gives an energy density. For the sake of simplicity I will continue talking about energies rather than about energy densities.

Following Kovalenko et al., I calculate an energy-(density-)map, as a function of two variables; the angles ϑ and φ, for every value of β with fixed M and B_ext. The energy surface E_total for $\beta = 0^\circ$ and $B_\mathrm{ext} = 550\,\mathrm{mT}$ is depicted in Fig. 7.6. It exhibits minima which coincide with the magnetization directions, as the system seeks the least energetic state. In the situation shown in Fig. 7.6, the magnetization most certainly must point to the $(1\bar{1}\bar{1})$ or $(1\bar{1}1)$ direction, because the global and local minima of E_total give those directions. Although the sample was magnetised in $(1\bar{1}0)$ direction before every measurement, where no minimum can be seen in in the energy-density-map ($\vartheta = 90^\circ$ and $\varphi = 135^\circ$), the two mentioned minima represent the state of the magnetization in the domains. Because the minima are symmetrical, I assume equally distributed magnetic domains magnetised either in $(1\bar{1}\bar{1})$ or $(1\bar{1}1)$ direction, which results in a macroscopic magnetization along $(1\bar{1}0)$ and is consistent with our knowledge of the domain structure.

In the appendix, the Figures A.1 to A.4 show the complete energy maps for different angles β at magnetic fields of 550 mT, 150 mT and 1100 mT, as well as one series with neglected shape anisotropy energy at 550 mT. Comparing Fig. A.1 and A.2, the impact of E_shape becomes clear. There are four equal minima at $\beta = 90^\circ$ in the series without it, because the energy is the same for all four directions, even if the magnetization has a component out-of-plane. Considering E_shape however changes this drastically as the magnetization favours now in-plane directions such as $(1\bar{1}1)$ and $(\bar{1}11)$ or $(1\bar{1}\bar{1})$ as in Fig. 7.6. Varying the external field strength has also a very specific effect. Mainly an increase of the field gives rise to the correlation of the field direction with the position and intensity of the minima, i.e. the magnetization direction. Comparing Fig. A.3 with A.1 highlights this manner as only one minimum (or in symmetric cases two minima) distinguishes itself more distinctly if the magnetic field is twice as large. Decreasing the external field leads to an opposite effect. The energy surface stays rather constant with no obvious movements or trajectories of the minima visible, just the intensities of extrema is changing in the course of the rotating magnetic field, see Fig. A.4.

To see how the magnetization direction is changing during the roation of $\vec{B}_\mathrm{ext}$, we must follow the minima during the series of β. On this account, the minima were calculated and plotted as red crosses in Fig. 7.6 to see in which direction the magnetization points. Recalling the magnetization measurements of the previous section 7.2, we already know that the magnetization points into one certain direction and switches to the exact opposite direction after a sufficient rotation of the external field. We also assume that the most magnetic domains are either magnetised in $(1\bar{1}\bar{1})$ or $(1\bar{1}1)$ direction at the beginning. Between 150° and 180° should be the point in β where the magnetization leaves the local energetic minimum around the $(1\bar{1}\bar{1})$ and $(1\bar{1}1)$ direction and switches to the opposite side, the $(\bar{1}11)$ and $(\bar{1}1\bar{1})$ direction. This change of minima is associated with the movement of domain walls as single domains not necessarily change their magnetization direction, but decrease and increase their size to influence their shares on the macroscopic magnetization and re-magnetise the sample along the applied field.

This situation is depicted in Fig. 7.7 where E_total is plotted for $\beta = 150^\circ$ and 180°. The energy

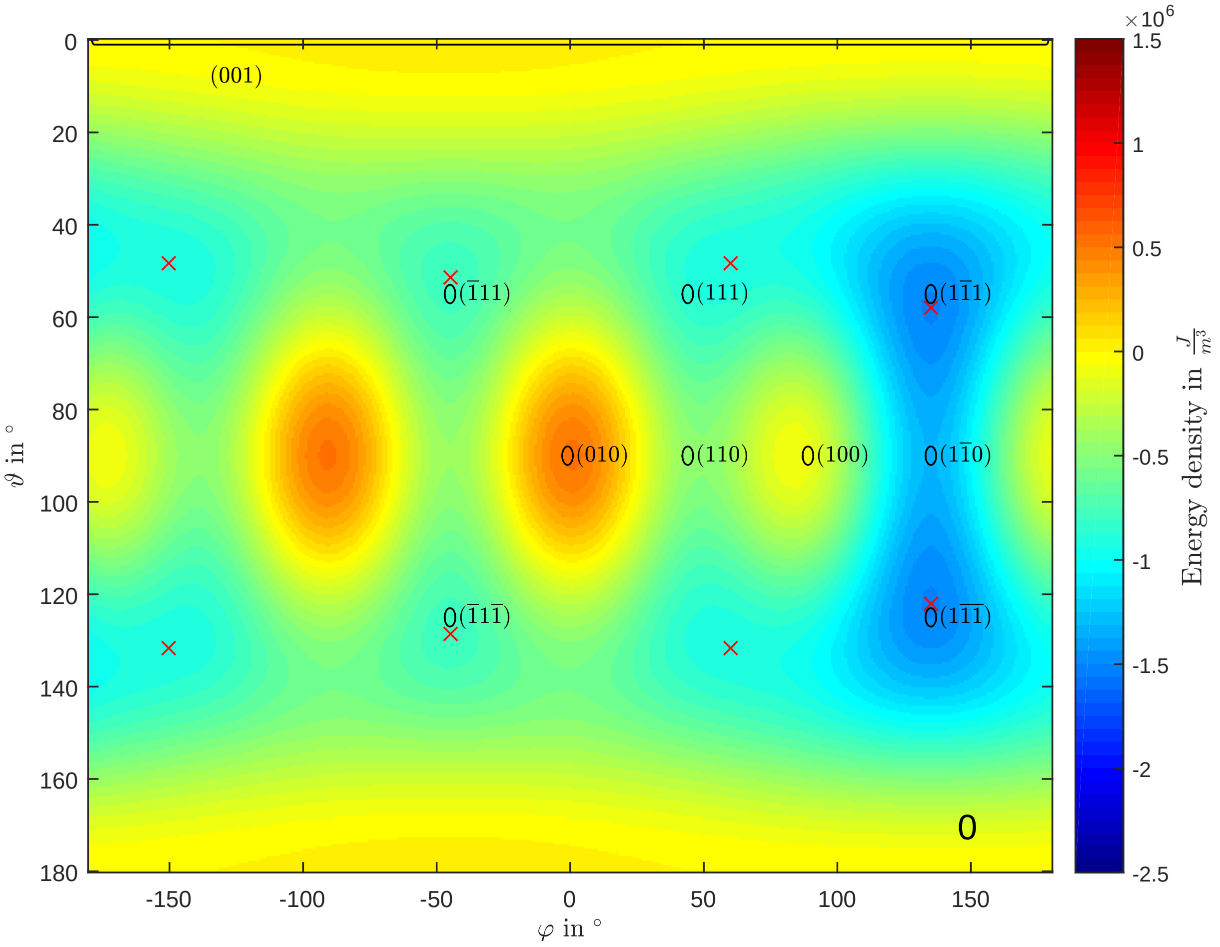

Figure 7.6: Energy density (E_{total}) as a function of the angles ϑ and φ, which parameterise the magnetization, see Fig. 7.5. The ranges of $0\,°$ to $180\,°$ and $-180\,°$ to $180\,°$ of ϑ and φ respectively cover all possible directions of $\vec{M}$. The red crosses are local minima of E_{total} and the zero in the bottom right corner gives the angle β that was chosen to get the depicted simulation result. The small black circles represent certain crystallographic directions with their description next to it, they are depicted for the sake of orientation (the line at the top represents the (001) direction, i.e. $\vartheta = 0\,°$). With $\beta = 0\,°$, $\vec{B}_{\text{ext}}$ is aligned to the $(1\bar{1}0)$ direction, which is associated to $\vartheta = 90\,°$ and $\varphi = 135\,°$. Clearly, the magnetization is pointing in either $(1\bar{1}\bar{1})$ or $(1\bar{1}1)$ direction in the majority of the sample, as the energy's local and global minima are at the those places. This is the initial state of the sample, as it was magnetised with higher fields along the $(1\bar{1}0)$ direction.

maps are equipped with the same features as in Fig. 7.6, additionally rectangles are drawn to mark the most represented magnetization direction distributed over the sample. Before the switch (left), mainly all domains, where $\vec{M}$ points along the $(1\bar{1}\bar{1})$ or $(1\bar{1}1)$ direction occupy most of the specimen's volume. And afterwards (right), the domains with magnetization along the $(\bar{1}11)$ or $(\bar{1}1\bar{1})$ direction are dominant. The map for $\beta = 180\,^\circ$ looks exactly like the one for $0\,^\circ$ as it should be so the states of the magnetization in both cases are indistinguishable originating from the crystallographic symmetry.

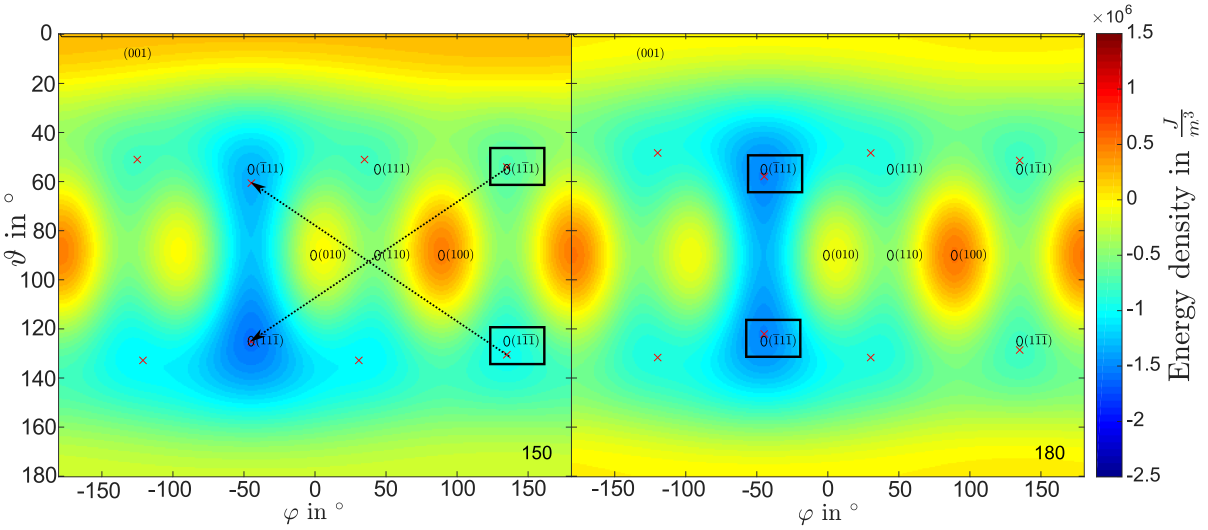

Figure 7.7: Energy maps for $\beta = 150\,^\circ$ and $180\,^\circ$ with all features described already in Fig. 7.6. In the **left** graph, the sample's majority is magnetised along the $(1\bar{1}\bar{1})$ or $(1\bar{1}1)$ direction, although it is not the global minimum but a local minimum is still visible inside the black rectangle. **Right**, at $\beta = 180\,^\circ$, a large portion of the sample is magnetised along $(\bar{1}11)$ or $(\bar{1}1\bar{1})$ direction and thus again occupying the least energetic state in that situation (black rectangle).

By following the energetic minima, it was possible to track the magnetization direction for both cases, i.e. each minimum. Thus it is elementary to simulate the VSM measurements of Sec. 7.2. The minimum contains the pair of φ and ϑ and using Eq. 7.2 to get $\vec{M}$ as well as $\vec{B}_{\mathrm{ext}}$ for every β gives the possibility to calculate the scalar product $\vec{B}_{\mathrm{ext}} \cdot \vec{M}$ which is proportional to $M_\parallel$, and $M_\perp$ is calculated by Pythagoras; $\sqrt{M^2 - M_\parallel^2}$. Including the assumption of two possible states, equally distributed in magnetic domains, the macroscopic magnetization could be calculated. This simulated result of the previous shown measurement is depicted and compared again in Fig. 7.8 (top). A good agreement between the measurement and simulation is visible. The only difference is the steepness during the switching process. While the measurement shows a very steep increase of $M_\parallel$, it is not instantaneous, as it is in the simulation. Some kind of damping process associated with the domain wall movement could be the reason to slow down the switching mechanism in terms of β.

Additionally, the calculated and measured strain is shown in Fig. 7.8 (bottom) again. It was calculated by putting the same set of φ and ϑ for each minimum and β into Akulov's law (Eq. 5.23). It condenses to a very simple form, because the direction of examination $\vec{\gamma}$ is (110), and $\lambda_{111} \gg \lambda_{100}$:

$$\epsilon_{110} = \frac{3\lambda_{110}}{2}\alpha_{\mathrm{x}}\alpha\mathrm{y}. \tag{7.3}$$

Likewise, the strain was calculated for both possible states and the mean value is presented here as the final result. In comparison with the data it is clear that two very important features are represented by the simulation. First, the strain increases monotonically for the most part of the first half of the external field's rotation, and also for the second half, after the switch which is the second feature. A jump in strain occurs around $\beta = 150\,^\circ$, where it decreases drastically to the initial value, associated with the alignment of magnetization and external field. The only difference seems to be the strain amplitude of the simulation which is three times higher than measured. This may originate from the epitaxial clamping of the film or a certain defect pattern.

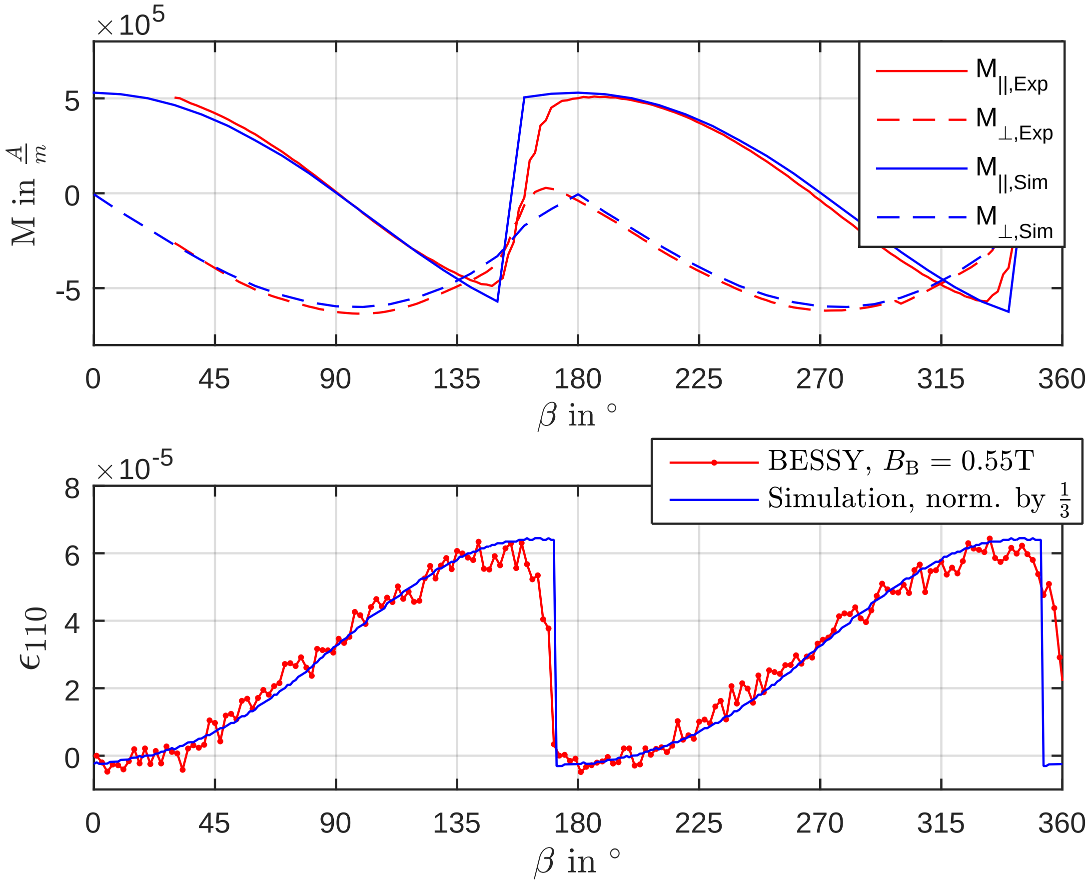

Figure 7.8: Top: VSM-Measurements (see Sec. 7.2) compared to simulated data. The sample's magnetization parallel and perpendicular to the external field over the rotation of the same is depicted. Simulated and measured data are in good agreement. The only deviation lies in the steepness during the switch around $150\,^\circ$.
Bottom: The strain along the (110) direction, calculated and measured at BESSY II, is depicted over the rotation of the external magnetic field of $B_\mathrm{B} = 550\,\mathrm{mT}$. Both, the data and simulation, show a rise in strain when rotating the magnetic field and both show a shift around $150\,^\circ$, where the strain vanishes and starts to rise again. The simulation result is normalised by a factor of $\frac{1}{3}$, to make visible that only the absolute magnitude of the calculated strain must be adjusted to fit the measured data.

Concerning the measurements at the MFXT, the simulation result is the same as one can see in Fig. 7.1. The strain reaches its maximum at $\beta = 180\,^\circ$, before following the mirrored sinusoidal path as in the measurements, reaching zero again at $360\,^\circ$. There are no discontinuities to be found, because the magnetization does not alter its sign, only moving around the $(1\bar{1}\bar{1})$ and $(1\bar{1}1)$ direction, as one can see in Fig. A.4. Also, the strain scales linearly with the quotient of the magnetic field strengths and it is three times higher than the measured one. In Fig. A.5, one can see that a mono-domain approach would not be suitable as the calculated strain would not match with the measurement results.

8. Outlook for static forced magnetostriction

As it was possible for me to describe the microscopic changes within the sample statically with a simple model, the factor of three remains to be explained or justified. To me, it is not clear why the simulation gives a strain which is three times higher than the reality shows us. It may be possible that Akulov's law in its simplicity to which it condenses in my evaluation is not sufficient to cover all magnetoelastic interactions in $TbFe_2$ and therefore the simulation is yet incomplete somehow. However, many sources use this law for the prediction of magnetostriction while knowing the magnetic state of the sample [4, 8, 64]. Since it is reported that a strain occurs in thin films, originating from the mismatch of lattice constants from buffer and film, maybe the sample is clamped in some way, so that the magnetoelastic strain can not be as large as expected [18, 46, 84]. Taking bulk $TbFe_2$ and repeating the measurements would be an option, as clamping effects due to the connections to a substrate are disabled in that case.

At many points during this work, it became clear that magnetic domains are present in $TbFe_2$. More evidence of magnetic domains would be possible to gather with different experimental methods in the future. AFM (Atomic Force Microscopy) measurements have been performed on $TbFe_2$, grown in (111) direction on sapphire by Huth and Flynn [84]. They show magnetic domains in the micrometer-regime and this could easily be performed on the present sample to confirm the existence of domains. A spatial overview of the sample's magnetic structure can be also achieved with MOKE (Magneto-optical Kerr Effect [85]). The UDKM group is currently working on such experimental implementation. But also simple XRD is capable of detecting magnetic domains, even if the X-ray probe spot on the sample is larger than the domains. If so, the Bragg-Peak must be of increased width because of varieties in the lattice constant from domain to domain.

To test Akulov's law, different crystallographic axes could be examined in terms of magnetostriction as well. The BESSY II setup is suited for such measurements. However, on $TbFe_2$ conducted measurements were not consistent regarding the intensity and position of the Bragg-peaks. Responsible was a wrong association of the crystallographic axes in the sample while measuring asymmetrical Bragg reflections. Repeating these experiments with a better understanding of how the crystallographic system is oriented in the sample could improve the amount of data we have to test the presented modelling I developed.

We also conducted magnetic switching under laser irradiation and a selection of the results is depicted in Fig. A.6 of the appendix. It utilises the same experimental setup as described in Sec. 6.2 but with an additional laser system in place which is usually used for time resolved measurements, see Sec. 9.1. The laser heats the sample with short pulses and adjustable fluences and could evoke an earlier switching in terms of β during the rotation of the external field. So far we have not yet developed a consistent interpretation but it seems to be a promising topic because this could give quantitative information about energy-density thresholds which need to be overcome to switch the sample magnetization.

Part III.

Ultrafast lattice dynamics of $TbFe_2$

As the UDKM group has a strong interest in dynamics of nanostructures on a femto- to nanosecond time scale, I used two experimental setups to observe the lattice dynamics of $TbFe_2$ after the excitation by an ultrashort laser pulse. One of the setups is the previously presented XPP-KMC-3-Beamline at BESSY II. A pulsed laser system is additionally used to trigger dynamics which are detected via time resolved XRD, in a pump-probe approach. The second setup, the Plasma X-ray source, is an ultrafast time-resolved version of the MFXT setup. Additionally I utilised the UDKM1DSIM-toolbox to simulate the pump-probe experiments and interpret the observed lattice dynamics.

This part begins with a description of the PXS and BESSY II setups in Sec. 9 where I explain the implementation of the pump-probe experiments to provide an overview of the capabilities, limits and collected data of the setups. In the subsequent section 10 I discuss the collected data, i.e. the lattice strain obtained via time-resolved XRD by fitting the Bragg reflections with Gaussian profiles or calculating the COM. It follows an analysis of the PXS data focussed on the strain dynamics during the first 150 ps deduced from a detailed examination of the temporal evolution of recorded Bragg peaks. I further discuss the BESSY II data with respect to the magnetic and thermal strain present in the sample. I conclude this part with a data interpretation by modelling the results using the UDKM1DSIM-toolbox in Sec. 11.

9. Experimental setup and data acquisition

Two complementary setups were used in this work to measure the temporal dynamics: the lab based Plasma X-ray Source of the UDKM group and the BESSY II beamline already described in Sec. 6.2. The time resolution is better at the PXS, however longer delays can be measured at the BESSY II beamline with higher resolution in $\vec{Q}$ space. In both, timeresolved XRD is performed on $TbFe_2$. After exciting the sample with an ultrashort, high fluence laser pump pulse it is probed with short X-ray pulses. The laser pulse deposits a large amount of energy inside the sample in times less than a picosecond, which results among other things in a dynamical, spatio-temporal lattice distortion which can be examined by an ultrashort X-ray pulse. A brief overview of the two setups is given in table 9.1, comparing the setup specifications. The experiments are discussed in more detail in the following sections together with an explanation of the data handling routine.

Table 9.1: Comparison of MFXT and BESSY II setup parameters

	Plasma X-ray Source[86, 87, 88]	BESSY II-Beamline [73, 76]
X-ray source	focused laser pulse (40 fs, 800 nm centre wavelength, 6 mJ pulse energy) on a 15 μm thick Cu-Tape	dipole D13.1 magnet at the electron storage ring BESSY II
X-ray optics	Montel multilayer optic [89] with 0.3 ° divergence, focusing to $(300\,\mu\text{m})^2$ with a flux of approximately $5 \cdot 10^5\ \frac{\text{photons}}{\text{s}}$	*XPP-KMC3-Beamline*: parabolic mirrors and a double crystal monochromator, creating a $(350\,\mu\text{m})^2$ focus with a flux of approximately $10^{11}\ \frac{\text{photons}}{\text{s}}$
X-ray energy	8.048 keV to 8.027 keV (Cu-K_{α_1} and K_{α_2})	10 keV (Synchrotron)
Goniometer geometry	two circle diffractometer (ω,θ)	four circle diffractometer (ω,θ,ϕ,χ)
Detector System	*Pilatus 100k* (Dectris) fast read-out two-dimensional X-ray detector, 172 μm pixel size	*Pilatus 100k* (Dectris) fast read-out two-dimensional X-ray detector, 172 μm pixel size
Accessable delay	0 to 4 ns	0 to 4.8 μs
Time resolution	250 fs	50 ps
Pump-Laser system	*Mantis* (Coherent) oscillator producing short pulses, amplified by *Legend Duo* (Coherent) Two-stage Ti:sapphire amplifier	*Clark-MXR*, Impulse: multi-stage Yb-doped fibre-amplifier
Centre wavelength	800 nm	1030 nm
Pump-pulse duration	40 fs	250 fs
Pump-pulse energy	0.1 mJ	10 μJ
Repetition rate	1 kHz	200 kHz to 1.25 MHz

9.1. BESSY II Beamline

The setup is the same as it is described in Sec. 6.2 extended by a synchronized pump-laser. A multi-stage fibre-amplifier amplifies femtosecond laser pulses which are synchronised with the synchrotron's periodically emitted X-ray pulses with a repetition rate of 1.25 MHz. The synchronization accuracy is 4 ps at maximum and the X-ray pulse length of 50 ps limits the time resolution of this setup. By coupling the pump beam into the centre of the goniometer, the sample is exposed to 250 fs pump pulses with a centre wavelength of 1030 nm which deposit approximately 10 μJ of energy [76]. The fluence (the amount of energy deposited per time and area) can be varied by adjusting the pump laser's intensity to achieve different amounts of excitation[12]. A sketch of the pump probe implementation is shown in Fig. 9.1.

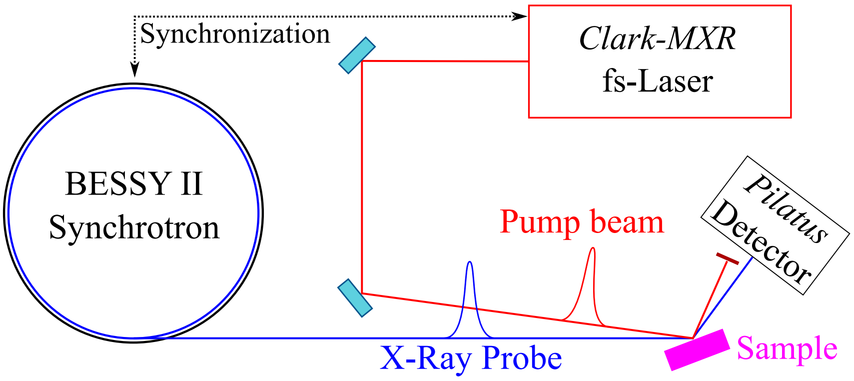

Figure 9.1: Layout of the pump probe setup at BESSY II. In addition to the X-ray setup (blue, described in Sec. 6.2), a femtosecond laser is installed at the beamline to supply ultrashort light pulses as excitation pump-pulses which are electrically synchronised with the periodically occurring X-ray probe pulses. The delay between pump and probe can be chosen freely up to 5 μs determined by the round trip time of an electron bunch in the storage ring. Doing so, the evolution of the diffracted X-ray signal in time is recorded by running through several pump probe iterations with various delays.

Because an area detector is used, it does not have to be moved to scan the reciprocal space for different delays, only the sample is rotated during the scans. The chosen Bragg peak is centred on the detector before each pump probe experiment. The observed peak shifts and distortions are small, the reflection will never leave the detector area in course of a delay scan. Thus, the lattice spacing corresponding to the position of the Bragg peak can be measured as a function of the time after the pump laser excites the sample, proceeding accordingly to Sec. 6.2. This means, RSM are constructed from the detector images, the maxima in $\vec{Q}$-space are determined and associated with the (110) lattice spacing which changes during a delay series. The final result is the relative change in spacing, the strain, which is depicted in Fig. 10.4 of Sec. 10.3.

9.2. Plasma X-ray Source

The Plasma X-ray Source is one of the main experimental stations of the UDKM group. It allows time resolved X-ray diffraction in a pump-probe experiment and sub-picosecond resolution in a tabletop setup. Due to its complexity, I refer to several publications that summarise the main working principles of this machine, primarily the dissertation of D. Schick [90] as well as the Master thesis of A. von Reppert [6] and J. Pudell [5]. There one finds more detailed views of the setup and many examples of measurements already conducted using this source.

The process of generating ultrashort X-ray pulses is the heart of the PXS, also giving it its name. Accelerated electrons are the source of X-rays but the acceleration is accomplished with a short and

---

[12] The fluence is calcualted via the Top Hat approximation of the pump pulse spatial profile (at BESSY II as well as PXS). Therefore, the energy per pulse E_p is calculated by the repetition rate and the output power. Also, the two dimensional Gaussian beam profile is recorded to obtain the full width at half maximum (FWHM) in x- and y-direction perpendicular to the propagation direction. The fluence is then derived by $2E_\mathrm{p}/(\pi \mathrm{FWHM_x FWHM_y})$, i.e. the ratio of pulse energy and the approximated area which resembles a top hat as an approximation of the two dimensional Gaussian beam profile.

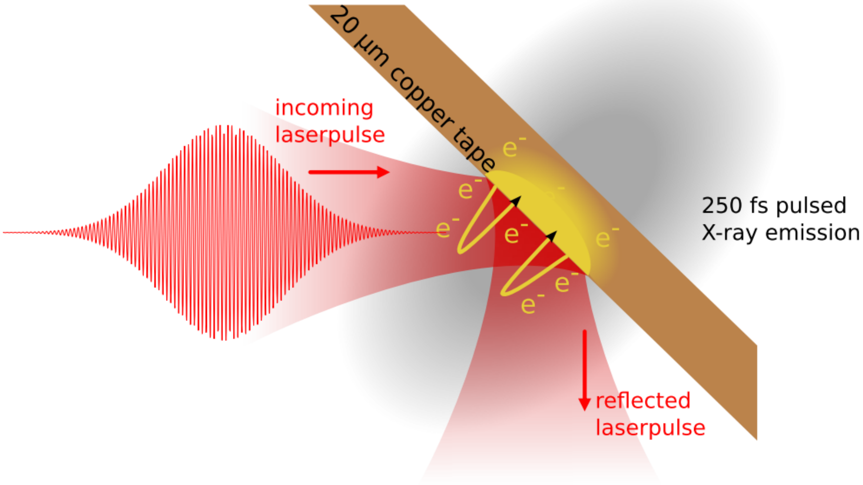

Figure 9.2: Sketch of the generation precess for short X-ray pulses, taken from von Reppert [6] who adapted this sketch from Weisshaupt et al. [91]. An incoming ultrashort laserpulse ionises copper atoms at the tape surface. This is possible because an energy of 6 mJ is compressed to a light pulse of 40 fs length, resulting in a peak intensity of $5 \cdot 10^{17}\,\frac{\mathrm{W}}{\mathrm{cm}^2}$ [90]. This is associated with an electric field of over $10^{12}\,\frac{\mathrm{V}}{\mathrm{m}}$ which creates the plasma due to ionization in the copper tape (yellow area). Electrons inside this large oscillating electric field are accelerated and decelerated for a short period of time and also interacting with the surrounding copper as they do in conventional X-ray tubes. The resulting X-ray spectrum is therefore similar to the one shown in Sec. 6.1.1, containing Bremsstrahlung as well as the characteristic spectral lines of copper. X-rays are only emitted while the laserpulse is present and shortly after, resulting in 250 fs x-ray probe pulses with a repetition rate of 1 kHz. The X-ray pulse length is the limiting factor of the time resolution, which is almost two orders of magnitudes higher as at BESSY II [6]. After the emission of an X-ray pulse, a small hole is left in the tape and therefore the tape is translated continuously to ensure the same initial situation for every pulse every millisecond.

very intense laserpulse, not with a booster synchrotron or a static electric field. In Fig. 9.2, the X-ray generation process at the PXS is depicted and explained.

The plasma used for X-ray generation is located in an interaction chamber of the experimental station for which an overview is shown in Fig. 9.3 to understand the functioning of the setup. Having a two circle goniometer combined with a pulsed laser system which illuminates the sample for 40 fs and simultaneously generates short X-ray pulses to diffract from the excited sample, time resolved X-ray diffraction is realised. The pump probe delay is set via a mechanical delay stage.

Similar to the procedure at BESSY II (Sec. 6.2), the area detector allows us to create a RSM where maxima in $\vec{Q}$-Space are associated with sets of planes in this case again, along the (110)-direction, out-of-plane. However, in the course of this thesis the goniometer geometry was fixed during the delay scans. Because the X-rays which are focussed onto the sample have a convergence of 0.3 ° and an area detector is in place, a miniature version of a $\vartheta/2\vartheta$-Scan is conducted without moving the goniometer. During one exposure, a range of diffraction angles is thus detected simultaneously. If the chosen incident angle is the Bragg angle of the (110) peak of $\mathrm{TbFe_2}$, additional X-rays will shine onto the sample under a slightly different angle, i.e. ±0.15 °. An area detector is therefore very useful as it records all the diffracted X-rays simultaneously in contrast to a point detector which can only detect X-rays under one specific diffraction angle. The detector picture is integrated along the direction perpendicular to the diffraction plane after each exposure to get a one dimensional intensity profile in q_z direction.

Shifts and distortions of these reflections correspond to lattice dynamics which can be examined over time as shwon in pump-probe experiments. For every delay, the measured Bragg peak is evaluated mostly with respect to the momentary strain within the region probed by X-ray pulses. The probe region is located in the centre of the pump area which is larger than the X-ray spot. A Gaussian fit and the COM is used to determine the exact position of the peak maximum associated with the average lattice spacing, giving the strain. The time dependence of the latter and also of the peak's shape is measured at $TbFe_2$ for different fluences. The results are discussed together with the measurements at BESSY II in the following Sec. 10.

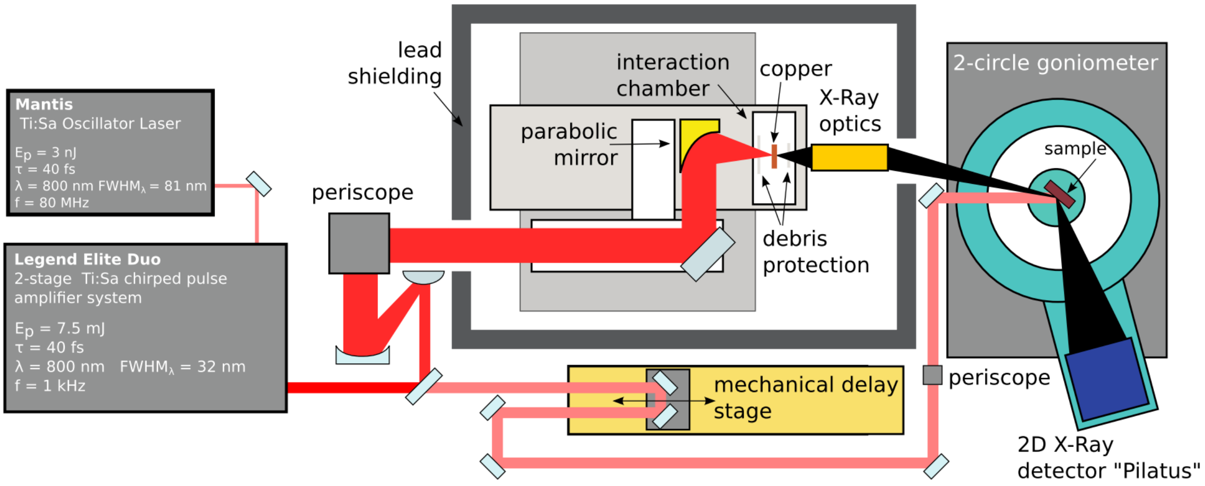

Figure 9.3: Sketch of the PXS, taken from von Reppert[6], cf. [90] and [5]. A *Mantis* Ti:sapphire oscillator creates fs low energy pulses with 80 MHz repetition rate which are coupled into the *Legend Elite Duo* amplifier. The amplifier's output is a pulsed laser signal with a 1 kHz repetition rate, 800 nm centre wavelength, 40 fs pulse length, but 7.5 mJ energy per pulse. By passing a beamsplitter, 80% of the *Legend Elite Duo* output is focused inside the interaction chamber using a parabolic mirror onto the copper tape, creating X-ray pulses which are focussed on the sample located in the centre of a two circle goniometer. The remaining 20% of the amplifier output are available for sample excitation passing through the mechanical delay stage.

10. Experimental results

In this section I present time resolved X-ray diffraction data on $TbFe_2$ collected at the PXS setup and at BESSY II. The lattice dynamics on a pico- to nanosecond time scale after photo excitation are determined via X-ray diffraction. Therefore, the recorded RSMs were integrated along q_x to provide one dimensional diffraction patterns. The diffracted intensity as a function of q_z, i.e. one dimensional Bragg peaks are evaluated at different time delays.

10.1. Evaluation of Bragg peaks

In Fig. 10.1a, the (220) Bragg peaks of $TbFe_2$ are depicted, selected at four different delay times at the PXS. They are fitted with Gaussian profiles as shown, to determine the corresponding q_z which is associated with a certain lattice spacing via Bragg's law. In Fig. 10.1b, two Bragg peaks are plotted to emphasise that at early delays (< 100 ps), the peaks are asymmetrical as they exhibit shoulders which are not covered by single Gaussian fits.

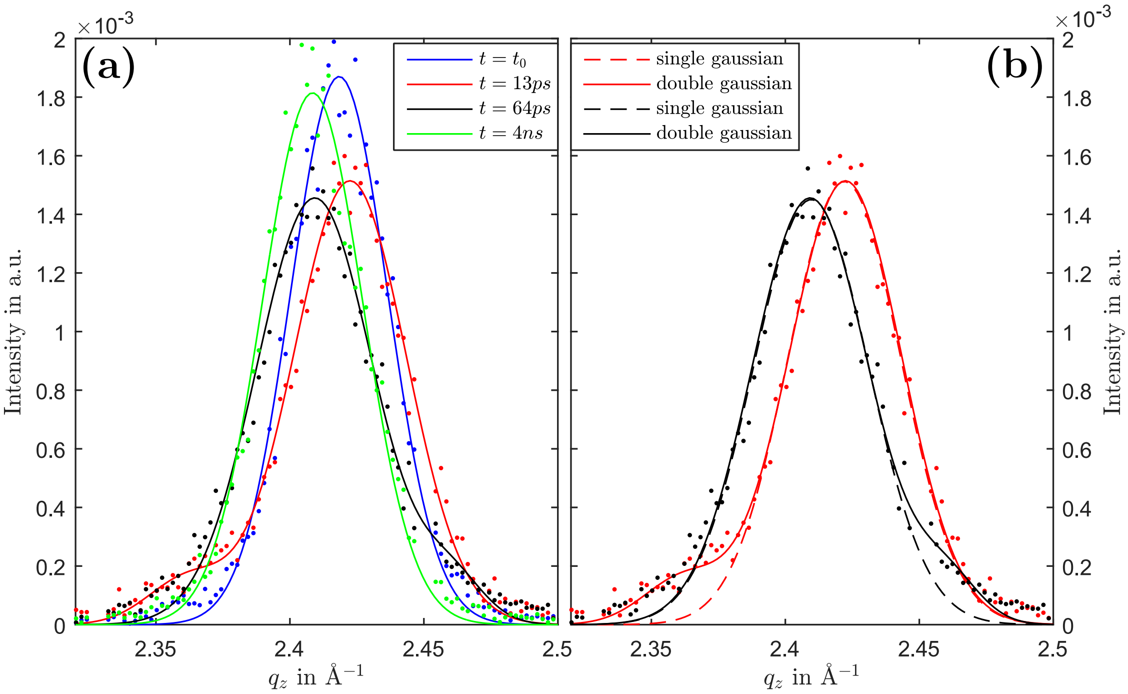

Figure 10.1: (a): Measured Bragg peaks at PXS with a fluence of 25 $\frac{\text{mJ}}{\text{cm}^2}$ at four different delays displayed with Gaussian fits for q_z determination. Data and fits are displayed at $t = t_0$, 13 ps, 64 ps and 4 ns. **(b)**: Data points, double Gaussian and regular Gaussian fits are displayed at $t = 13$ ps and 64 ps.

In Fig. 10.1a, the temporal evolution of the Bragg peaks becomes visible. 13 ps after excitation, the intensity has decreased by 20% associated with a disorder of the $TbFe_2$ lattice. Also, the main peak shifted by $-1.5 \cdot 10^{-3}$ to higher q_z associated with a compressed majority of the layer. Simultaneously a shoulder at lower q_z has developed, associated with a small fraction of the sample being expanded. These are the initially excited and now expanded top layers. At 64 ps, the main Bragg peak's intensity has subsequently further decreased by 4% and it shifted by $3.5 \cdot 10^{-3}$ to lower q_z in relation to the initial position. At this stage, it exhibits a shoulder at higher q_z associated with a small fraction of the sample yet being compressed. But still a small shoulder at lower q_z is visible. The Bragg peak then recovers intensity while the shoulders are vanishing until it reaches 97% of the initial intensity 4 ns after excitation. At this point in time, it is shifted by $3.5 \cdot 10^{-3}$ to lower q_z.

For the two time delays, where the shoulders of the Bragg peak are pronounced, at $t = 13\,\text{ps}$ and 64 ps, data and fits are depicted again in Fig. 10.1b. There, the peaks are fitted with a single Gaussian function (dashed line) and a double Gaussian profile, i.e. the sum of two Gaussian functions. While the double Gaussian fit covers the whole range of data points, the single Gaussian fit mainly matches the data points in the centre of the major Bragg peak, disregarding the shoulders. The position of the main Bragg peak however differs by less than 1% in both approaches which is why both are valid.

Regardless of the Gaussian evaluation method, these shoulders can be interpreted as minor parts of the sample diffracting under a different $\vec{Q}$ because they are compressed (shoulder at higher q_z) or expanded (shoulder at lower q_z) in relation to the majority of the sample (main Bragg peak). Thus, I additionally calculate the COM of the peaks. This way, the shoulders will be included in the determination of q_z. These two evaluation methods provide two different pieces of information about the sample. As the COM is sensitive to the main peak but also takes shoulders into account, the q_z is different from the q_z one gets from the Gaussian fit which includes only the main peak. This means that the COM asserts the average lattice spacing in $TbFe_2$ while the Gaussian fit provides the lattice spacing inside the fraction of the layer with the highest diffraction signal which is usually the majority of the sample.

The Bragg peaks recorded at BESSY II are measured with a significantly slower time resolution which is why the shoulders and temporal evolution during the first 100 ps could not be observed. However, the q_z and the resulting strain determined either via COM or Gaussian fits differ from each other as well, as one can see in section 10.3.

10.2. Picosecond strain dynamics at the PXS

The temporal evolution of the lattice spacing is determined by evaluating the Bragg peaks for every time delay. I then calculate the relative change of the lattice spacing, i.e. the strain. In this thesis I only evaluate (220) or (440) Bragg peaks which is why the strain along the (110) direction (ϵ_{110}) is determined via q_z from the COM and Gaussian fits. In the used sample geometry, this direction is perpendicular to the sample surface.

In Fig. 10.3, ϵ_{110} is plotted for seven fluences. In the top graph ϵ_{110} was determined via a Gaussian fit of the Bragg peak and in the bottom grpah ϵ_{110} was calculated via the COM. Obviously, the determination method of the peak position is of high relevance when quantifying the strain with a high time resolution. Applying the conclusions of Sec. 10.1, the PXS data show an immediate increase of the average strain after excitation (COM). The strain is reaching its maximum between 10 ps and 60 ps depending on the fluence. With increasing fluence, a larger maximum is recorded and the maximum is recorded at larger delay times. This is due to heat deposited inside $TbFe_2$ by photo excitation which is accompanied with a thermal expansion proportional to the initial amount of energy deposited. The exceptional case is the strain evolution for a high fluence of $25\,\frac{\text{mJ}}{\text{cm}^2}$ because not until 10 ps after excitation the strain begins to rise and seems to continue increasing at 1 ns.

The strain provided by the Gaussian fit implies that the majority of $TbFe_2$ is compressed during the first 10 ps to 30 ps after t_0, depending on the fluence. Subsequently the strain rises to a local maximum, meaning that most of the sample is expanded before a renewed decrease results in a local minimum at 110 ps. Afterwards, the global maximum is reached which shifts to larger delay times with increasing fluence.

The dynamics during the first 100 ps are in accord with previous ultra fast time resolved XRD measurements and is explained in depth in the publication by D. Schick et al. [92]. With Fig. 10.2 I shortly summarize their findings. With that in mind, the ultra fast strain dynamics measured at the PXS can be explained qualitatively. A few picoseconds after photo excitation, just the top layer is strongly expanded, whereas the majority of the sample is slightly compressed. This is in accord with the Bragg peak shift and the shoulder we see at 13 ps in Fig. 10.1a. During the propagation of the strain-wave through the layer, the amount of compressed $TbFe_2$ decreases as two parts of the layer are expanded (H

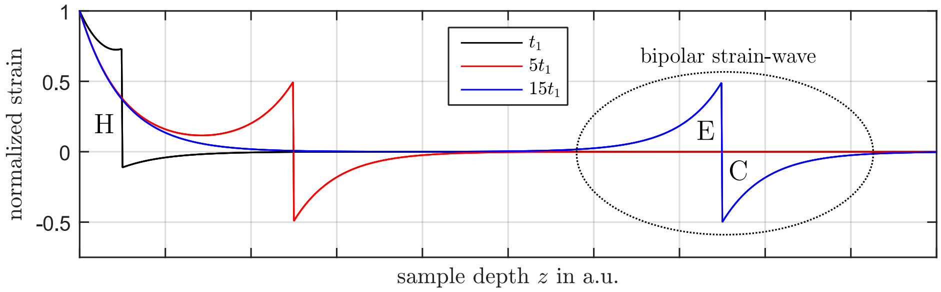

Figure 10.2: Sketched strain profiles at three arbitrary delay times inside a layer excited by an femtosecond laser pulse, adapted from Schick et al. [92]. The initial pump pulse inscribes an inhomogeneous stress profile according to Beer-Lambert's law. A few picoseconds after excitation (t_1) the top layers give in to the stress and expand, i.e. show a positive strain. This is because the amount of deposited energy is maximal near the surface and so is the stress the lattice is exposed to. Going deeper into the sample, the stress decreases exponentially, resulting in a net contraction of the majority of the sample during the first 10 ps to 30 ps. The expansion (E) propagates with sound velocity into the $TbFe_2$ layer, preceded by the contraction (C). This spatial strain transforms into a bipolar strain-wave propagating through the layer ($15t_1$), leaving an exponentially decreasing strain profile due to heat at the surface (H) behind.

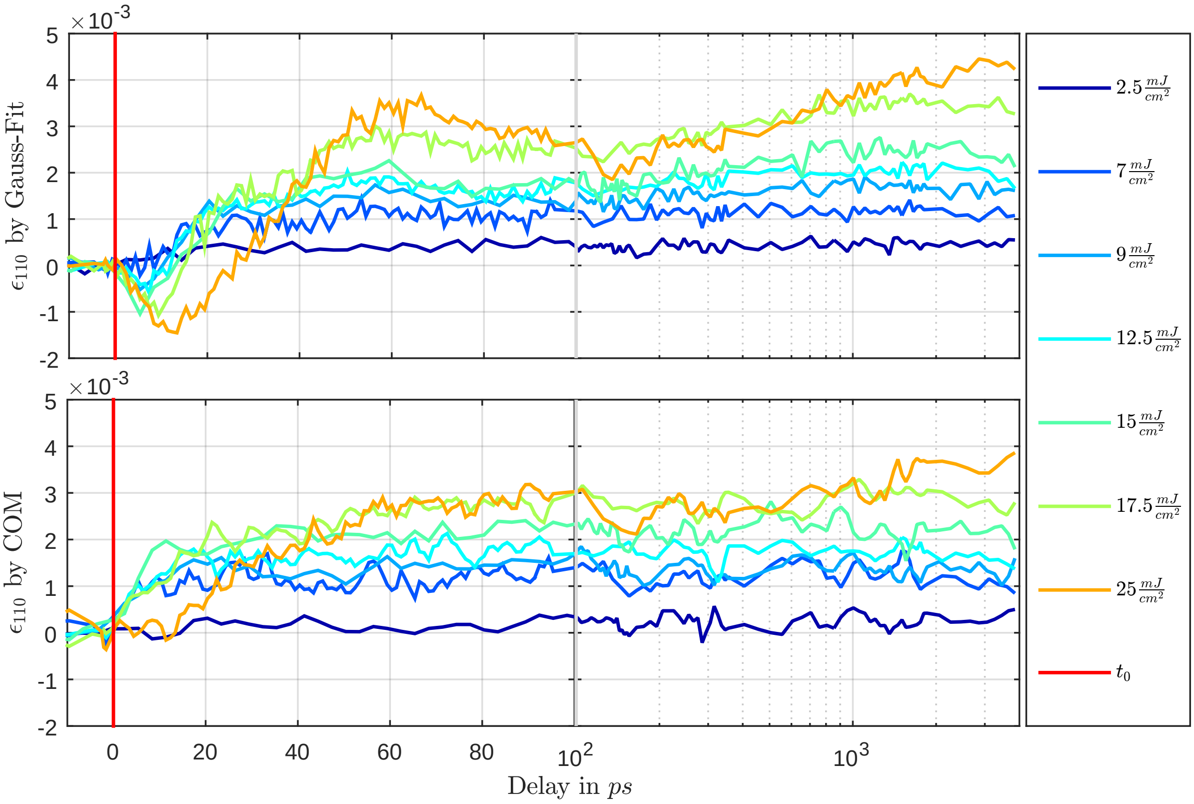

Figure 10.3: Fluence series of temporal strain evolution in $TbFe_2$ after laser excitation at t_0, measured at the PXS. For each fluence, the Bragg peak of $TbFe_2$ was scanned for delays reaching up to 4 ns. Either the COM (**bottom**) was determined or a Gaussian fit (**top**) was utilised to ascertain the peak position in q_z and associate a lattice spacing which leads to the strain when compared to the initial value at $t < t_0$. The COM data are smoothed to ensure a better visibility, meaning that every data point represents the average value over adjacent data points and itself.

and E in Fig. 10.2). The expanded parts are associated with the Bragg peak shift to lower q_z and the small shoulder at lower q_z. The preceding compressive part corresponds to the shoulder at larger q_z of the peak at 64 ps in Fig. 10.1a. At this delay time, the compressive part of the strain wave starts to propagate into the adjacent niobium layer which is why the average strain increases until 110 ps. Then, a sudden strain decrease is recorded as the expansive part of the strain-wave follows the compressive part into the niobium.

10.3. Nanosecond strain dynamics at BESSY II

An overview of the strain evolution of TbFe$_2$ after laser excitation has been determined at BESSY II from 0 to 500 ns, with a magnetic field applied in different directions, see Fig. 10.4. A similar measurement series is displayed in the appendix in Fig. A.7 which differs in terms of the point density which is five times higher at short time delay.

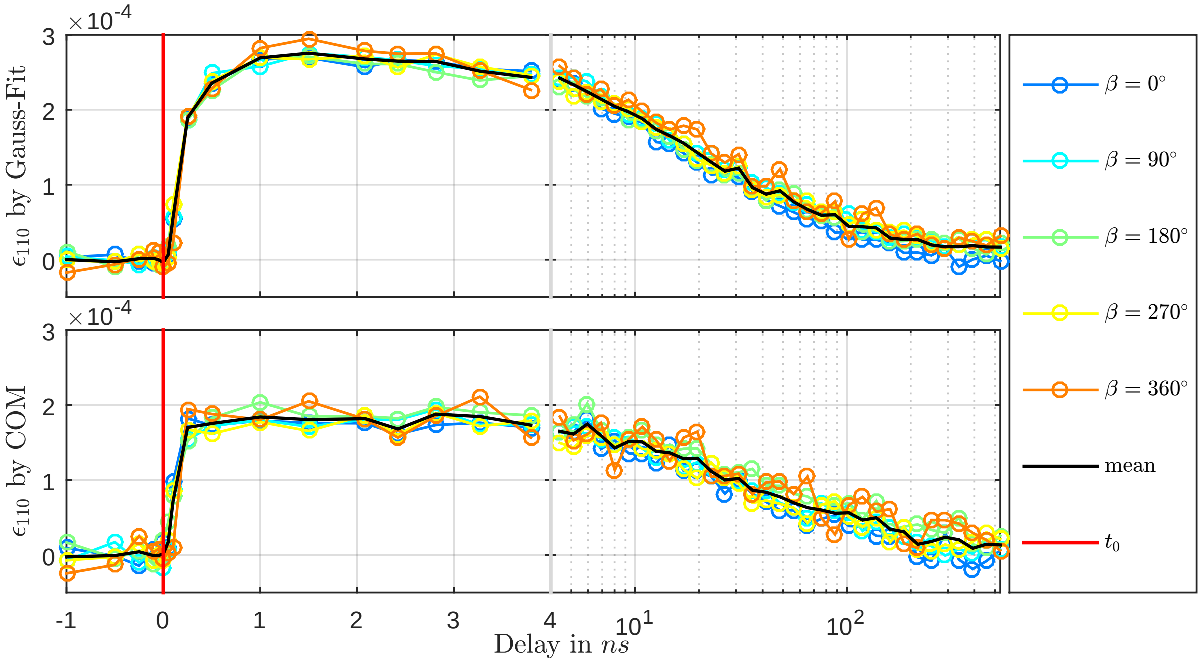

Figure 10.4: Time resolved strain of TbFe$_2$ after laser excitation at t_0 along (110) direction. The strain is either calculated by a Gaussian fit (**top**) by the COM method (**bottom**) and is derived for five different directions (β) of an external magnetic field with a strength of 550 mT. The sample was exposed to 7.5 $\frac{\mathrm{mJ}}{\mathrm{cm}^2}$ of incident fluence with 1030 nm centre wavelength, resulting in a shift and distortion of the Bragg peak corresponding to the displayed strain.

10.3.1. Magnetic strain

Clearly, the different directions of the magnetic field do not affect the experimental outcome in terms of measured strain. Partly this may be due to the difference of an order of magnitude in strain compared to the static measurements where a maximum of $6 \cdot 10^{-5}$ was recorded. Looking at Fig. 10.4, a maximum of $3 \cdot 10^{-4}$ is visible. Also, the measured strain scatters within a range of $5 \cdot 10^{-5}$. So even if the sample was switched into a different magnetic state during one excitation process, it would be difficult to see with the present data quality. Other more fundamental reasons for not seeing a dependence on the magnetic field are the experiment's implementation sequence and the data handling.

Concerning the measurement sequence it is important to note that the sample was only exposed to a saturation magnetic field once before the measurement. Afterwards, the delay scan begun with one pump pulse and an X-ray pulse to be diffracted by the excited sample at one certain delay (maybe even diffracted by the unexcited sample if the first delay was set to $t < t_0$). If the sample was changed in any way to a new magnetic state by the initial pump pulse, only one diffracted X-ray pulse could detect this change. For the second pump pulse, the magnetic state of the sample could not have been altered because the direction of the external field was not changed during the delay-scans. Thus, it is not the right way to detect the difference in the sample's magnetic state by looking at the relative change of the lattice spacing for each measurement. However, the absolute values of the lattice spacing hold the information about the magnetic state of the sample.

Therefore, I plotted the absolute difference between the measured lattice spacing d_{110} and it's literature value (5.195 Å) for four different magnetic field directions in Fig. 10.5. The global trend of the absolute value d_{110} is obviously similar to it's relative change in Fig. 10.4. But for $\beta = 90\,°$ and $270\,°$ the absolute value of d_{110} is on average $2.8 \cdot 10^{-4}$ Å larger than for $\beta = 180\,°$ and $360\,°$. This absolute offset of $2.8 \cdot 10^{-4}$ Å corresponds to a relative magnetostrictive strain of $5 \cdot 10^{-5}$, in good agreement with the static magnetostriction measurements in Sec. 7. There, a strain of $4 \cdot 10^{-5}$ for the different magnetic states was found, see Fig. 7.1. Here, in the time resolved measurements, the dynamics are independent of the applied magnetic field.

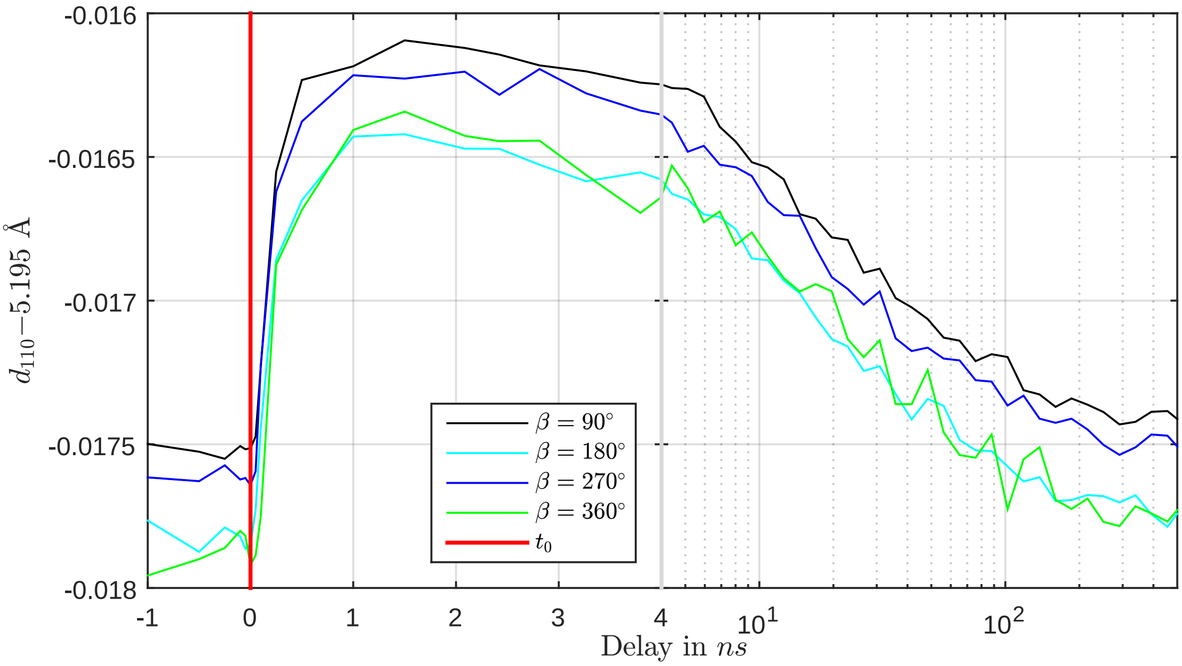

Figure 10.5: Time resolved lattice spacing along (110) for four different directions of an external magnetic field of 550 mT. The position of the Bragg peak was deduced by applying Gaussian fits.

10.3.2. Thermal strain

Although no dynamics associated with magnetostriction could be substantiated, the observed strain dynamics still provide important information about the dynamics in $TbFe_2$ after the excitation. Obviously, an expansion is visible due to heating of the sample via the pump pulse. An amount of energy is deposited in the sample, absorbed by the electrons from which it is transferred into the lattice (electron-phonon-coupling). The coupling of electrons (excited by an ultrashort laser pulse) and the lattice is subject of current research targeted on the development of an underlying model as well as on the identification of equilibrium coupling times [93, 94]. Additionally, magnetic systems shifted into the focus, adding the spin system interactions to the conception of ultrafast dynamics [6, 95]. Two- or three-temperature models are often used in the literature, although theory shows that temperature is not necessarily a valid quantity at short times after excitation. The idea is to associate temperatures to the electronic system, the lattice and the spins which can interact by scattering of electrons, phonons and magnons. Macroscopically this translates into three coupled heat baths from which only one is heated at t_0. The electrons absorb the pump energy which increases their temperature resulting in heat flowing to the lattice and spin system until a temperature equilibrium is reached. It is not easy to find electron-phonon coupling times of any rare earth metal in the literature, but according to U. Bovensiepen the typical order of magnitude is a few picoseconds [95]. Thus, this ultrafast equilibration can not be displayed by the measurements. Also, in my evaluation of dynamics in $\mathrm{TbFe_2}$, I do not consider magnons as interaction elements, i.e. dynamical magnetic response.

Even so, at a time scale of several nanoseconds, the sample is basically heated in a common way, meaning an amount of heat $Q(\vec{r},t)$ is deposited in an exponentially decaying spatial profile and propagates through $\mathrm{TbFe_2}$ according to classical heat diffusion [12], described by Fourier heat law:

$$\frac{\dot{Q}(\vec{r},t)}{A} = -\kappa \nabla T, \tag{10.1}$$

where κ is the heat conductivity, ∇T the temperature gradient and $\frac{\dot{Q}(\vec{r},t)}{A}$ the heat current density, i.e. the heat current passing perpendicularly through the area A. Inscribing an exponential temperature profile by the pump laser excitation pulse due to Beer-Lambert's law, results in a maximum temperature gradient at the surface, decreasing exponentially into the sample. Thus, the heat flows fastest out of the top layer into the sample and successively slower the more deeper it goes into the sample. Additionally, the heat is accompanied by an expansion, modelled by a linear thermal expansion coefficient ζ [12], see Eq. 10.2:

$$\frac{\Delta L}{L} = \zeta \Delta T, \tag{10.2}$$

where $\frac{\Delta L}{L}$ is the relative change in length during a temperature change ΔT. Although ζ and κ are in general temperature dependent [12], I assume constants for the sake of simplicity in the course of this thesis as they are implemented as constants during the simulations in Sec. 11. Also, for a the temperature range 150 K to 350 K linear thermal expansion could be substantiated at the PXS, see Fig. A.8 in the appendix. Focussing on the heating and expansion process, a maximum of the temperature induced strain ($\frac{\Delta L}{L}$) right after the excitation could be expected. This is obviously not accurate concerning the strain calculated by the Gaussian fit but applies to the COM data. Nevertheless that is not a contradiction as the strain is maximal right after excitation but only inside the top layer of $\mathrm{TbFe_2}$. The majority of the sample is yet to be heated and expanded. The Gaussian fit however is not sensitive to a small portion of the sample being strongly expanded because the diffraction signal of this thin layer is a broad, low intensity Bragg peak competing with an intense, narrow peak of the homogeneous remaining sample. Additionally, the diffracted intensity is even more reduced because of the inhomogeneous excitation profile. Not until a significant fraction of $\mathrm{TbFe_2}$ is heated and expanded, the major Bragg peak shifts and therefore a positive strain can be detected by the Gaussian fit.

The maximum around 2 ns (see Fig. 10.4) occurs because of two competing processes. On the one hand there is the reduction of the maximal and average strain because the initial temperature profile equilibrates and heat slowly propagates to the adjacent niobium layer. This results on the other hand in an increase of the strain detected by the Gaussian fit because the sample is successively homogenised, sharpening and intensifying the Bragg peak. Meanwhile, the COM evaluation is sensitive to a shift of the major Bragg peak as well as to the small, heated fraction of the sample providing a broad, low intensity Bragg peak. Consequently, the Gaussian fit is sensitive to the majority of the sample and the amount of inhomogeneity, whereas the COM evaluation is a measure of the average strain, as it reaches its maximum almost instantaneously after excitation and does not decrease until heat is flowing out to the adjacent niobium buffer.

11. Strain dynamics modelled by the udkm1Dsim-toolbox

In this section I provide an overview of the simulations to model the measured strain dynamics. Therefore I explain the concepts and implementation of the UDKM1DSIM-toolbox, depict the results and compare them with measured data. I derive a more sophisticated insight about the mechanics of $TbFe_2$ during the pump-probe experiments, as it is for example possible to picture a temporal and spatially resolved strain evolution at once.

To ensure a suitable interpretation of the strain data obtained at the PXS and BESSY II, I employed the UDKM1DSIM-toolbox [96], a collection of Matlab (MathWorks Inc.) routines and functions developed by the UDKM-group. With this I modelled a one dimensional representation of the sample along the out-of-plane direction by placing atoms in the right order and distance to create unit cells and subsequently material layers. This one dimensional representation was then exposed to the pump pulse resulting in structural dynamics because of thermal stress. Consequently, the strain was calculated by applying a linear-chain model of masses and springs. Eventually, dynamical X-ray diffraction was conducted on the excited sample at given delays by simulating the scattering of incident X-rays on single atoms over the entire sample.

Many publications of the UDKM concerning ultrafast XRD used this toolkit to fit their data and provide explanations for observed features, see [5, 6, 90]. Based on experience, a one dimensional approach provides a good approximation of the structural dynamics. This can be understood by taking a closer look at the spatial orders of magnitude. The $TbFe_2$ layer measures 500 nm in depth while typically a spot size on the surface with a diameter of 1200 μm is exposed to the pump pulse at the PXS. With an optical penetration depth of 22 nm, solemnly a one dimensional temperature dependence is inscribed into the region which is probed by the X-ray pulse and measures 300 μm in diameter. With a sonic speed of $4.6\,\frac{\mathrm{nm}}{\mathrm{ps}}$ it would take 65 ns for a strain wave to propagate from the outer rim of the excited spot to the probe region of the sample. Thus it is safe to assume a one dimensional problem structure to model structural dynamics on a pico- to nanosecond time scale especially for nanoscopic samples.

I will focus mainly on three distinguished parts of this procedure which are the heat deposition during the excitation and its diffusion in section 11.1, the coherent phonon dynamics arising from the initial excitation in section 11.2 and subsequently the simulated dynamical X-ray diffraction in section 11.3. All along, a comparison of the data from previous sections will be included to determine the sound velocity of $TbFe_2$ in Sec. 11.4. Additionally, I present evidence of fluence dependent ultrafast heat diffusion in $TbFe_2$ in Sec. 11.5.

To start off the simulation one must hand over important material properties to the simulation tool kit and construct the unit cells accordingly. In Table 11.1, all necessary quantities are listed to conduct the simulations via the UDKM1DSIM-toolbox. In contrast to niobium and sapphire, it was not possible for me to find exact values for the heat conductivity κ, the sound velocity v_{sound} and the linear thermal expansion coefficient ζ for $TbFe_2$. The given κ is associated with a Terbium-Dysprosium-Iron alloy, known as Terfenol ($Tb_{0.3}Dy_{0.7}Fe_{1.92}$), which is listed online. It is a well known magnetostrictive alloy for which the heat conductivity is documented [97]. The longitudinal sound velocity of polycrystalline $TbFe_2$ is $3.94\,\frac{\mathrm{nm}}{\mathrm{ps}}$ [7] but since the sample consists of a single crystal it is not surprising that a different value of $4.6\,\frac{\mathrm{nm}}{\mathrm{ps}}$ provides the best match of the simulation results and the measurement data, see Sec. 11.2 and 11.4. To determine the linear thermal expansion coefficient, the temperature dependence of the lattice spacing d_{110} was measured at the PXS via static XRD, see Fig. A.8 in the appendix. Also, the optical penetration depth according to Beer-Lambert's law was identified by ellipsometry measurements conducted by my colleague L. Willig. For niobium it was found to be 24 nm and for $TbFe_2$ 22 nm but the simulation of the UXRD signal (Fig. 11.6) shows that only a much higher δ of up to 55 nm matches the temporal strain evolution during the first hundred picoseconds after excitation. In fact, a correlation between the fluence and penetration depth could be observed, i.e. the length scale of the stress profile rises with higher fluences, see Sec. 11.5.

Table 11.1: Necessary material properties at room temperature for UDKM1DSIM-toolbox operation. Quantities marked with * are not associated with single crystal TbFe$_2$ but with similar materials as I could not find the exact values. The $^\times$ tagged items result from the simulation itself as those values provide a match of measured and simulated data, see Sec. 11.4 and 11.5. Those properties signed by † are determined by the UDKM group either by static XRD or ellipsometry, see Fig. A.8 in the appendix. The optical penetration depth for Sapphire was set to ∞ because the TbFe$_2$ and Nb layers absorb nearly the entire pump energy with the result that at maximum a fraction of 10^{-5} of the incident intensity would have penetrated the substrate.

	TbFe$_2$ layer	Nb buffer	Al$_2$O$_3$ substrate
lattice constants in Å			
c-axis (out-of-plane)	10.39 [17, 18]	4.67 [98]	4.76 [99]
b-axis (in plane)	10.39 [17, 18]	3.30 [98]	12.80 [99]
a-axis (in plane)	7.35 [17, 18]	4.67 [98]	8.24 [99]
heat conductivity κ in $\frac{\mathrm{W}}{\mathrm{mK}}$	10.8* [97]	58.3 [100]	40 [99]
heat capacity C_p in $\frac{\mathrm{J}}{\mathrm{kgK}}$	330 [101]	264.78 [102]	778.73 [103]
sound velocity v_sound in $\frac{\mathrm{nm}}{\mathrm{ps}}$	3.94* $\ldots$ 4.6$^\times$ [7]	5.083 [104]	11.075 [105]
mass density ρ in $\frac{\mathrm{g}}{\mathrm{cm}^2}$	9.0 [19]	8.57 [102]	4.05 [99]
optical penetration depth δ in nm	22† $\ldots$ 55$^\times$	24†	∞
lin. thermal expansion ζ in $\frac{10^{-6}}{\mathrm{K}}$	23.7†	7.6 [106]	6.6 [107]
layer thickness d in nm	500	100	10^6

11.1. Heat diffusion

After constructing the sample by manually defining the structural prototypes of unit cells and adding them to sample layers, the heat simulation can be conducted with the UDKM1DSIM-toolbox. For a given excitation pulse, the program assigns an exponentially decreasing temperature profile according to Beer-Lambert's law. Subsequently to the instantaneously modelled excitation, the temporal and spatial thermal evolution $T(z,t)$ is then calculated by solving the one dimensional heat diffusion equation 11.1 numerically, cf. [96]:

$$\rho(z)C_\mathrm{p}(z)\frac{\partial T(z,t)}{\partial t} = \frac{\partial}{\partial z}\left(\kappa(z)\frac{\partial T(z,t)}{\partial z}\right), \tag{11.1}$$

where $\rho(z)$ is the mass density, $C_\mathrm{p}(z)$ the heat capacity and $\kappa(z)$ the heat conductivity. The involved quantities are dependent on the sample's depth z as three different materials with different properties are part of the simulation. Furthermore $C_\mathrm{p}(z)$ and $\kappa(z)$ are usually temperature dependent but are set to the fixed values of table 11.1 during the course of this thesis. Eventually, the output, a spatial and temporal temperature map of the whole sample, is generated for further evaluation. Several spatial temperature profiles at different times after excitation are depicted in Fig. 11.1.

5 ps after the initial pump pulse, the exponential penetration profile originating from Beer-Lambert's law is still apparent. Successively heat diffuses deeper into the sample, rapidly reducing the temperature near the surface and increasing temperature in the remaining part of the sample slowly as in the process the flux is determined by the one dimensional temperature gradient $\nabla T(z,t) = \frac{\partial T(z,t)}{\partial z}$ and $\kappa(z)$

according to Eq. 10.1. The different values of $\kappa(z)$ for the three materials can be seen in the inset of Fig. 11.1 because the temperature equilibrates at higher rates in niobium and sapphire as compared to $TbFe_2$ and therefore decreases the spatial temperature slope. Apparently only after an elapsed time of 2 ns a considerable amount of thermal energy flows out of $TbFe_2$ heating the adjacent niobium buffer. Meanwhile the average temperature gradient within $TbFe_2$ is reduced from $9.2\,\frac{\mathrm{K}}{\mathrm{nm}}$ to $0.9\,\frac{\mathrm{K}}{\mathrm{nm}}$ inside the top 100 nm while being increased by a factor of ten inside the bottom 100 nm of $TbFe_2$, adjacent to niobium.

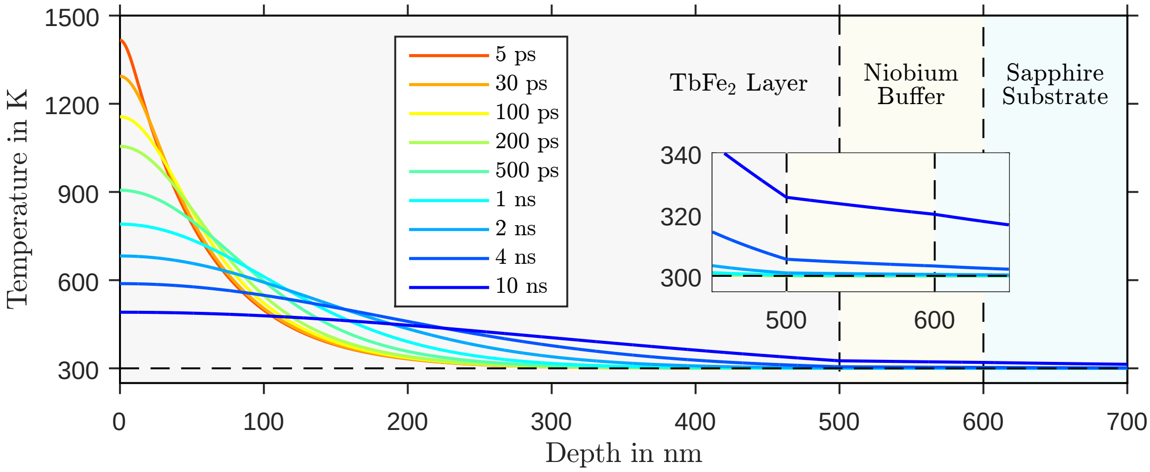

Figure 11.1: Spatial temperature profiles of the sample simulated at several times from 5 ps to 10 ns after an instantaneously excitation by a $20\,\frac{\mathrm{mJ}}{\mathrm{cm}^2}$ pump pulse and an optical penetration depth of 55 nm. The decently coloured background indicates different sample layers according to the sample depth, i.e. the $TbFe_2$ layer occupies the top 500 nm followed by 100 nm niobium and eventually the sapphire substrate from 600 nm on. The inset magnifies the spatial profiles at the $TbFe_2$-niobium-sapphire interface.

11.2. Coherent phonon dynamics

The calculated temporal and spatial temperature distribution is evaluated in this section with respect to the resulting structural dynamics. Mainly the concept of linear thermal expansion (Eq. 10.2) is applied including the elastic theory concerning (thermally induced) stress and its conversion into strain, as discussed in Sec. 5.1.3. The briefly explained fundamental processes are discussed by Schick et al. in depth [92].

The inscribed temperature profile not only equilibrates thermally due to heat diffusion but is also accompanied by a thermal stress which relaxes via the generation of hypersound and is described by the linear thermal expansion coefficient ζ. The latter provides the uniaxial length expansion ΔL caused by the temperature change ΔT. However, to elongate unit cells by ΔL according to their ΔT, space is needed which is initially, i.e. directly after pump excitation, still occupied by adjacent unit cells. Only the unit cell at the surface is adjacent to only a single unit cell on the one side and is able to release its stress by expanding to the other side. Alongside with an inherent expansion, the surface unit cell compresses the adjacent cell because of the discrepancy in stress, figuratively it pushes stronger. Because of the exponentially decreasing stress profile, this compression occurs also instantaneously deeper into the sample. Subsequently the unit cell below the surface will expand as it is not pressured any more by the cell on the top which is now strained but not stressed. The interaction of stressed, expanded and compressed unit cells propagates through the lattice as a bipolar strain wave with a compression travelling in advance pursued by an expansion [92], see Fig. 10.2.

In the UDKM1DSIM-toolbox this is modelled by an one dimensional model of masses and springs. A chain of harmonic oscillators is built with masses m_i according to the involved unit cells and springs k_i derived from the sound velocity $v_\mathrm{sound,i}$ and the lattice spacing c_i along the sample growth direction according to $k_\mathrm{i} = m_\mathrm{i} v^2_\mathrm{sound,i}/c^2_\mathrm{i}$. Thus, a multidimensional system of differential equations according to Eq. 11.2 is derived [96]:

$$m_\mathrm{i}\ddot{x}_\mathrm{i} = -k_\mathrm{i}(x_\mathrm{i} - x_\mathrm{i-1}) - k_\mathrm{i+1}(x_\mathrm{i} - x_\mathrm{i+1}) + m_\mathrm{i}\gamma_\mathrm{i}(\dot{x}_\mathrm{i} - \dot{x}_\mathrm{i-1}) + F^\mathrm{heat}_\mathrm{i}(t), \qquad (11.2)$$

where $x_\mathrm{i}(t) = z_\mathrm{i}(t) - z_\mathrm{0,i}$ expresses the absolute position change in relation to the initial position $z_\mathrm{0,i}$ of the unit cells. An empircal damping term $m_\mathrm{i}\gamma_\mathrm{i}(\dot{x}_\mathrm{i} - \dot{x}_\mathrm{i-1})$ is added as well as $F^\mathrm{heat}_\mathrm{i}(t)$, the thermal stress due to the pump excitation and heat diffusion numerically provided by the temporal temperature profile of Sec. 11.1. $F^\mathrm{heat}_\mathrm{i}(t)$ is realised by, figuratively speaking, placing incompressible sticks of the length ΔL between each spring and mass, where the ΔL is determined via Eq. 10.2. This represents the stress in terms of compressed springs before relaxation, and thermal expansion after relaxation. Solving this system of differential equations numerically with an inbuilt ordinary differential equation solver provides the temporal and spatially strain distribution $x_\mathrm{i}(t)/z_\mathrm{0,i}$. An example of the latter is depicted in Fig. 11.2.

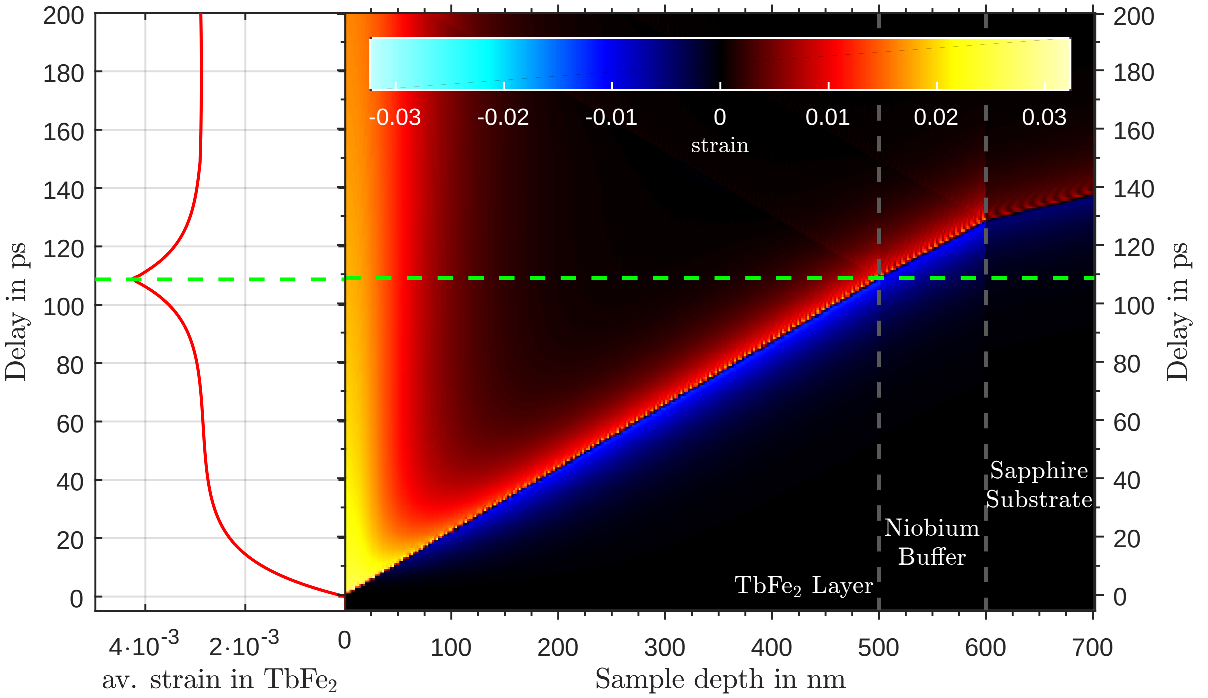

Figure 11.2: Spatiotemporal strain distribution $x_\mathrm{i}(t)/z_\mathrm{0,i}$ for pump probe delays of 0 to 200 ps, simulated with a fluence of 20 $\frac{\mathrm{mJ}}{\mathrm{cm}^2}$ and an optical penetration depth of 55 nm. The strain evolution of the top TbFe$_2$ layer, 100 nm niobium buffer and 100 nm of the sapphire substrate are displayed in the right plot. On the left, the average strain inside the TbFe$_2$ layer is displayed for the same time span. Moreover, the green dashed line at 108 ps marks the maximum of the average strain in TbFe$_2$ which is the moment when the entire compressive part of the bipolar strain wave (blue) is propagated into adjacent niobium.

All discussed features discussed in this section are visible in in Fig. 11.2, for example the expansion of surface near TbFe$_2$ due to heat and heat diffusion deeper into the sample while decreasing the temperature gradient near the top layers. Likewise the bipolar strain wave and its propagation through TbFe$_2$ lead by a compressive part (blue) and followed by an expansion (red) was calculated by the UDKM1DSIM-toolbox. This spatio-temporal strain profile is handed over in the following to a dynamic XRD simulation, calculating the time dependent diffraction signal of the sample, to calculate the transient Bragg peak of TbFe$_2$.

11.3. Dynamical X-ray diffraction

In this section, I briefly explain the procedure of the udkm1Dsim-toolbox to calculate XRD patterns and present the results of the simulation. The latter is the transient X-ray reflectivity for a strained sample according to the spatio-temporal strain distribution. Here, *dynamical* means that effects on the incident X-ray beam such as absorption, refraction, scattering and multiple reflections are taken into account. The toolbox calculates the X-ray reflectivity in accord with the concept of the scattering amplitude in Sec. 3.2.5. The main difference is the restriction in terms of the scattering vector $\vec{Q}$. As the toolbox models one dimensionally, only symmetric reflections can be simulated, i.e. the (220) Bragg peak of $TbFe_2$. The udkm1Dsim-toolbox is in detail described and explained by their authors Schick et al. [96]. Consequently however, the X-ray reflectivity for each diffraction angle ϑ or the associated q_z is calculated which corresponds to the measured intensity of the experiment. Subsequently, the temporal evolution of the Bragg peak of $TbFe_2$ is provided which is evaluated by the same fitting routines or COM procedure as the measured data. In Fig. 11.3 a comparison of the temporal evolution of the reflections is shown.

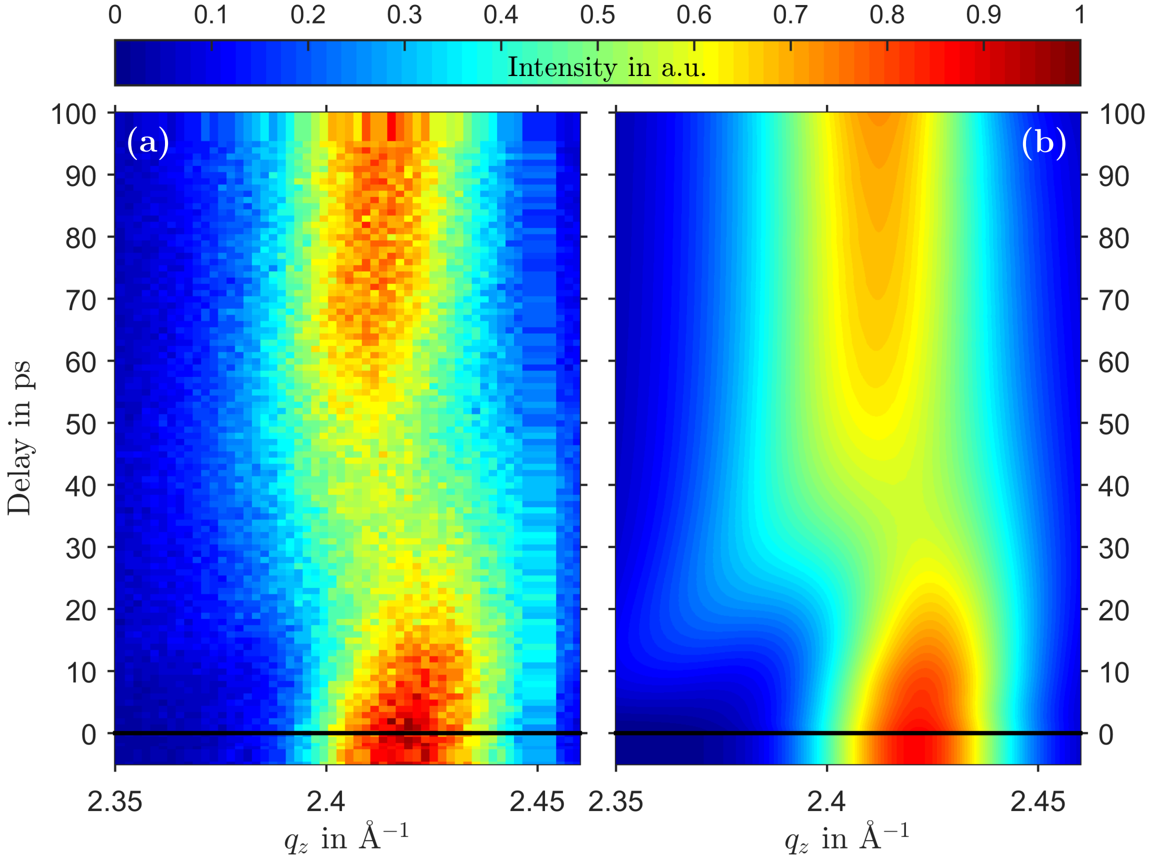

Figure 11.3: Measured **(a)** and simulated **(b)** temporal $TbFe_2$ (220)-Bragg peak evolution during the first 100 ps after excitation. The fluence was chosen to be 25 $\frac{\mathrm{mJ}}{\mathrm{cm}^2}$ at the PXS and 20 $\frac{\mathrm{mJ}}{\mathrm{cm}^2}$ for the simulated data. The excitation moment is marked as a black line at $t_{\mathrm{Delay}} = 0$ and the intensity is normalised for a comparable colour code. An optical penetration depth of 55 nm was set for the simulation in this case.

The temporal evolution of the modelled Bragg peak corresponds well to the measured reflections. At a pump-probe delay of 0 to 25 ps after excitation the main Bragg peak shifts to higher q_z which is associated with a compression of the majority of the $TbFe_2$ layer. The intensity of the Bragg peak decreases which is associated with an increasing disorder and inhomogeneity reviewed in the previous sections. Even the observed shoulders discussed in Sec. 10.1 and visualised in Fig. 10.1 are visible in Fig. 11.3. Between 10 and 40 ps and 2.35 and 2.4 Å^{-1}, a shoulder is appearing, increasing in intensity while shifting to higher q_z and eventually combining with the main peak. This shoulder is also more pronounced than the shoulder of the Bragg peaks measured at the PXS, see Fig. 11.4b. Subsequently, the main peak maintains its minimal intensity for 20 ps while shifting back to lower q_z as the strain wave propagated halfway through the TbFe$_2$ layer. At 50 ps after excitation the majority of TbFe$_2$ is expanded, as the position of the main reflection has shifted to lower q_z compared to its initial position. The maximal shift is recorded at 60 ps. And in succession a slight shift decrease of 30% for the measured and 5% for the simulated data is recorded.

As done already in Sec. 10.1, the Bragg peaks can be evaluated in terms their position in q_z. Fitting the main peak with a Gaussian function provides the centre position corresponding to the lattice spacing in the majority of the sample. Calculating the COM however gives the average strain in the TbFe$_2$ layer. The simulated transient strain, can therefore be calculated and is displayed and compared to BESSY II and PXS data in Fig. 11.4a.

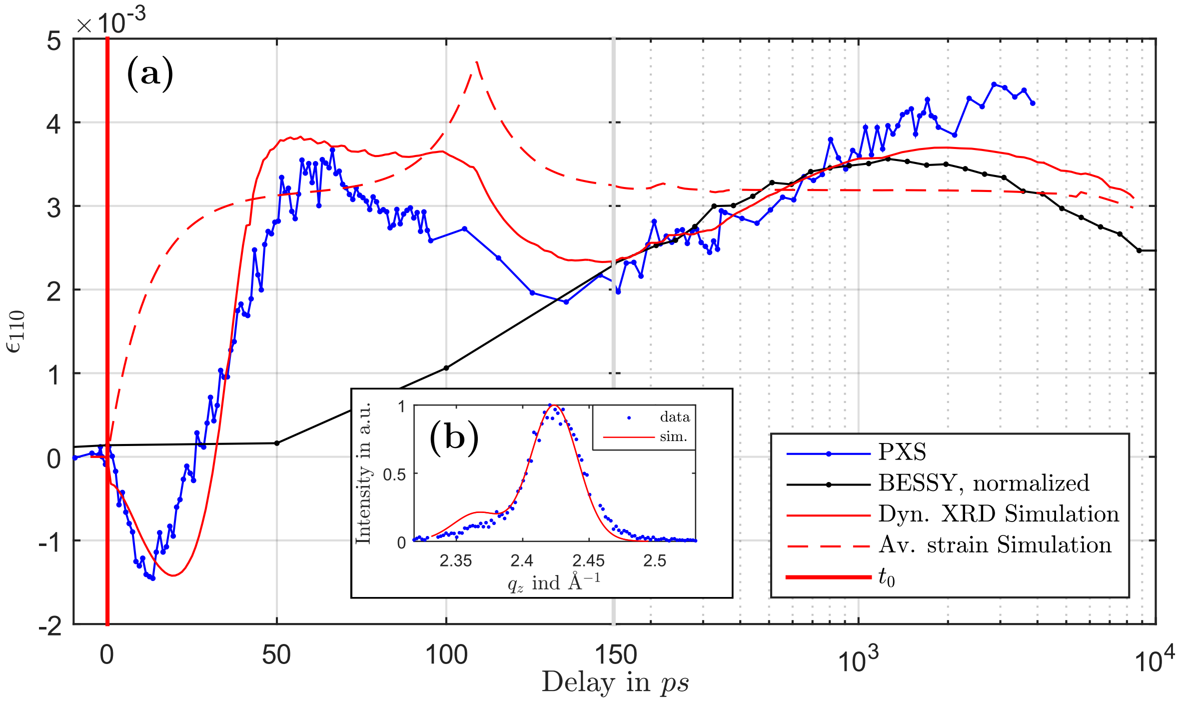

Figure 11.4: (a): Time resolved strain of TbFe$_2$ as measured at BESSY II and PXS as well as simulated after excitation with a short laser pulse at t_0. The incident fluence at PXS was 25 $\frac{\text{mJ}}{\text{cm}^2}$, at BESSY II 7.5 $\frac{\text{mJ}}{\text{cm}^2}$ and in the simulation 18 $\frac{\text{mJ}}{\text{cm}^2}$ was chosen. The BESSY II data are scaled with a factor of 10 for an easier comparison. The strain from the dynamical XRD simulation is provided via a Gaussian fit. Calculating the COM of simulated Bragg peaks results in a transient strain, which equals the average strain calculated by the toolbox and already seen in Fig. 11.2. **(b)**: Simulated Bragg peak and raw PXS data of the Bragg peak at 13 ps after excitation. An equally large shift to higher q_z and a shoulder at lower q_z can be observed.

The plain red graph results from the transient Gaussian fit evaluation of the simulated Bragg peaks in Fig. 11.3. The blue graph corresponds to the measured temporal Bragg evolution in Fig. 11.3. The initial decrease of the strain, the quick increase to a maximum at 60 ps and a subsequent strain reduction as well as the global maximum at 2 ns (discussed in Sec. 10.3.2) are features visible in both data sets.

All in all, the transient response of the Bragg peaks corresponds well to the known response of single crystalline materials exposed to an ultrashort pump pulse, which is a main research field of the UDKM group. Two distinct observations concerning the temporal evolution of the reflections are usually made during similar measurements, in particular peak-splitting and peak-shifting [90, 108]. Peak-splitting means that the Bragg peak is split into two distinct reflections after the excitation, i.e the shoulder has around 50% of the diffracted intensity. Thus, two lattice constants can be associated with the diffracting sample, usually corresponding to the fraction excited by the pump pulse which is therefore expanded and to the unexcited part which is not yet heated due to insufficient penetration of the pump pulse. Peak-shifting on the other hand occurs if the excited diffracting material layer is thin in relation to the penetration depth so that the sample's diffracting part is homogeneously heated after excitation. In the course of this thesis, a hybrid of both phenomena is observed. The peak shifts to larger q_{z} after excitation, because of a compression of the majority of the layer. Simultaneously, a shoulder appears at smaller q_{z}, associated with the expanded part of the layer. This is because 90% and more of the sample is not excited by the pump pulse. Subsequently, the shoulder increases in intensity, i.e. the peak shifts to smaller q_{z} because the majority of the sample expands.

11.4. Determination of sound velocity in TbFe$_2$

In this section I match the simulated and measured data to determine the sound velocity of TbFe$_2$. As discussed in the beginning of Sec. 11, I could not find some material properties of single crystal TbFe$_2$ as a necessary input for the UDKM1DSIM-toolbox, in particular v_{sound} along the (110) direction. The sound velocity in crystals depends on the propagation direction and can be derived from the elements of the elastic tensor C_{ij} [56] but since I could neither provide those, I determined the sound velocity in TbFe$_2$ by matching the measured data to the simulated results. Because the strain oscillation observed at the PXS during the first 150 ps after excitation is caused by the bipolar strain wave propagating through the 500 nm TbFe$_2$ layer, its time scale depends on the sound wave's velocity which is the sound velocity along (110) direction. I tuned v_{sound} to achieve the best match measured strain at the PXS. The measured strain and modelled results for three different sound velocities are displayed in Fig. 11.5.

Considering $v_{\mathrm{sound}} = 4.6\,\frac{\mathrm{nm}}{\mathrm{ps}}$ provides obviously the best result as the strain retains negative values for the first 30 to 35 ps and reaching a maximum between 50 and 60 ps. Afterwards it decreases slightly until the strain drops more significantly at 100 ps, manifesting at a local minimum between 130 to 150 ps and subsequently rises to the global maximum. Although the slopes of the simulations do not fit the measured data during the strain oscillation, the global trend and the moments for significant features, i.e. extrema and signs of slopes, are fitted best with a chosen sound velocity of $4.6\,\frac{\mathrm{nm}}{\mathrm{ps}}$. A change in v_{sound} leads to a mismatch of the measured and modelled strain. The maximum at 60 ps is reached too early for a higher sound velocity. Also, the strain-decrease at 100 ps, associated with the excitation of the sound wave's expansive part to the adjacent niobium layer, occurs 20 to 30 ps later than measured if utilising a lower sound velocity. Consequently I chose to set the sound velocity in TbFe$_2$ to the fixed value of $4.6\,\frac{\mathrm{nm}}{\mathrm{ps}}$ as this fits the data best at my discretion even if tuning the speed with a resolution of $0.1\,\frac{\mathrm{nm}}{\mathrm{ps}}$.

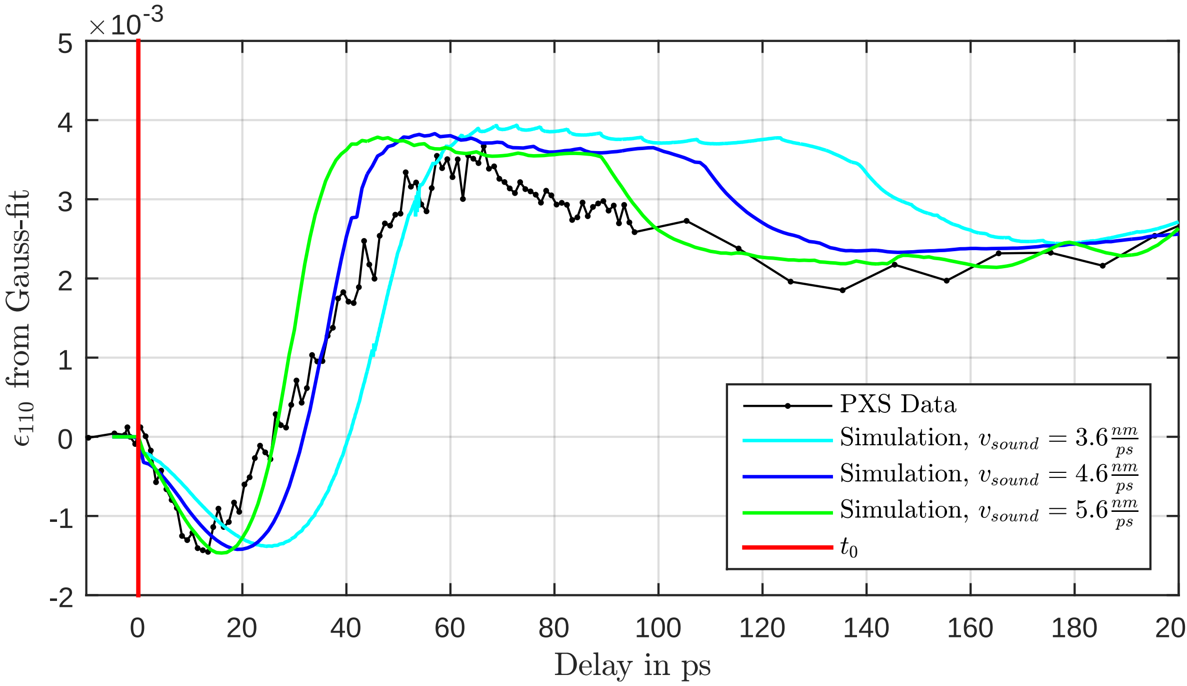

Figure 11.5: Strain calculated by Gaussian fits over 200 ps of pump-probe delay time. The black line represents the PXS data for a fluence of 25 $\frac{\mathrm{mJ}}{\mathrm{cm}^2}$. Three simulation results with different sound velocities, a fluence of 20 $\frac{\mathrm{mJ}}{\mathrm{cm}^2}$ and an optical penetration depth of 55 nm are displayed.

11.5. Fluence dependent ultrafast heat diffusion

Another aspect which must be discussed is the impact of the optical penetration depth δ which is found to be 22 nm at a wavelength of 800 nm by ellipsometry measurements, conducted by L. Willig of the UDKM group. Forwarding this value to the udkm1Dsim-toolbox results in a significant mismatch between measured and simulated data, especially for high fluences, see Fig. 11.6. However, this discrepancy is mainly apparent for delay times after the observed sign reversal of the PXS data, while the minimum directly after excitation is modelled rather well. If utilizing a penetration depth of 55 nm, the simulation result fits the measured data significantly better for delays with an associated positive measured strain whereby the improvement in match increases with the fluence. In the first 15 to 30 ps (dependent on the fluence) the sample responds as if the penetration depth was 22 nm. The depth and position of the minimum is determined by the dynamics of the bipolar strain wave which are coupled to the initial stress profile inscribed during excitation. Apparently, assuming a larger penetration depth does not provide the stress profile necessary to result in the minimum of the measured strain during the first 15 to 30 ps. However subsequently, only a transient state associated with a larger penetration depth of 55 nm matches the data. The most obvious difference in these cases is the inscribed stress profile due to thermal excitation. But consulting Fig. 11.1 it becomes apparent that the temperature profiles register only minor changes from 5 ps to 30 ps due to the heat conductivity of 10.8 $\frac{\mathrm{W}}{\mathrm{mK}}$ which is mainly the limiting factor concerning heat diffusion. The sample is initially excited with a penetration depth of 22 nm, because the corresponding stress profile determines the dynamics of the strain wave during the first 15 to 30 ps. A possible explanation is that subsequently, the heat propagates significantly faster than predicted by the Fourier heat diffusion (which can be approximated by an initially larger penetration depth), accompanied with a faster and stronger expansion.

Phenomena of ultrafast heat diffusion are discussed since 1987, when Brorson et al. introduced an new mechanism of heat transport. They detected heat propagation in thin gold films which was orders of magnitudes faster than the usual heat conductivity of gold would provide. This was explained with hot,

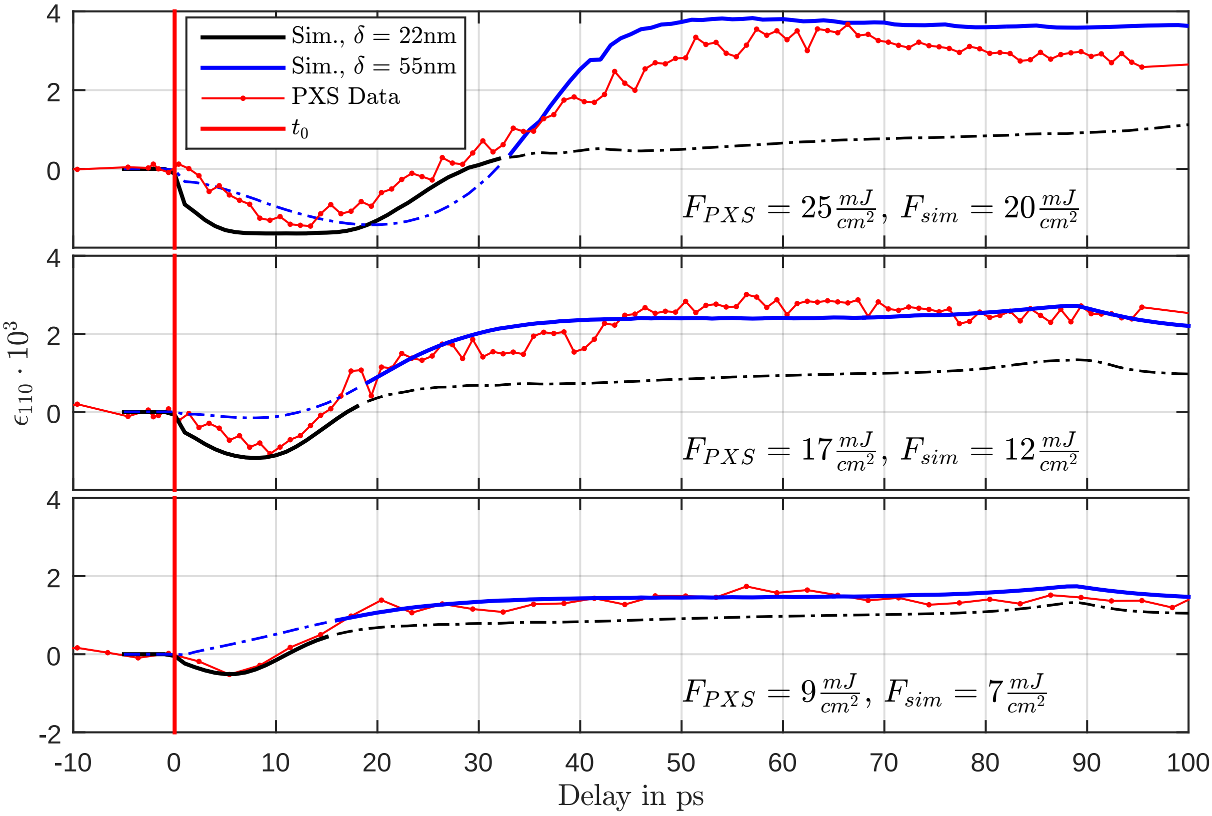

Figure 11.6: Time dependent strain, derived by a Gaussian fit of Bragg peaks measured at the PXS or calculated by the UDKM1DSIM-toolbox. In each of the plots, the red graph is associated with the PXS measurement at a certain fluence F_{PXS}, noted in the bottom right corner. The modelled strain is depicted for two different optical penetration depths $\delta = 22\,\text{nm}$ (black) and $55\,\text{nm}$ (blue) whereas the input fluence F_{sim} is the same and placed in the bottom right corner. Thereby, the ratio of F_{PXS} and F_{sim} is chosen to be similar for each plot. As different regimes of the modelled strains match to certain parts of the measured data, the graph is plain for the simulation which fits best at a particular time and is dashed otherwise.

non-equilibrium (ballistic) electrons which propagate quickly after excitation deep into the sample. They equilibrate with phonons after long electron propagation paths and therefore conduct heat faster. Thus they distort the spatial thermal profile and the resulting stress profile on a femtosecond time scale [109].

Another approach concentrates on the electron-phonon coupling time τ which was mentioned in Sec. 10.3.2. Typically, this coupling time is on the order of magnitude of a few picoseconds [95], but it is not a constant. Is has been shown, that the electron-phonon coupling time scales linearly with the heat capacity of electrons C_e [110]. The latter is a function of the temperature T_e of the electronic system, according to the Sommerfeld-model of a free electron gas [12]:

$$\tau \sim C_\mathrm{e} = \gamma T_\mathrm{e}, \tag{11.3}$$

where γ is the Sommerfeld constant. Because T_e is increased drastically after photo excitation, especially at high fluences, the electron-phonon coupling time increases. Also, the heat conductivity of the electronic system is usually much larger than the conductivity of the phonon system. Thus, hot electrons propagate deeper into the sample before coupling with the phonon system resulting in a flatter temperature profile. This is accompanied with an extended and delayed stress profile. In essence, at high fluence the excited electrons live longer and therefore conduct more heat compared to low fluence. In addition the very large electron temperature lead to very large temperature gradients, accelerating the heat transport even more.

12. Outlook for ultrafast X-ray diffraction

So far, I studied the ultrafast lattice dynamics in $TbFe_2$ after laser excitation and I could observe magnetostriction as a static offset in the presented measurements. Consequently I propose a new experiment to examine the magnetostrictive dynamics during the laser induced magnetization-switch process (see Appendix A.6), where strain and magnetization change as shown in the static measurements (Part II). In principle, a pump-probe setup should be used, just as presented in this thesis (PXS and BESSY II). But to scan the strain during the switching process which is induced by the pump pulse, the sample needs to be exposed to a saturation magnetic field before the sample is pumped again. This way, we magnetise the sample in the same way before each pump pulse. A succeeding probe pulse would then provide the strain at a certain time during the switching process. The sample is magnetised to saturation ($> 1\,\mathrm{T}$) at first, is then exposed to a magnetic field of $550\,\mathrm{mT}$ at an angle of $170\,^\circ$ in relation to the initial magnetization which is not enough yet to switch the magnetization. Then, the sample is exposed to the pump pulse which triggers the magnetization switch and a change in strain. The latter is measured by the succeeding probe pulse at a certain time and then, the sample is remagnetised to saturation to restart the measurement routine.

There are however technical difficulties to overcome. Strong magnetic fields of over $1\,\mathrm{T}$ are precarious to handle and slow to change, which is why the conduction of the proposed experiment may take a long time. Alternatively, we could use another material than $TbFe_2$ which has a significantly smaller anisotropy energy and is thus much easier to magnetise, i.e. with small magnetic fields. Regardless of the final implementation, this experiment may provide pieces of information about whether or not the coherent strain wave or the heating of the sample is responsible for the facilitation of the magnetization switch. Also, we could determine the time scale of the switching process.

Furthermore, I could to use the UDKM1DSIM-toolbox to provide quantitative proof for the interpretation of ultrafast electronic heat transport and increased electron-phonon coupling time in Sec. 11.5. A two-temperature model with variable electron-phonon coupling time would have to fit to the fluence dependent data, based on the assumption of a electronic heat capacity which linearly increases with the temperature, according to the Sommerfeld model.

Summary

The presented X-ray diffraction measurements on a 500 nm layer of $TbFe_2$ provide a self consistent view of the magnetostrictive response and ultrafast structural dynamics, confirmed by a qualitative theoretical evaluation of the observables.

I acquainted myself with the commonly accepted concepts of magnetostriction, which is mainly an assignment of potential energies to different subsystems of magnetostrictive materials. This concept contains terms like the elastic energy of the lattice, the magnetocrystalline anisotropy energy which determines the easy and hard crystalline axis' of magnetic materials, the Zeeman energy held by a magnetic moment associated with a magnetization inside a magnetic field and the magnetoelastic energy which describes the interaction of the lattice and magnetization. Usually, the sum is subsequently minimised with respect to the strain and the magnetization direction to receive the magnetostrictive response to initial conditions.

As I measured the out-of-plane magnetostriction forced by an applied magnetic field rotating in sample plane via static X-ray diffraction, I was able to model the magnetostrictive strain qualitatively utilising the minimisation of the potential energy sum and under the assumption of the separation of $TbFe_2$ into ferromagnetic domains with distinctive magnetization directions. The ordering of $TbFe_2$ is documented as well as the resulting magnetization direction of the domains corresponding with the magnetic easy axis which is the (111) direction (or equivalent directions in cubic symmetry) according to the minimisation of the anisotropy energy. I calcualted the resulting strain with Akulov's law which represents the magnetoelastic interaction and allocates magnetostriction to the magnetization direction. The measured as well as modelled data show a sinusoidal increase of the strain starting at a minimum where the sample's macroscopic magnetization is aligned to the external field. By rotating the magnetic field a maximum strain is reached a few degrees before an antiparallel state of the initial magnetization and the external field is employed. From there, the strain vanishes rapidly since the magnetization realigns with the external field to minimize the Zeeman energy. I conducted the measurements at two different experimental stations, utilising the MFXT setup of the UDKM group and the synchrotron BESSY II of the HZB and fortunately all results coincide. A constant factor mismatch of the modelled data, as a maximal strain of $6 \cdot 10^{-5}$ was recorded with an external field strength of 550 mT, is associated with an epitaxial clamping of the $TbFe_2$ layer.

Furthermore, I conducted ultrafast structural dynamics studies on $TbFe_2$ via X-ray diffraction once again at two different experimental stations; At BESSY II of the HZB and the PXS of the UDKM group. The sample was exposed to an ultrashort laser pulse and subsequently probed by a similarly short X-ray pulse, providing the sample's out-of-plane lattice spacing as a function of the pump probe delay time. All measured and modelled data show a thermal expansion of up to $4 \cdot 10^{-3}$. The superior time resolution of the PXS (down to one picosecond) enabled recording the strain oscillation during the first 100 ps after laser excitation which corresponds to a bipolar strain wave propagating through the $TbFe_2$ layer according to the modelling of the UDKM1DSIM-toolbox. The utilisation of the toolbox additionally suggest an ultrafast heat diffusion process, particularly during the first 30 ps and increased by high fluences. We suggest that the nonequilibrium of electron- and phonon-temperatures leads to the enhanced heat conductivity κ, because κ_{electron} is larger than κ_{phonon}.

A. Appendix

Simulation of field rotation several β-series

External field strength: $550\,\mathrm{mT}$

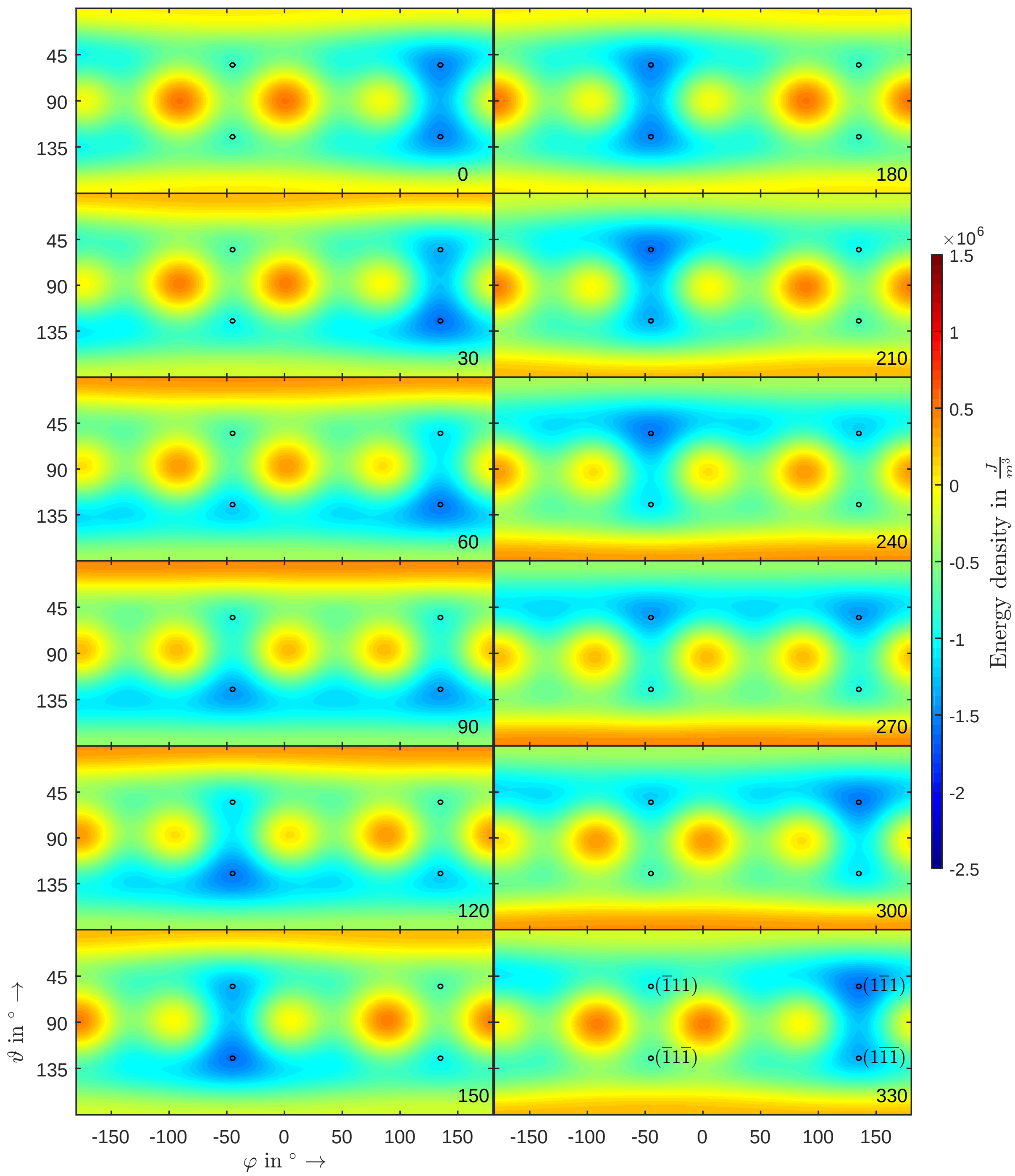

Figure A.1: Energy density map of E_{total} for $B_{\text{ext}} = 550\,\mathrm{mT}$. The number in each segment is the corresponding angle β and for each graph. Also, four crystallographic axes are marked.

External field strength: $550\,\mathrm{mT}$**, no** E_{shape} **energy term**

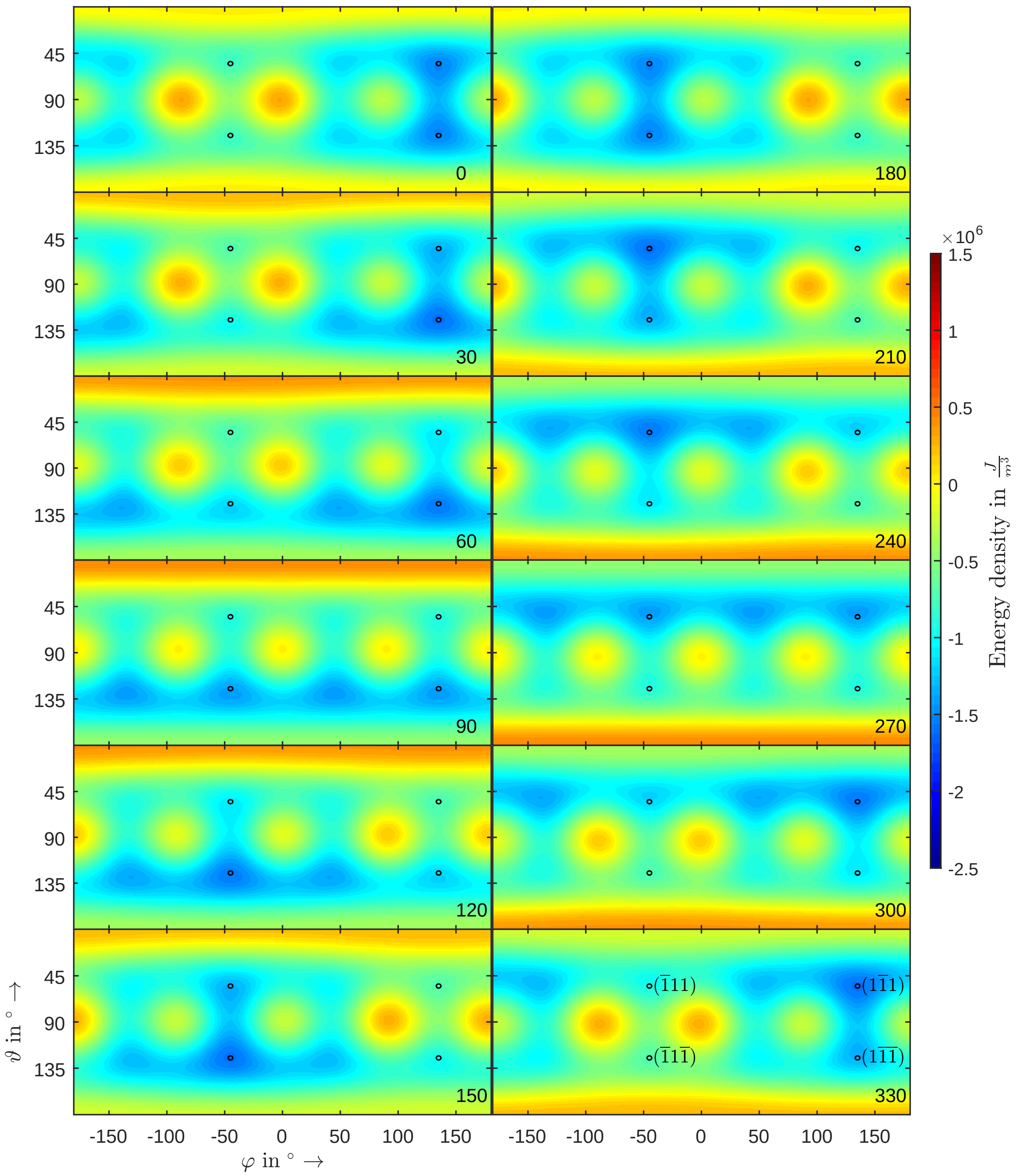

Figure A.2: Energy density map of E_{total} for $B_{\text{ext}} = 550\,\mathrm{mT}$ **with neglected shape anisotropy energy** E_{shape}. The number in each segment is the corresponding angle β and for each graph. Also, four crystallographic axes are marked.

External field strength: $1100\,\mathrm{mT}$

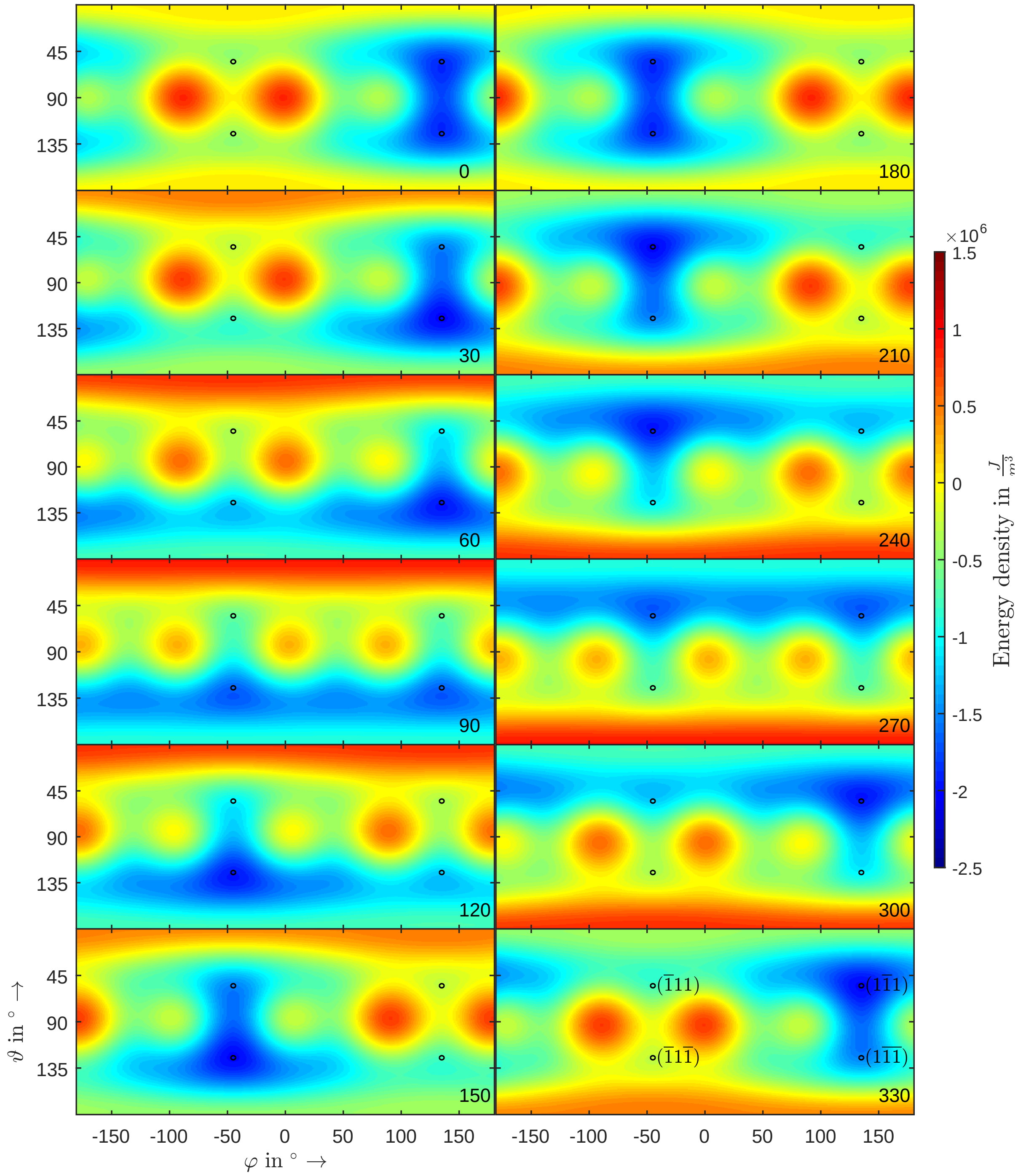

Figure A.3: Energy density map of E_{total} for $B_{\text{ext}} = 1100\,\mathrm{mT}$. The number in each segment is the corresponding angle β and for each graph. Also, four crystallographic axes are marked.

External field strength: 150 mT

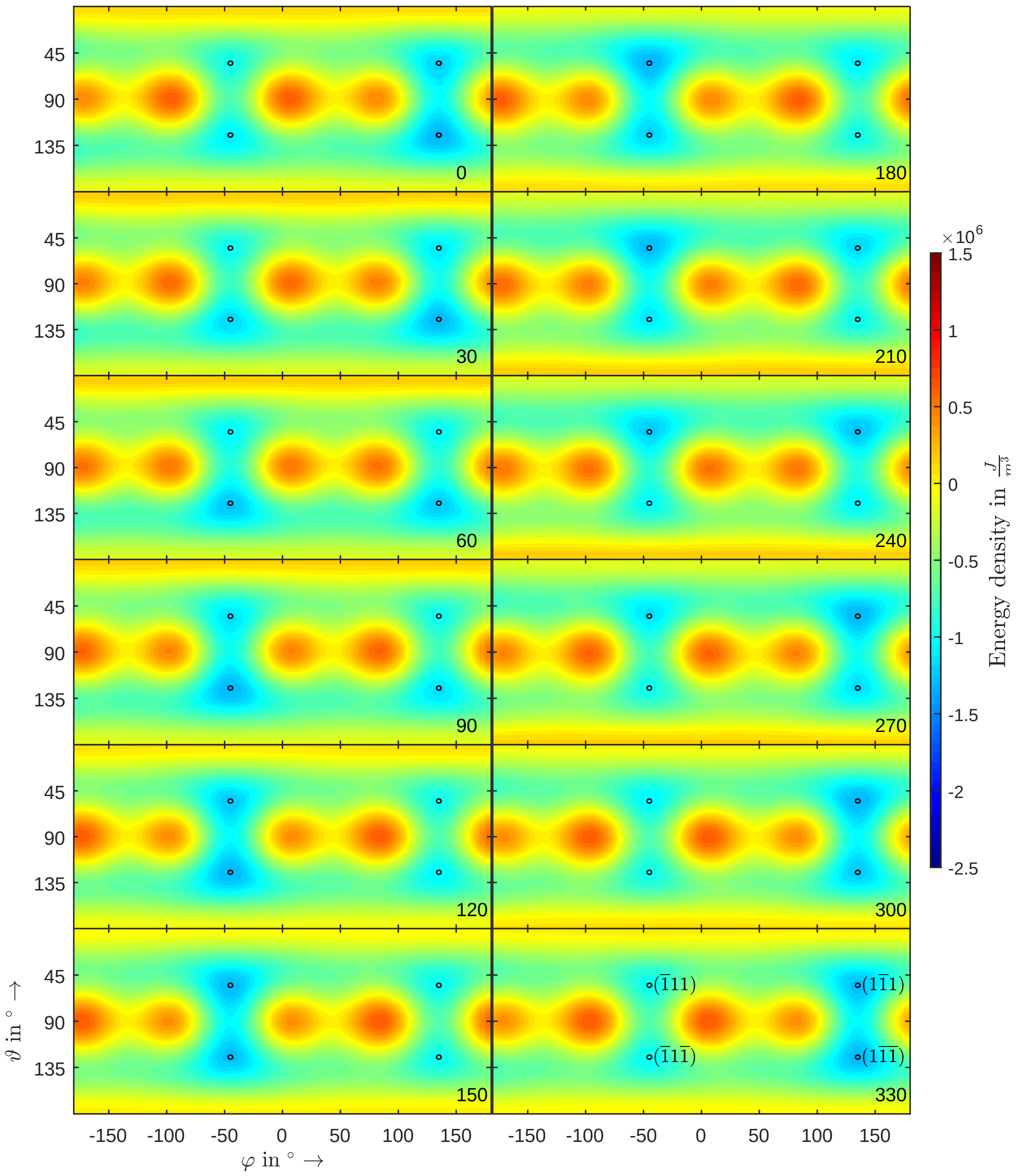

Figure A.4: Energy density map of E_{total} for $B_{\text{ext}} = 150\,\text{mT}$. The number in each segment is the corresponding angle β and for each graph. Also, four crystallographic axes are marked.

Simulated strain in a mono-domain model

In Fig. A.5, the simulated strain for three different situations is plotted together with the strain from static magnetostriction BESSY II measurements. It is clear that both simulations in which a mono-domain approach was used (red), are not matching the data. The extrema are not in the right place and it shows in general a different progression. Only the switch around 180 ° is visible in all simulations. That is because I manually changed the energetic minimum at that angle as the magnetization measurements of Sec. 7.2 show a switch in the magnetization at that angle. Only the combination of both strains in the multi-domain approach (blue) gives a qualitative agreement with the data.

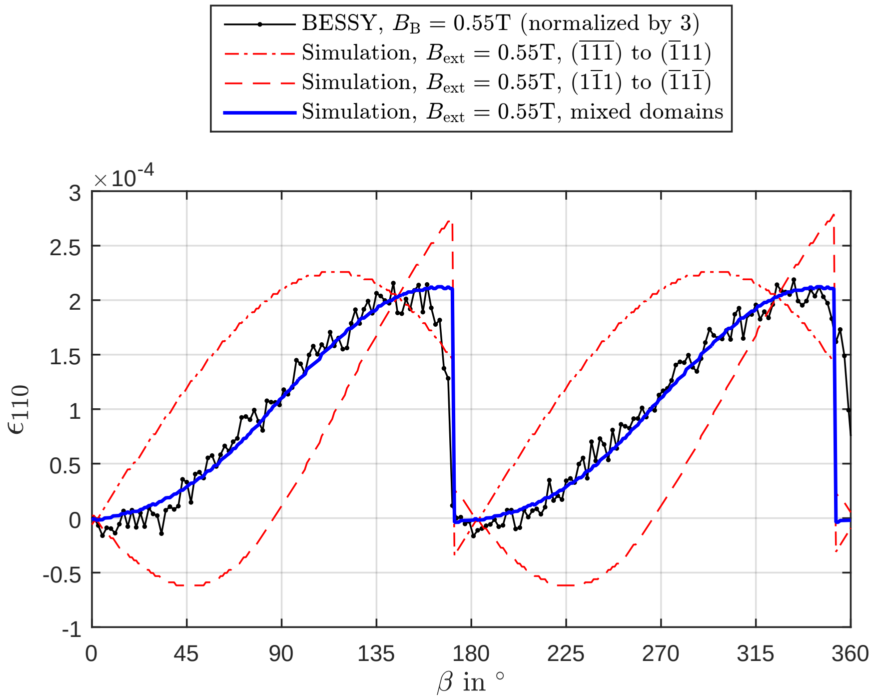

Figure A.5: Calculated and measured strain of $TbFe_2$ due to a rotation of an external field by the angle β. The black graph shows the data (multiplied by 3), the red dashed-dotted line shows the simulated strain if assuming that the magnetization in the sample points everywhere in the sample along the $(1\overline{11})$ direction for the first 180 ° and switches to the $(\bar{1}11)$ direction afterwards. The dashed red line results from a similar assumption, only taking different crystallographic directions into account, $(1\bar{1}1)$ and $(\bar{1}1\bar{1})$. The blue graph originates from a combination of both as the sample is not seen homogeneous, but evenly segmented in domains with either one of the two magnetization directions.

Laser assisted magnetic switching

During the experimental work at BESSY II we tested, if the rotation of the magnetization in a rotating in-plane magnetic field could be modified by laser-pulse excitation. As examplified in Fig. A.6, we observed the switching of magnetization at a lower β angles when the sample was excited with a pump laser. The pulsed pump laser, which is usually used for time resolved measurements and is characterised in Sec. 9, was focussed on the sample during the course of a β scan. The observed discontinuity in strain associated with a magnetization realignment (cf. 7.1) could thus be induced at lower angles β. For several incident laser fluences, the switching process is displayed in Fig. A.6. Although depicted measurements show the general trend that the switch relocates to a lower rotation angle β with increasing fluence, more measurements with significantly higher fluences show a contradictory dependence. In the displayed data, a memory effect becomes apparent as two measurements without laser excitation significantly differ from each other, if the sample was exposed to light in between. This rules out stationary heating with lowered energetic potential barriers as a sample process. Maybe the magnetization is trapped in a local minimum of the energy density map modelled in Sec. 7.3. As the time was limited, no consistent result or reasonable strategy to examine this feature was found, therefore this can be the content of upcoming research on $TbFe_2$.

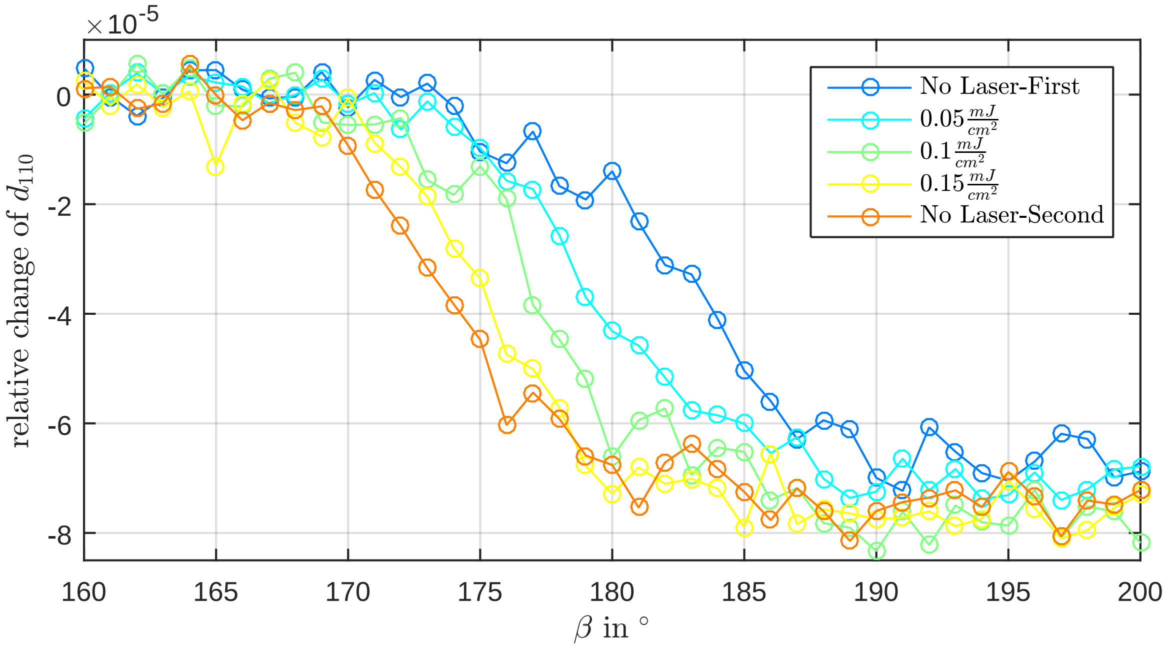

Figure A.6: Relative change of the lattice spacing along (110) direction in dependence of the external magnetic field's angle β at a field strength of 550 mT. The relative change was derived from a Gaussian fit of the Bragg peaks corresponding to d_{110} and the five displayed results are recorded subsequently according to their order in the legend.

Ultimately, a study about the laser induced magnetic switching of the sample could be conducted in the future focussing on the microscopic dynamics during the remagnetization process. It would be interesting to differentiate between the impact of a single laser pulse and the heating at longer time scales and which of those effects is responsible for the easier switching. On the one hand, a thermal excitation of $TbFe_2$ is accompanied with an significant decrease of the anisotropy constants K_i, see Fig. 5.4, that can soften the magnetic response of the sample, i.e. the magnetization is more easily realigned. However, a bipolar strain wave on the other hand, which is observed during time resolved measurements in Sec. 10, could also work as a seed for a magnetization switch, propagating through $TbFe_2$. The latter would be a directly forced magnetostrictive effect of inverse nature as the material is stressed and strained to evoke a change in the magnetization, cf. Kovalenko et al. [82].

Sub-nanosecond strain dynamics at BESSY II

Figure A.7 shows the temporal strain profiles measured at BESSY II, similar to the results discussed in Sec. 10.3 but with a different time resolution. It is depicted here to display the highest possible time resolution which can be reached at BESSY II. However, compared to the PXS, the superior time resolution of the PXS becomes apparent as the strain oscillation during the first 100 ps can not be resolved at BESSY II.

The strain reaches a saddle point during the first 100 ps to 200 ps after the excitation independent of the calculation method of the strain. The Gauss-Fit strain continues to increase by 50% to the global maximum around 1 to 2 ns before decreasing at larger times while the COM strain stays relatively constant from 200 ps to 2 ns until decreasing as well. This trend corresponds well to the interpretations in Sec. 10. The steady increase of the Gauss-Fit strain until 2 ns in contrast to the constant COM strain is an effect of dynamical X-ray diffraction.

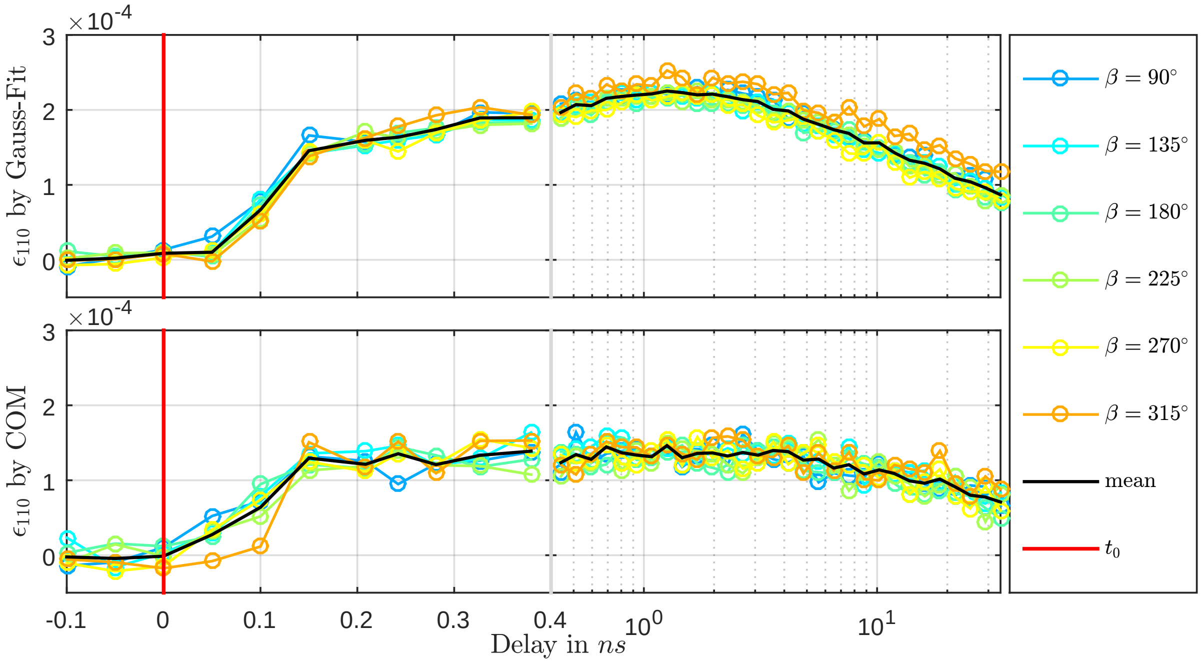

Figure A.7: Time resolved strain of $TbFe_2$ after Laser excitation at t_0 along (110) direction. The strain is either calculated by a Gauss-Fit (**top**) or the COM method (**bottom**) and is derived at six different directions (β) of an external magnetic field with a strength of 550 mT. The sample was exposed to 7 $\frac{\mathrm{mJ}}{\mathrm{cm}^2}$ of incident fluence with 1030 nm centre wavelength, resulting in a shift of the Bragg peak corresponding to the displayed strain.

Static thermal strain

The PXS possesses the ability to conduct XRD statically, i.e. without a sub picosecond time resolution of pump probe experiments. Additionally a cryostat is present to cool down samples from room temperature to 15 K. Since the cooling procedure takes long time, a homogeneous temperature of the sample is ensured before XRD is performed to determine the lattice spacing out-of-plane d_{110}. The temperature dependent relative change of d_{110} is displayed subsequently in Fig. A.8, leading to a linear thermal expansion coefficient of $\zeta = 22.7\,\frac{10^{-6}}{\mathrm{K}}$ by fitting the linear regime between 150 K and 350 K.

ζ is mainly determined by the heat capacity C_V which is a function of the temperature. At low temperatures, below 150 K, C_V is proportional to T^3 and thus ζ is also not constant. At larger temperatures above 150 K, C_V and thus ζ become constants [12].

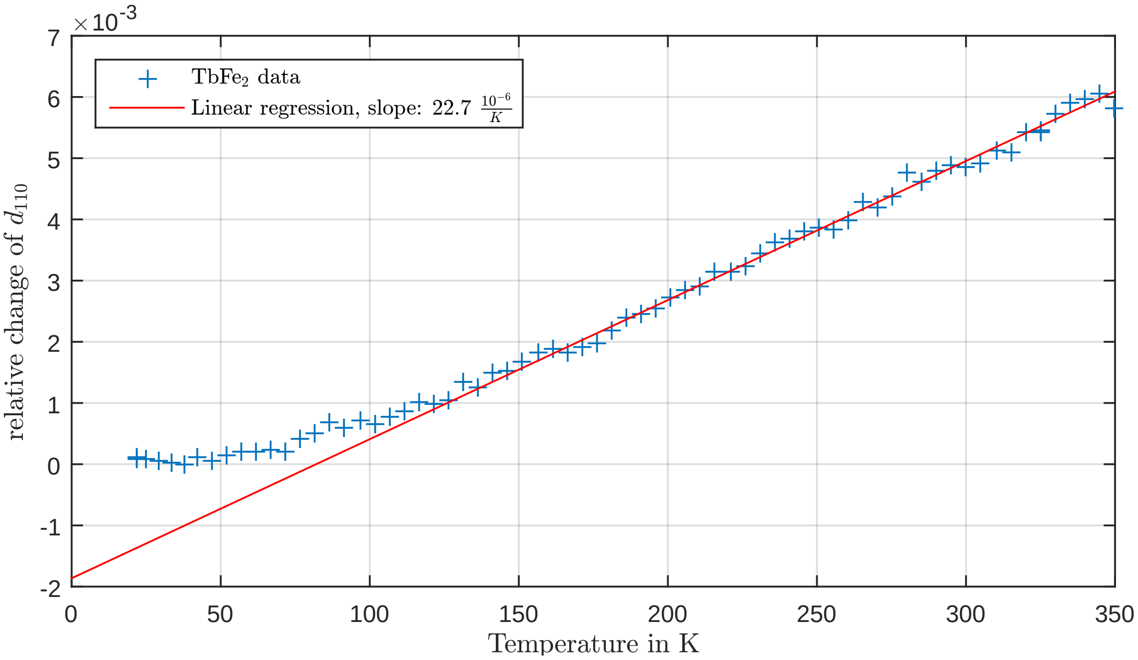

Figure A.8: Temperature dependent relative change of the lattice spacing d_{110} measured statically at PXS. The Bragg peak associated with the (110) set of planes was fitted with a Gaussian function to obtain the position of the maximum corresponding to d_{110}. The relative change of latter was determined for a range of temperatures and a linear regression subsequently provides the linear regime's slope starting at 150 K upwards to 350 K. It is specified to be $22.7\,\frac{10^{-6}}{\mathrm{K}}$, resembling the linear thermal expansion coefficient ζ.

References

[1] J. P. Joule. XVII. On the effects of magnetism upon the dimensions of iron and steel bars. *The london, edinburgh, and dublin philosophical . . .*, 1847. URL: `http://www.tandfonline.com/doi/pdf/10.1080/14786444708645656`.

[2] A. E. Clark and H. S. Belson. Giant Room-Temperatur Magnetostriction in TbFe2 and DyFe2. *Physical review b*, 5(9):91–95, 1972.

[3] N. S. Akulov. Über ein Gesetz, das verschiedene Eigenschaften ferromagnetischer Kristalle miteinander verknüpft. *Zeitschrift für physik*, 59(3-4):254–264, 1930. ISSN: 1434-6001. DOI: `10.1007/BF01341430`. URL: `http://link.springer.com/10.1007/BF01341430`.

[4] C. Kittel. Physical Theory of Ferromagnetic Domains. *Reviews of modern physics*, 21(4):541–583, 1949. ISSN: 0034-6861. DOI: `10.1103/RevModPhys.21.541`. URL: `http://journals.aps.org/rmp/abstract/10.1103/RevModPhys.21.541`.

[5] J. Pudell. Ultraschnelle Magnetostriktion von antiferromagnetischem Holmium. Master Thesis. Universität Potsdam, 2015.

[6] A. von Reppert. Ultrafast Magnetostriction in Dysprosium studied by Femtosecond X-Ray diffraction. Master Thesis. Universität Potsdam, 2015.

[7] A. E. Clark. *Alloys and Intermetallics.* Volume 2 of *Handbook on the Physics and Chemistry of Rare Earths.* Elsevier, 1979, pages 231–258. ISBN: 9780444850218. DOI: `10.1016/S0168-1273(79)02006-7`. URL: `http://www.sciencedirect.com/science/article/pii/S0168127379020067`.

[8] G. Engdahl and I. Mayergoyz. *Handbook of Giant Magnetostrictive Materials.* Elsevier, 2000. ISBN: 9780122386404. DOI: `10.1016/B978-012238640-4/50014-0`. URL: `http://www.sciencedirect.com/science/article/pii/B9780122386404500140`.

[9] Ashima Arora, Mohamad-Assaad Mawass, Oliver Sandig, Chen Luo, Ahmet A. Ünal, Florin Radu, Sergio Valencia, and Florian Kronast. Spatially resolved investigation of all optical magnetization switching in TbFe alloys. *Scientific reports*, 7(1):9456, 2017. ISSN: 2045-2322. DOI: `10.1038/s41598-017-09615-1`. URL: `http://www.ncbi.nlm.nih.gov/pubmed/28842586http://www.pubmedcentral.nih.gov/articlerender.fcgi?artid=PMC5573396http://www.nature.com/articles/s41598-017-09615-1`.

[10] S. N. Piramanayagam and Tow C. Chong, editors. *Developments in Data Storage.* John Wiley & Sons, Inc., Hoboken, NJ, USA, 2011. ISBN: 9781118096833. DOI: `10.1002/9781118096833`. URL: `http://doi.wiley.com/10.1002/9781118096833`.

[11] D. Schick, M. Herzog, H. Wen, P. Chen, C. Adamo, P. Gaal, D.G. Schlom, P. G. Evans, Y. Li, and M. Bargheer. Localized Excited Charge Carriers Generate Ultrafast Inhomogeneous Strain in the Multiferroic BiFeO3. *Physical review letters*, 112(9):097602, 2014. ISSN: 0031-9007. DOI: `10.1103/PhysRevLett.112.097602`. URL: `https://link.aps.org/doi/10.1103/PhysRevLett.112.097602`.

[12] R. Gross and A. Marx. *Festkörperphysik.* Oldenbourg, München, 2012.

[13] F. Laves and K. Löhberg. Die Kristallstruktur von intermetallischen Verbindungen der Formel AB2. *Nachrichten von der gesellschaft der wissenschaften zu göttingen*:59–66, 1934. URL: `http://d-nb.info/364969059`.

[14] J. R. Cullen and A. E. Clark. Magnetostriction and structural distortion in rare-earth intermetallics. *Physical review b*, 15(9):4510–4515, 1977. ISSN: 01631829. DOI: `10.1103/PhysRevB.15.4510`.

[15] J. H. Zhu, C. T. Liu, L. M. Pike, and P. K. Liaw. A thermodynamic interpretation of the size-ratio limits for laves phase formation. *Metallurgical and materials transactions a*, 30(5):1449–1452, 1999. ISSN: 1073-5623. DOI: `10.1007/s11661-999-0292-5`. URL: `http://link.springer.com/10.1007/s11661-999-0292-5`.

[16] K. Inoue, T. Kuroda, and K. Tachikawa. Some improvements in laves phase high-field superconductors. English. *Ieee transactions on magnetics*, 15(1):635–638, 1979. ISSN: 0018-9464. DOI: `10.1109/TMAG.1979.1060070`. URL: `http://ieeexplore.ieee.org/articleDetails.jsp?arnumber=1060070`.

[17] K. H. J. Buschow. Intermetallic compounds of rare-earth and 3d transition metals. *Reports on progress in physics*, 40(10):1179–1256, 1977. ISSN: 0034-4885. DOI: `10.1088/0034-4885/40/10/002`. URL: `http://stacks.iop.org/0034-4885/40/i=10/a=002`.

[18] A. Mougin, C. Dufour, K. Dumesnil, N. Maloufi, Ph. Mangin, and G. Patrat. Strain in single-crystal R Fe 2 (110) thin films (R = Y , Sm, Gd, Tb, Dy 0.7 Tb 0.3 , Dy, Er, Lu). *Physical review b*, 59(8):5950–5959, 1999. ISSN: 0163-1829. DOI: `10.1103/PhysRevB.59.5950`. URL: `http://journals.aps.org/prb/abstract/10.1103/PhysRevB.59.5950`.

[19] A. E. Clark, H. S. Belson, and R. E. Strakna. Elastic properties of rare-earth-iron compounds. *Journal of applied physics*, 44(6):2913, 1973. ISSN: 00218979. DOI: `10.1063/1.1662676`. URL: `http://scitation.aip.org/content/aip/journal/jap/44/6/10.1063/1.1662676`.

[20] M. J. Bentall, R. Cowley, W. J. L. Buyers, Z. Tun, W. Lohstroh, R. C. C. Ward, and M. R. Wells. Magnetic structures of Laves phase superlattices. *Journal of physics: condensed matter*, 15(25):4301–4330, 2003. ISSN: 0953-8984. DOI: `10.1088/0953-8984/15/25/303`.

[21] A. Y. Cho and J. R. Arthur. Molecular beam epitaxy. *Progress in solid state chemistry*, 10:157–191, 1975. ISSN: 00796786. DOI: `10.1016/0079-6786(75)90005-9`. URL: `http://www.sciencedirect.com/science/article/pii/0079678675900059`.

[22] V. Oderno, C. Dufour, K. Dumesnil, Ph. Mangin, and G. Marchal. Epitaxial growth of (110) DyFe2, TbFe2 and Dy0.7Tb0.3Fe2 thin films by molecular beam epitaxy. *Journal of crystal growth*, 165(1-2):175–178, 1996. ISSN: 00220248. DOI: `10.1016/0022-0248(96)00187-X`. URL: `http://www.sciencedirect.com/science/article/pii/002202489600187X`.

[23] J. Als-Nielsen and D. McMorrow. *Elements of Modern X-Ray Physics*. John Wiley & Sons, Ltd, New York, Chichester, Weinheim, Brisbane, Singapore, Toronto, 2001.

[24] A. E. Dwight and C. W. Kimball. TbFe2, a rhombohedral Laves phase. EN. *Acta crystallographica section b structural crystallography and crystal chemistry*, 30(11):2791–2793, 1974. ISSN: 05677408. DOI: `10.1107/S0567740874008156`. URL: `http://scripts.iucr.org/cgi-bin/paper?a11384`.

[25] B. Barbara, J. P. Giraud, J. Laforest, R. Lemaire, E. Siaud, and J. Schweizer. Spontaneous magnetoelastic distortion in some rare earth-iron Laves phases. *Physica b+c*, 86-88:155–157, 1977. ISSN: 03784363. DOI: `10.1016/0378-4363(77)90267-4`. URL: `http://www.sciencedirect.com/science/article/pii/0378436377902674`.

[26] Y. M. Tang, L. Y. Chen, L. Zhang, H. F. Huang, W. B. Xia, S. Y. Zhang, J. Wei, S. L. Tang, and Y. W. Du. Temperature dependence of the magnetostriction in polycrystalline PrFe1.9 and TbFe2 alloys: Experiment and theory. *Journal of applied physics*, 115(17):173902, 2014. ISSN: 0021-8979. DOI: `10.1063/1.4874940`. URL: `http://scitation.aip.org/content/aip/journal/jap/115/17/10.1063/1.4874940`.

[27] W. H. Bragg and W. L. Bragg. The Reflection of X-rays by Crystals. *Proceedings of the royal society a: mathematical, physical and engineering sciences*, 88(605):428–438, 1913. ISSN: 1364-5021. DOI: `10.1098/rspa.1913.0040`. URL: `http://rspa.royalsocietypublishing.org/content/88/605/428`.

[28] W. Friedrich, P. Knipping, and M. Laue. Interferenzerscheinungen bei Röntgenstrahlen. *Annalen der physik*, 346(10):971–988, 1913. ISSN: 00033804. DOI: `10.1002/andp.19133461004`. URL: `http://doi.wiley.com/10.1002/andp.19133461004`.

[29] M. Bargheer, N. Zhavoronkov, M. Woerner, and T. Elsaesser. Recent progress in ultrafast X-ray diffraction. *Chemphyschem : a european journal of chemical physics and physical chemistry*, 7(4):783–92, 2006. ISSN: 1439-4235. DOI: `10.1002/cphc.200500591`. URL: `http://www.ncbi.nlm.nih.gov/pubmed/16596604`.

[30] A. L. Patterson. A Fourier Series Method for the Determination of the Components of Interatomic Distances in Crystals. *Physical review*, 46(5):372–376, 1934. ISSN: 0031-899X. DOI: `10.1103/PhysRev.46.372`. URL: `http://journals.aps.org/pr/abstract/10.1103/PhysRev.46.372`.

[31] K. H. J. Buschow. Intermetallic compounds of rare earths and non-magnetic metals. en. *Reports on progress in physics*, 42(8):1373–1477, 1979. ISSN: 0034-4885. DOI: `10.1088/0034-4885/42/8/003`. URL: `http://iopscience.iop.org/article/10.1088/0034-4885/42/8/003`.

[32] K.N.R. Taylor. Intermetallic rare-earth compounds. en. *Advances in physics*, 20(87):551–660, 1971. ISSN: 0001-8732. DOI: `10.1080/00018737100101311`. URL: `http://www.tandfonline.com/doi/abs/10.1080/00018737100101311`.

[33] M. A. Ruderman and C. Kittel. Indirect Exchange Coupling of Nuclear Magnetic Moments by Conduction Electrons. *Physical review*, 96(1):99–102, 1954. ISSN: 0031-899X. DOI: `10.1103/PhysRev.96.99`. URL: `http://journals.aps.org/pr/abstract/10.1103/PhysRev.96.99`.

[34] T. Kasuya. A Theory of Metallic Ferro- and Antiferromagnetism on Zener's Model. *Progress of theoretical physics*, 16(1):45–57, 1956. ISSN: 0033-068X. DOI: `10.1143/PTP.16.45`. URL: `http://ptp.oxfordjournals.org/content/16/1/45`.

[35] K. Yosida. Magnetic Properties of Cu-Mn Alloys. *Physical review*, 106(5):893–898, 1957. ISSN: 0031-899X. DOI: `10.1103/PhysRev.106.893`. URL: `http://journals.aps.org/pr/abstract/10.1103/PhysRev.106.893`.

[36] W. Nolting and A. Ramakanth. *Quantum Theory of Magnetis*. Springer Science & Business Media, Heidelberg, 2009. URL: `http://www.springer.com/us/book/9783540854159`.

[37] U. Atzmony, M. P. Dariel, E. R. Bauminger, D. Lebenbaum, I. Nowik, and S. Ofer. Spin-Orientation Diagrams and Magnetic Anisotropy of Rare-Earth-Iron Ternary Cubic Laves Compounds. *Physical review b*, 7(9):4220–4232, 1973. ISSN: 0556-2805. DOI: `10.1103/PhysRevB.7.4220`. URL: `http://journals.aps.org/prb/abstract/10.1103/PhysRevB.7.4220`.

[38] G. J. Bowden, P. A. J. Groot, J. D. O Neil, B. D. Rainford, and A. A. Zhukov. On the anomalous temperature-dependent magnetostriction in intermetallic DyFe 2. en. *Journal of physics: condensed matter*, 16(13):2437–2446, 2004. ISSN: 0953-8984. DOI: `10.1088/0953-8984/16/13/021`. URL: `http://iopscience.iop.org/article/10.1088/0953-8984/16/13/021`.

[39] E. Burzo. Magnetic and Crystallographic Properties of Rare-Earth and Yttrium-Iron Laves Phases. *Zeitschrift angewandter physik*, 32(2):127–132, 1971.

[40] N. W. Ashcroft and D. N. Mermin. *Festkörperphysik*. Oldenbourg, München, Wien, 3rd edition, 2007.

[41] R. S. Sery, H. T. Savage, B. K. Tanner, and G. F. Clark. Domain configurations in single crystal TbFe2 and Tb0.27Dy0.73Fe2. *Journal of applied physics*, 49(3):2010, 1978. DOI: `10.1063/1.324779`. URL: `http://scitation.aip.org/content/aip/journal/jap/49/3/10.1063/1.324779`.

[42] J. Geshev, L. Bozukov, J.M.D. Coey, and M. Mikhov. Hysteresis of ball-milled TbFe2 fine particles. *Journal of magnetism and magnetic materials*, 170(1-2):219–222, 1997. ISSN: 03048853. DOI: `10.1016/S0304-8853(96)00754-8`. URL: `http://www.sciencedirect.com/science/article/pii/S0304885396007548`.

[43] A. E. Clark. Magnetic and Magnetoelastic Properties of Highly Magnetostrictive Rare Earth-Iron Laves Phase Compounds. In *Magnetism and magnetic materials — 1973: nineteenth annual conference*. Volume 18. (1). ASCE, 1974, pages 1015–1029. ISBN: 0-88318-117-7. DOI: `10.1063/1.2947192`. URL: `http://scitation.aip.org/content/aip/proceeding/aipcp/10.1063/1.2947192`.

[44] A. E. Clark and D. Crowder. High temperature magnetostriction of TbFe2 and Tb.27Dy.73Fe2. English. *Ieee transactions on magnetics*, 21(5):1945–1947, 1985. ISSN: 0018-9464. DOI: `10.1109/TMAG.1985.1064034`. URL: `http://ieeexplore.ieee.org/articleDetails.jsp?arnumber=1064034`.

[45] A. E. Clark, R. Abbundi, H. T. Savage, and O. D. McMasters. Magnetostriction of rare earth-Fe2 laves phase compounds. *Physica b+c*, 86-88:73–74, 1977. ISSN: 03784363. DOI: `10.1016/0378-4363(77)90231-5`. URL: `http://www.sciencedirect.com/science/article/pii/0378436377902315`.

[46] A. Mougin, C. Dufour, K. Dumesnil, and Ph. Mangin. Strain-induced magnetic anisotropy in single-crystal R Fe 2 (110) thin films (R = D y , E r , T b , Dy 0.7 Tb 0.3 , Sm, Y). *Physical review b*, 62(14):9517–9531, 2000. ISSN: 0163-1829. DOI: `10.1103/PhysRevB.62.9517`. URL: `http://journals.aps.org/prb/abstract/10.1103/PhysRevB.62.9517`.

[47] A. del Moral. *Magnetostriction and Magnetoelasticity Theory: A Modern View. Handbook of Magnetism and Advanced Magnetic Materials.* John Wiley & Sons, 2007. URL: `http://onlinelibrary.wiley.com/book/10.1002/9780470022184`.

[48] K. B. Hathaway and A. E. Clark. Magnetostrictive Materials. *Mrs bulletin*, 18(4):34–41, 1993.

[49] G. F. Dionne. Origin of the magnetostriction effects from Mn3+, Co2+, and Fe2+ ions in ferrimagnetic spinels and garnets. *Journal of applied physics*, 50(6):4263, 1979. ISSN: 00218979. DOI: `10.1063/1.326459`. URL: `http://scitation.aip.org/content/aip/journal/jap/50/6/10.1063/1.326459`.

[50] W. Demptröder. *Experimentalphysik 2.* Springer-Lehrbuch, Berlin, 2008.

[51] E. R. Callen and H. B. Callen. Static Magnetoelastic Coupling in Cubic Crystals. *Physical review*, 129(2):578–593, 1963. ISSN: 0031-899X. DOI: `10.1103/PhysRev.129.578`. URL: `http://journals.aps.org/pr/abstract/10.1103/PhysRev.129.578`.

[52] U. Atzmony and M. P. Dariel. Nonmajor cubic symmetry axes of easy magnetization in rare-earth-iron Laves compounds. *Physical review b*, 13(9):4006–4014, 1976. ISSN: 0556-2805. DOI: `10.1103/PhysRevB.13.4006`. URL: `http://journals.aps.org/prb/abstract/10.1103/PhysRevB.13.4006`.

[53] M.T. Hutchings. Point-Charge Calculations of Energy Levels of Magnetic Ions in Crystalline Electric Fields. *Solid state physics*, 16:227–273, 1964. ISSN: 00811947. DOI: `10.1016/S0081-1947(08)60517-2`. URL: `http://www.sciencedirect.com/science/article/pii/S0081194708605172`.

[54] R. Becker and W. Döring. *Ferromagnetismus.* Julius Springer, Berlin, 2012.

[55] K. N. Martin, P. A. J. Groot, B. D. Rainford, K. Wang, G. J. Bowden, J. P. Zimmermann, and H. Fangohr. Magnetic anisotropy in the cubic Laves REFe 2 intermetallic compounds. en. *Journal of physics: condensed matter*, 18(2):459–478, 2006. ISSN: 0953-8984. DOI: `10.1088/0953-8984/18/2/009`. URL: `http://iopscience.iop.org/article/10.1088/0953-8984/18/2/009`.

[56] D. Royer and E. Dieulesaint. *Elastic Waves in Solids I.* Springer, Berlin, Heidelberg, 1996.

[57] W. Voigt. *Lehrbuch der Kristallphysik: mit Ausschluß der Kristalloptik.* Teubner, Leipzig, 1910.

[58] W. Demptröder. *Experimentalphysik 1.* Springer-Lehrbuch, Berlin, 2008.

[59] M. L. Spano, K. B. Hathaway, and H. T. Savage. Magnetostriction and magnetic anisotropy of field annealed Metglas 2605 alloys via dc M-H loop measurements under stress. *Journal of applied physics*, 53(3):2667, 1982. ISSN: 00218979. DOI: `10.1063/1.330932`. URL: `http://scitation.aip.org/content/aip/journal/jap/53/3/10.1063/1.330932`.

[60] G. V. Blessing and A. E. Clark. Elastic properties of Tb[sub 0.3]Dy[sub 0.7]Fe[sub 2] measured ultrasonically. *The journal of the acoustical society of america*, 60(S1):S53, 1976. ISSN: 00014966. DOI: `10.1121/1.2003403`. URL: `http://scitation.aip.org/content/asa/journal/jasa/60/S1/10.1121/1.2003403`.

[61] V. Z. C. Paes and D. H. Mosca. Effective elastic and magnetoelastic anisotropies for thin films with hexagonal and cubic crystal structures. *Journal of magnetism and magnetic materials*, 330:81–87, 2013. ISSN: 03048853. DOI: `10.1016/j.jmmm.2012.10.036`. URL: `http://www.sciencedirect.com/science/article/pii/S030488531200858X`.

[62] H. Klimker, M. Rosen, M. P. Dariel, and U. Atzmony. Elastic and magnetoelastic properties of polycrystalline rare-earth-iron Laves compounds. *Physical review b*, 10(7):2968–2972, 1974. ISSN: 0556-2805. DOI: `10.1103/PhysRevB.10.2968`. URL: `http://journals.aps.org/prb/abstract/10.1103/PhysRevB.10.2968`.

[63] W. P. Mason. Derivation of Magnetostriction and Anisotropic Energies for Hexagonal, Tetragonal, and Orthorhombic Crystals. *Physical review*, 96(2):302–310, 1954. ISSN: 0031-899X. DOI: `10.1103/PhysRev.96.302`. URL: `http://link.aps.org/doi/10.1103/PhysRev.96.302`.

[64] K. P. Bjelow. Erscheinungen in ferromagnetischen Metallen. Berlin, 1953.

[65] N. S. Akulov. Über die Anwendungen des Gesetzes ferromagnetischer Anisotropie zur Berechnung der Eigenschaften polykristallinischen Eisens. *Zeitschrift für physik*, 66(7-8):533–542, 1930. ISSN: 1434-6001. DOI: `10.1007/BF01402036`. URL: `http://link.springer.com/10.1007/BF01402036`.

[66] A. E. Clark and H. S. Belson. Magnetostriction of Terbium-Iron and Erbium-Iron Alloys. *Ieee transactions on magnetics*, 8(3):477–479, 1972. ISSN: 19410069. DOI: `10.1109/TMAG.1972.1067486`. URL: `http://ieeexplore.ieee.org/lpdocs/epic03/wrapper.htm?arnumber=1067486`.

[67] M. Melamud, K. B. Hathaway, and J. R. Cullen. Magnetic structure changes in amorphous RE-Fe2 alloys as detected by Ultrasonic Measurement. *Physics letters*, 73A(I):58–62, 1979.

[68] J. R. Cullen, G. V. Blessing, S. Rinaldi, and E. R. Callen. Magnetic and elastic properties of rare earth-iron materials. *Journal of magnetism and magnetic materials*, 7(1-4):160–167, 1978. ISSN: 03048853. DOI: `10.1016/0304-8853(78)90173-7`. URL: `http://www.sciencedirect.com/science/article/pii/0304885378901737`.

[69] S. Buck and M. Fähnle. Magnetostriction in TbFe2: weak influence of the internal structural distortion. *Journal of magnetism and magnetic materials*, 204(1-2):L1–L4, 1999. ISSN: 03048853. DOI: `10.1016/S0304-8853(99)00450-3`. URL: `http://www.sciencedirect.com/science/article/pii/S0304885399004503`.

[70] M J Bentall, R A Cowley, W J L Buyers, Z Tun, W Lohstroh, R C C Ward, and M R Wells. Magnetic structures of Laves phase superlattices. en. *Journal of physics: condensed matter*, 15(25):4301–4330, 2003. ISSN: 0953-8984. DOI: `10.1088/0953-8984/15/25/303`. URL: `http://iopscience.iop.org/article/10.1088/0953-8984/15/25/303`.

[71] James R. Cullen and Arthur E. Clark. Magnetostriction and structural distortion in rare-earth intermetallics. *Physical review b*, 15(9):4510–4515, 1977. ISSN: 0556-2805. URL: `http://journals.aps.org/prb/abstract/10.1103/PhysRevB.15.4510`.

[72] S. P. Zeuschner. Zeitaufgelöste Röntgenbeugung mit einer Mikrofokus-Röntgenröhre. Bachelor Thesis. Universität Potsdam, 2014.

[73] Helmholtz Zentrum Berlin, BESSY II Synchrotron. URL: `https://www.helmholtz-berlin.de/quellen/bessy/index{\_}de.html` (visited on 09/29/2017).

[74] Optigrpah GmbH, Physical characteristics of HOPG. (Visited on 09/29/2017).

[75] E. Jaeschke, S. Khan, D. Kramer, and D. Schirmer. Status of the high brilliance synchrotron radiation source BESSY-II. In *Proceedings particle accelerator conference*. Volume 3. IEEE, 1996, pages 1411–1413. ISBN: 0-7803-2934-1. DOI: `10.1109/PAC.1995.505239`. URL: `http://ieeexplore.ieee.org/document/505239/`.

[76] M. Reinhardt and W. Leitenberger. XPP: X-ray Pump Probe station at BESSY II. *Journal of large-scale research facilities jlsrf*, 2016. URL: `https://jlsrf.org/index.php/lsf/article/view/82/pdf`.

[77] U. Pietsch, V. Holý, and T. Baumbach. *High-resolution X-ray Scattering*. Springer Science & Business Media, New York, 2nd edition, 2004. ISBN: 9781441923073.

[78] D. Kriegner, E. Wintersberger, and J. Stangl. Xrayutilities: a versatile tool for reciprocal space conversion of scattering data recorded with linear and area detectors. *Journal of applied crystallography*, 46(4):1162–1170, 2013. DOI: `10.1107/S0021889813017214`. URL: `http://scripts.iucr.org/cgi-bin/paper?S0021889813017214`.

[79] Certified Scientific Software, SPEC: Software for Diffraction. URL: `https://www.certif.com/content/spec/` (visited on 09/29/2017).

[80] K. Dumesnil, S. Fernandez, A. Avisou, C. Dufour, A. Rogalev, F. Wilhelm, and E. Snoeck. Temperature and thickness dependence of the magnetization reversal in DyFe2/YFe2 exchange-coupled superlattices. *The european physical journal b*, 72(2):159–171, 2009. ISSN: 1434-6028. URL: `http://www.springerlink.com/index/10.1140/epjb/e2009-00351-8`.

[81] S. Foner. Vibrating Sample Magnetometer. *Review of scientific instruments*, 27(7):548–548, 1956. ISSN: 0034-6748. DOI: `10.1063/1.1715636`. URL: `http://aip.scitation.org/doi/10.1063/1.1715636`.

[82] O. Kovalenko, T. Pezeril, and Vasily V. Temnov. New Concept for Magnetization Switching by Ultrafast Acoustic Pulses. *Physical review letters*, 110(26):266602, 2013. ISSN: 0031-9007. DOI: `10.1103/PhysRevLett.110.266602`. URL: `https://link.aps.org/doi/10.1103/PhysRevLett.110.266602`.

[83] S. Blundell. *Magnetism in Condensed Matter*. Oxford University Press Inc., Oxford, 2001.

[84] M. Huth and C. P. Flynn. Magnetism and microstructure in epitaxial TbFe 2 (111) thin films. *Physical review b*, 58(17):11526–11533, 1998. ISSN: 0163-1829. DOI: `10.1103/PhysRevB.58.11526`. URL: `http://journals.aps.org/prb/abstract/10.1103/PhysRevB.58.11526`.

[85] V. Hoffmanna, R. Schäfer, E. Appel, A. Hubert, and H. Soffel. First domain observations with the magneto-optical Kerr effect on Ti-ferrites in rocks and their synthetic equivalents. *Journal of magnetism and magnetic materials*, 71(1):90–94, 1987. ISSN: 0304-8853. DOI: `10.1016/0304-8853(87)90336-2`. URL: `http://www.sciencedirect.com/science/article/pii/0304885387903362`.

[86] D. Schick, A. Bojahr, M. Herzog, C. von Korff Schmising, R. Shayduk, W. Leitenberger, P. Gaal, and M. Bargheer. Normalization schemes for ultrafast x-ray diffraction using a table-top laser-driven plasma source. *Review of scientific instruments*, 83(2):025104, 2012. ISSN: 0034-6748. DOI: `10.1063/1.3681254`. URL: `http://aip.scitation.org/doi/10.1063/1.3681254`.

[87] D. Schick, R. Shayduk, A. Bojahr, M. Herzog, C. Von Korff Schmising, P. Gaal, and M. Bargheer. Ultrafast reciprocal-space mapping with a convergent beam. *Journal of applied crystallography*, 46(5):1372–1377, 2013. ISSN: 00218898. DOI: `10.1107/S0021889813020013`. URL: `http://scripts.iucr.org/cgi-bin/paper?S0021889813020013`.

[88] F. Zamponi, Z. Ansari, C. Korff Schmising, P. Rothhardt, N. Zhavoronkov, M. Woerner, T. Elsaesser, M. Bargheer, T. Trobitzsch-Ryll, and M. Haschke. Femtosecond hard X-ray plasma sources with a kilohertz repetition rate. *Applied physics a*, 96(1):51–58, 2009. ISSN: 0947-8396. DOI: `10.1007/s00339-009-5171-9`. URL: `http://link.springer.com/10.1007/s00339-009-5171-9`.

[89] M. Bargheer, N. Zhavoronkov, R. Bruch, H. Legall, H. Stiel, M. Woerner, and T. Elsaesser. Comparison of focusing optics for femtosecond X-ray diffraction. *Applied physics b*, 80(6):715–719, 2005. ISSN: 0946-2171. DOI: `10.1007/s00340-005-1792-7`. URL: `http://link.springer.com/10.1007/s00340-005-1792-7`.

[90] D. Schick. Ultrafast Lattice Dynamics in Photoexcited Nanostructures - Femtosecond X-ray Diffraction with Optimized Evaluation Schemes. Dissertation. Universität Potsdam, 2013. URL: `http://opus.kobv.de/ubp/volltexte/2013/6882/`.

[91] Jannick Weisshaupt, Vincent Juvé, Marcel Holtz, Michael Woerner, and Thomas Elsaesser. Theoretical analysis of hard x-ray generation by nonperturbative interaction of ultrashort light pulses with a metal. *Structural dynamics*, 2(2):024102, 2015. ISSN: 2329-7778. DOI: `10.1063/1.4915485`. URL: `http://aca.scitation.org/doi/10.1063/1.4915485`.

[92] D. Schick, M. Herzog, A. Bojahr, W. Leitenberger, A. Hertwig, R. Shayduk, and M. Bargheer. Ultrafast lattice response of photoexcited thin films studied by X-ray diffraction. *Structural dynamics*, 1(6):064501, 2014. ISSN: 2329-7778. DOI: `10.1063/1.4901228`. URL: `http://scitation.aip.org/content/aip/journal/sdy/1/6/10.1063/1.4901228`.

[93] Pascal Ruello and Vitalyi E Gusev. Physical mechanisms of coherent acoustic phonons generation by ultrafast laser action. *Ultrasonics*, 56(0):21–35, 2015. ISSN: 0041-624X. DOI: `10.1016/j.ultras.2014.06.004`. URL: `http://www.sciencedirect.com/science/article/pii/S0041624X1400153X`.

[94] Zhibin Lin, Leonid V Zhigilei, and Vittorio Celli. Electron-phonon coupling and electron heat capacity of metals under conditions of strong electron-phonon nonequilibrium. *Phys. rev. b*, 77(7):75133, 2008. DOI: `10.1103/PhysRevB.77.075133`. URL: `http://link.aps.org/doi/10.1103/PhysRevB.77.075133`.

[95] U. Bovensiepen. Coherent and incoherent excitations of the Gd(0001) surface on ultrafast timescales. *Journal of physics: condensed matter*, 19(8):083201, 2007. ISSN: 0953-8984. DOI: `10.1088/0953-8984/19/8/083201`. URL: `http://stacks.iop.org/0953-8984/19/i=8/a=083201?key=crossref.e0b4506a1f4bf94a3de227c3d5605c1a`.

[96] D. Schick, A. Bojahr, M. Herzog, R. Shayduk, C. von Korff Schmising, and M. Bargheer. udkm1Dsim—A simulation toolkit for 1D ultrafast dynamics in condensed matter. *Computer physics communications*, 185(2):651–660, 2014. ISSN: 00104655. DOI: `10.1016/j.cpc.2013.10.009`. URL: `http://linkinghub.elsevier.com/retrieve/pii/S0010465513003378`.

[97] MatWeb, material property data for Terfenol. URL: `http://www.matweb.com/` (visited on 09/29/2017).

[98] M. E. Straumanis and S. Zyszczynski. Lattice parameters, thermal expansion coefficients and densities of Nb, and of solid solutions Nb–O and Nb–N–O and their defect structure. *Journal of applied crystallography*, 3(1):1–6, 1970. ISSN: 00218898. DOI: `10.1107/S002188987000554X`. URL: `http://scripts.iucr.org/cgi-bin/paper?S002188987000554X`.

[99] E. R. Dobrovinskaya, L. A. Lytvynov, and V. Pishchik. *Sapphire. Material, Manufacturing, Applications.* Springer, 2009. URL: `http://fstroj.uniza.sk/journal-mi/PDF/sapphire.pdf`.

[100] C. Y. Ho, R. W. Powell, and P. E. Liley. Thermal Conductivity of the Elements. *Journal of physical and chemical reference data*, 1(2):279–421, 1972. ISSN: 0047-2689. DOI: `10.1063/1.3253100`. URL: `http://aip.scitation.org/doi/10.1063/1.3253100`.

[101] D. J. Germano and R. A. Butera. Heat capacity of, and crystal-field effects in, the R Fe 2 intermetallic compounds (R = Gd, Tb, Dy, Ho, Er, Tm, and Lu). *Physical review b*, 24(7):3912–3927, 1981. ISSN: 0163-1829. URL: `http://link.aps.org/doi/10.1103/PhysRevB.24.3912`.

[102] W. M. Haynes. *CRC Handbook of Chemistry and Physics.* Taylor & Francis, 93rd edition, 2012.

[103] D. C. Ginnings and G. T. Furukawa. Heat Capacity Standards for the Range 14 to 1200 K. *Journal of the american ceramic society*, 43(6), 1953. URL: `http://pubs.acs.org/doi/pdf/10.1021/ja01099a004`.

[104] K. J. Carroll. Elastic Constants of Niobium from 4.2° to 300°K. *Journal of applied physics*, 36(11):3689–3690, 1965. ISSN: 0021-8979. DOI: `10.1063/1.1703072`. URL: `http://aip.scitation.org/doi/10.1063/1.1703072`.

[105] J. B. Wachtmann, W. E. Tefft, D. G. Lam, and R. P. Stinchfield. Elastic Constants of Synthetic Single-Crystal Corundum at Room Temperature. *Journal of the american ceramic society*, 43(6):334–334, 1960. ISSN: 0002-7820. DOI: `10.1111/j.1151-2916.1960.tb13663.x`. URL: `http://doi.wiley.com/10.1111/j.1151-2916.1960.tb13663.x`.

[106] Webelements:, Linear expansion coefficient. URL: `https://www.webelements.com/periodicity/coeff{\_}thermal{\_}expansion/` (visited on 09/29/2017).

[107] M. Lucht, M. Lerche, H.-C. Wille, Y. V. Shvyd 'ko, H. D. Rüter, E. Gerdau, and P. Becker. Precise measurement of the lattice parameters of Sapphire in the temperature range 4.5 K -250 K using the Moessbauer wavelength standard. *J. appl. cryst*, 36(4):1075–1081, 2003. URL: `http://citeseerx.ist.psu.edu/viewdoc/download?doi=10.1.1.485.2021{\&}rep=rep1{\&}type=pdf`.

[108] D. Schick, P. Gaal, A. Bojahr, W. Leitenberger, R. Shayduk, A. Hertwig, I. Vrejoiu, M. Herzog, and M. Bargheer. Ultrafast x-ray diffraction studies of photoexcited coherent phonons in SrRuO3 thin films, 2013. arXiv: `1301.3324`. URL: `http://arxiv.org/abs/1301.3324`.

[109] S. D. Brorson, J. G. Fujimoto, and E. P. Ippen. Femtosecond electronic heat-transport dynamics in thin gold films. *Physical review letters*, 59(17):1962–1965, 1987. ISSN: 0031-9007. DOI: `10.1103/PhysRevLett.59.1962`. URL: `https://link.aps.org/doi/10.1103/PhysRevLett.59.1962`.

[110] S.-S. Wellershoff, J. Hohlfeld, J. Güdde, and E. Matthias. The role of electron–phonon coupling in femtosecond laser damage of metals. *Applied physics a materials science & processing*, 69(S1):S99–S107, 1999. ISSN: 0947-8396. DOI: `10.1007/s003399900305`. URL: `http://link.springer.com/10.1007/s003399900305`.

Acknowledgments

Writing a master thesis and conducting including experiments takes a lot of time and effort. Thus it would have been difficult to endure without the many people who accompanied me during this journey. This part of the thesis is for those who helped, worked and lived with me and for me to thank them.

At first I would like to thank the UDKM group of the University of Potsdam for their help, support and in whose kind and supportive work climate I mainly developed my thesis. Lead by Prof. Matias Bargheer who helped me to start my research on magnetostriction as his capacity for enthusiasm concerning solid state physics and ultrafast phenomena rapidly convinced me to share these interests with him. While being friendly and optimistic, his questions were the most helpful tool to reach a sophisticated understanding and were the determining factor which animated me a lot.

A special thanks naturally goes to my colleague Alexander von Reppert who was very friendly and vocal facilitating my initial inclusion to the UDKM group. Still, from there he did not stop to help me out at any occurring situation I can think of and supported me theoretically and experimentally as he is mainly responsible for the conductance of the experiments at the PXS, together with Jan Pudell to whom I am grateful for administrating the digital environment of the UDKM and providing additional computer for the execution of my simulations. During the beamtime at BESSY II I was lucky to be supported by Dr. Matthias Reinhardt, Dr. Wolfram Leitenberger, Dr. Marc Herzog and Azize Koc, to which I am obliged not only because of their knowledge and the resulting inspiring discussions but also because of their kindness. The same applies for Dr. Matthias Rössle and Lisa Willig who provided the opitcal penetration depth via elipsometry measurements for the used $TbFe_2$. As our capable technician Elko Hannemann constructed the rotation stages for the application of external magnetic fields, he is substantially involved in the success of the static magnetostriction measurements. Likewise, this applies for Mattias Sander and Dr. Flavio Zamponi who supported me with important input during the MFXT measurements.

I would also like to acknowledge the work of my international scientific colleagues who collaborated more or less directly with me during the course of my thesis. At first, Dr. Karine Dumesnil of the Institute Jean Lamour in Nacy, France, since she agreed to assess this thesis without even knowing me. Additionally, she provided the sample I conducted the presented measurements on and participated on multiple helpful publications concerning magnetostriction. Moreover did her colleague Arnaud Hillion conduct VSM measurements on the same sample which were crucial to finish the puzzle of the inner working of $TbFe_2$. Besides our french colleagues, I contacted Prof. Graham Bowden of the University of Southampton, Great Britain, concerning one of his publications and I am thankful that he took his time to answer me and clarify the concept of the common magnetostrictive formalisms.

In the end, I would like to thank the people I love; my friends and family. Beginning with my parents Markus and Birgit, who supported me my whole life under all circumstances in every conceivable way and because of them I am fortunate to have two wonderful prosperous siblings, René and Leya who accompanied me throughout my whole life and always encouraged me during my work. As I finish my studies with this thesis, I realise that the most precious time I spent was not used thinking thoughts, carrying out discussions or experiments concerning physics but being with my friends, René, Marius, Frank, Vincent, Kristin, Tobias, and many more. This applies undoubtedly to my outstandingly best friend and greatest love, Ines, unquestionably the most beautiful thing ever happened to me.

Statement of authorship

I hereby confirm that I drew up this submitted Master thesis independently, used no other than the specified aids whereas the parts of the thesis which are equivalent or verbatim to provided sources are precisely marked as references.

Hiermit erkläre ich, dass ich die vorliegende Masterarbeit selbstständig angefertigt, keine anderen als die angegebenen Hilfsmittel benutzt und die Stellen der Arbeit, die im Wortlaut oder im wesentlichen Inhalt aus anderen Werken entnommen wurden, mit genauer Quellenangabe kenntlich gemacht habe.

Place, Date

Steffen Peer Zeuschner